DEVELOPMENT AND APPLICATION OF HYDRAULIC FRACTURING SIMULATION FOR ANALYSIS OF FRACTURE INTERFERENCE AND DISTRIBUTED ACOUSTIC SENSING CHARACTERIZATION

by

Jiahui Chen

A thesis submitted in partial fulfillment of the requirements for the degree of

Doctor of Philosophy

in

PETROLEUM ENGINEERING

Department of Civil and Environmental Engineering
University of Alberta

ABSTRACT

Low-frequency distributed acoustic sensing (LF-DAS) is one of the promising diagnostic techniques to detect and characterize hydraulic fractures. LF-DAS signals can capture fracture hits and the strain field around the hydraulic fracture and provide continuous monitoring of fracture geometry and production at each stage of the wellbore. However, the interpretation of field LF-DAS data and the relationship between fluid allocation and production can be challenging due to the complexity of the underground conditions.

This thesis develops a new workflow for coupling flow and geomechanical computations and simulating fracture propagation in the MATLAB Reservoir Simulation Toolbox (MRST) – an open-source reservoir simulation software. A new discrete fracture model (DFM) is implemented. Unstructured meshing is used to discretize the gridding domain. The matrix-to-matrix, fracture-to-fracture, and fracture-to-matrix fluxes are computed explicitly in the computational domain following the control volume formulation. The flow calculations and the geomechanical computations are solved sequentially: the governing equations for poroelasticity are incorporated, and the fixed stress splitting coupling methodology is employed. The hydraulic fracture is set to propagate along a prescribed path with a specific propagation or activation criterion. The accuracy of our model is also validated against the KGD analytical solutions for the leak-off-viscosity, storage-viscosity and leak-off-toughness dominated regimes.

This study presents a comprehensive investigation of production performance and stress evolution in hydraulically fracturing formations using the proposed coupling strategy. This model considers the effects of poroelasticity and stress or strain variation in the fractured domains and factors influencing the behaviour of fracture interference, allowing for a more accurate

representation of complex fracture interference behavior. Several case studies and sensitivity analyses demonstrate the approach's utility and examine fracture interference, closure, and stress shadowing effects. The modelling work facilitates interpreting field measurement data by investigating characteristics of fracture hits from adjacent wells. Both the matrix and fractures are discretized, enabling the investigation of how different rock properties impact strain variation. Additionally, this thesis presents several case studies utilizing the proposed model and raw DAS data analysis to explore the effects of cross-well fracture hits and completion designs on fracture propagation and production conductivity. The study aims to provide new and valuable insights into the implications of fracture interference on optimal designs during hydraulic fracturing stimulation, and completion design optimization and interpretation of DAS data, which will inform decision-making, ultimately leading to improved well productivity and efficiency.

PREFACE

This thesis is an original work by Jiahui Chen. Parts of the research project have been previously published or are ready for the journal submission.

Chapter 3 and 4 are composed in part by Chen, J., Xu, Z., & Leung, J. Y. (2022). Analysis of fracture interference–Coupling of flow and geomechanical computations with discrete fracture modeling using MRST. *Journal of Petroleum Science and Engineering*, *219*, 111134; and Chen, J., & Leung, J. Y. (2020, December). Analysis of fracture interference–coupling of flow and geomechanical computations with discrete fracture modeling. In *Unconventional Resources Technology Conference, 20–22 July 2020* (pp. 4573-4588). I was responsible for the conceptualization, methodology, formal analysis, and the original draft composition. Xu, Z. was responsible for methodology and formal analysis. Leung, J. Y. was the supervisory author and was involved in project administration, funding acquisition, conceptualization, methodology, formal analysis, data curation, and manuscript review and editing.

Chapter 5 is composed in part by Chen, J., Leung, J. Y., & van der Baan, M. (2023, March). Characterization of Distributed Acoustic Sensing Signals in Hydraulic Fracturing Stimulation-A Coupled Flow-Geomechanical Simulation Approach. In *SPE Canadian Energy Technology Conference and Exhibition*, Calgary, AB, Canada. I was responsible for the conceptualization, methodology, formal analysis, and the original draft composition. Leung, J. Y., and van der Baan, M. were the supervisory authors and were involved in project administration, funding acquisition, conceptualization, methodology, formal analysis, and manuscript review and editing.

Chapter 6 of this thesis represents an original contribution by Jiahui Chen and contains previously unpublished content.

DEDICATION

To my beloved wife, my cherished family, and my exceptional supervisor, I dedicate this thesis with profound gratitude and immense love.

ACKNOWLEDGEMENT

First and foremost, I would like to express my deepest gratitude to my esteemed supervisor, Dr. Juliana Y. Leung. Her exceptional support, invaluable guidance, and mentorship have played a pivotal role in shaping my academic and personal growth. Beyond the realm of academia, Dr. Leung has also imparted invaluable life lessons on professionalism, kindness, and integrity. I am truly fortunate to have had the opportunity to work under her supervision and to learn from her wealth of knowledge and experience. This thesis would not have been possible without her mentorship and support.

I would like to extend my gratitude to the members of my examining committee, Dr. Mirko van der Baan, Dr. Samer Adeeb, Dr. Huazhou Li, and Dr. Gary Zhao for their attendance to my final defense and their insightful comments. I would also like to thank all my colleagues in Dr. Leung's research group for their support and friendship.

I would like to express my appreciation to the China Scholarship Council (CSC) and the Natural Sciences and Engineering Research Council of Canada (NSERC) for the financial support, MathWorks® for providing academic licenses for MATLAB R2019a, and Sintef Applied Mathematics for providing the MATLAB Reservoir Simulation Toolbox (MRST).

Lastly, I would like to express my heartfelt appreciation to all my friends and family, I would never be able to get to this point without your unconditional support. To my parents and my in-laws, I am deeply grateful for your selfless help and support during the moments when I needed it the most. To my wife, Xin Zhang, the mother of our beloved daughter, Ellie, I am eternally grateful for your understanding, unquestioning support, and endless love. Your presence in my life has been my greatest source of strength.

TABLE OF CONTENTS

ABSTRACT ii
PREFACE iv
DEDICATION v
ACKNOWLEDGEMENT vi
TABLE OF CONTENTS vii
LIST OF TABLES x
LIST OF FIGURES xi
LIST OF SYMBOLS xvi
CHAPTER 1 : INTRODUCTION 1
1.1 Background and Motivations 1
1.2 Problem Statement 4
1.3 Research Objectives 6
1.4 Thesis Outline 7
CHAPTER 2 : LITERATURE REVIEW 9
2.1 Overview 9
2.2 Review of the Development of Hydraulic Fracturing Models 9
2.2.1 KGD Model 9
2.2.2 PKN Model 11
2.2.3 Radial Model / Penny-Shaped Model 12
2.3 Review of Numerical Model Strategies for Fractured Media 14
2.3.1 Flow Modelling of Fractured Rocks 14
2.3.2 Geomechanical Modelling of Fractured Rocks 16
2.3.3 Approaches for Coupling Fluid Flow and Geomechanics Simulations 19
2.4 Review of Distributed Acoustic Sensing Technology 20
2.4.1 Historical Development of Fiber Optic Sensors 20
2.4.2 Distributed Acoustic Sensing Technology 21
2.4.3 Interpretations of DAS Data and the Impact on Optimization of Completion Design 24
CHAPTER 3 : STATIC MODEL SETUP AND VALIDATION 27
3.1 Overview 27
3.2 Mathematical Model 27
3.2.1 Governing Equations 27

3.2.2 Constitutive Relations 28
3.2.3 Fracture Deformation Mechanism 29
3.2.4 Boundary Conditions 30
3.3 Discretization and Solution Strategy 32
3.3.1 Grid Structure 32
3.3.2 Finite Volume Discretization of Flow Equations 34
3.3.3 Discretization for Mechanical Problems 35
3.3.4 Solution Strategy 37
3.4 Model Validation 38
3.4.1 McNamee Gibson's Problem 38
3.4.2 Fracture Deformation Verification 40
CHAPTER 4 : ANALYSIS OF FRACTURE INTERFERENCE AND PRESSURE DISTRIBUTION 44
4.1 Overview 44
4.2 Analysis of Hydraulic Fracturing Pressure Distribution 44
4.2.1 Single Planar Hydraulic Fracture Model Setup 44
4.2.2 Comparison of Pressure Distribution, Production Rate, and Cumulative Production 46
4.3 Sensitivity Analysis of Geomechanical Properties 47
4.3.1 Model Setup 49
4.3.2 Effects of Hydraulic Fracture Geometry 51
4.3.3 Effects of Well Spacing 53
4.3.4 Effects of Cluster Spacing 56
4.3.5 Effects of Differential Stress (DS) 58
4.4 Fluid Loss Mechanism Analysis 61
4.4.1 Model Setup 62
4.4.2 Model Initialization 63
4.4.3 Results and Discussion 65
CHAPTER 5 : CHARACTERIZATION OF DISTRIBUTED ACOUSTIC SENSING SIGNALS IN HYDRAULIC FRACTURING STIMULATION 67
5.1 Overview 67
5.2 Fracture Propagation Model 68
5.3 Validation of Fracture Propagation Model 68

5.3.1 Storage-Viscosity Dominated Regime 69
5.3.2 Leak-Off-Viscosity Dominated Regime 70
5.3.3 Leak-Off-Toughness Dominated Regime 72
5.4 Characterization of DAS Signals 74
5.4.1 Base case 77
5.4.2 Multi-Frac Case 78
5.4.3 Antenna case 80
5.5 Sensitivity analysis 82
5.5.1 Effects of Natural Fracture Initial Permeability 82
5.5.2 Effects of Monitoring Well Location 85
5.5.3 Effects of Matrix Permeability on the Heart Shape Size 89
CHAPTER 6 : HYDRAULIC FRACTURING MONITORING WITH DAS AND ANALYSIS OF FRACTURE HIT IMPACT ON FRACTURING STIMULATION AND PRODUCTION .. 91
6.1 Overview 91
6.2 Project Setup 92
6.2.1 Well Layout 92
6.2.2 Data Acquisition Schedule 92
6.3 Methodology 94
6.3.1 Far-Field DAS Data Characteristics 94
6.3.2 Measurement Depth of Fracture Hit 95
6.3.3 Near-Wellbor DAS Data 97
6.3.4 Production Data 99
6.4 Results and Discussion 100
6.4.1 Effects of Cluster Spacing and Well Spacing on Fracture Length 100
6.4.2 Effects on Production 104
6.4.3 The Impact of Stress Shadowing on Hydraulic Fracture Growth in Later Stages .. 107
CHAPTER 7 : CONCLUSIONS AND FUTURE WORK 112
7.1 Summary and Conclusions 112
7.2 Contributions 116
7.3 Recommendations for Future Work 117
BIBLIOGRAPHY 119
Appendix A 135

LIST OF TABLES

Table 3.1. Parameters used in McNamee Gibson's problem. 39

Table 3.2. Parameters used in fracture deformation verification case. 43

Table 4.1. Parameters used in the single planar hydraulic fracture problem. 45

Table 4.2. Parameters used in fluid loss analysis cases. 63

Table 5.1. Parameters used for storage-viscosity dominated regime modelling. 70

Table 5.2. The parameters used for leak-off-toughness dominated regime modelling. 72

Table 5.3. Parameters used for field DAS data comparison. 76

Table 6.1. Parameters used in the sensitivity analysis case. 101

LIST OF FIGURES

Figure 1.1. A schematic of multiple hydraulic fracturing in parent-child drilling. 2

Figure 2.1. Schematic of the KGD model setup. L_f is the fracture half-length, a is the fracture aperture and h_f is the fracture height. Modified from Adachi et al. (2007). 10

Figure 2.2. Schematic of the PKN model setup. L_f is the fracture half-length, a is the fracture aperture, and h_f is the fracture height. Modified from Adachi et al. (2007). 12

Figure 2.3. Schematic of the radial model setup. a is the fracture aperture, p is the internal fluid pressure, and r is the fracture radius. Modified from Adachi et al. (2007)..... 13

Figure 2.4. Schematic of discretization concepts for (a) the fractured rock mass, (b) FDM or FEM, (c) BEM, and (d) DEM, modified from (Jing, 2003)..... 19

Figure 2.5. Description of working principle for DAS system..... 22

Figure 2.6. (a) Hypothetical evolution of DAS response of a propagating hydraulic fracture, modified from Ugueto et al. (2019) and Ortega Perez (2022). (b) Field LF-DAS waterfall plot. 23

Figure 3.1. Boundary conditions for a fractured porous medium..... 32

Figure 3.2. The computational grid structure for (a) the flow problem and (b) the geomechanics problem. The white circle marks the pressure variables, and the black square represents the displacement variables. 34

Figure 3.3. Flow chart for the present coupled model. 38

Figure 3.4. (a) The geometry and boundary conditions of the McNamee Gibson's problem and (b) comparison of the analytical and the numerical solutions. 40

Figure 3.5. Fracture deformation validation model setup..... 42

Figure 3.6. Comparison of numerical solutions of fracture aperture between the present work and previous studies..... 43

Figure 4.1. The geometry and boundary conditions for the (a) geomechanical and (b) flow problems corresponding to the single planar hydraulic fracture case. 45

Figure 4.2. Comparison of pressure distribution after (a) 2 days (b) 15 days and (c) 90 days of production: uncoupled model (first row) and coupled model (second row). 46

Figure 4.3. Comparison of (a) production rate and (b) cumulative production between the uncoupled and coupled models. 47

Figure 4.4. (a) Geometry of the multi-stage hydraulic fracturing case, (b) pressure distribution and SHmax′ orientation, (c) SHmax′, and (d) Shmin′ magnitude after 1 year..... 50

Figure 4.5. (a), (d) Pressure distribution and SHmax′ orientation; (b), (e) SHmax′ magnitude; and (c), (f) Shmin′ magnitude for geometry 1 and geometry 2, respectively, after 1 year of production. 52

Figure 4.6. (a) SHmax′ orientation change, (b) pressure changes, (c) SHmax′ magnitude change, and (d) Shmin′ magnitude change along the x-direction at y = 250 m after 1 year. . 53

Figure 4.7. (a), (d) Pressure distribution and SHmax′; (b), (e) SHmax′ magnitude; and (c), (f) Shmin′ magnitude for well spacing of 220 m and well spacing of 280 m, respectively, after 1 year of production. 55

Figure 4.8. (a) SHmax′ orientation change, (b) pressure change, (c) SHmax′ change, and (d) Shmin′ change along the x-direction at y = 250 m after 1 year. 56

Figure 4.9. (a), (d) Pressure distribution and SHmax′; (b), (e) SHmax′ magnitude; and (c), (f) Shmin′ magnitude for cluster spacing of 25 m and cluster spacing of 75 m respectively after 1 year of production. 57

Figure 4.10. (a) SHmax′ orientation change, (b) pressure changes, (c) SHmax′ change, and (d) Shmin′ change along the x-direction at y = 250 m after 1 year. 58

Figure 4.11. (a), (d) Pressure distribution and SHmax′, (b), (e) SHmax′ magnitude, and (c), (f) Shmin′ magnitude for DS of 5 MPa and DS of 0 MPa respectively after 1 year of production. 60

Figure 4.12. (a) SHmax′ orientation change, (b) pressure changes, (c) SHmax′ change, and (d) Shmin′ change along the x-direction at y = 250 m after 1 year. 61

Figure 4.13. Schematic of the fracture network configuration and boundary conditions for case (a) simple natural fracture network and (b) branching natural fracture network. 63

Figure 4.14. Water saturation distribution for (a) simple natural fracture network and (b) complex natural fracture network after a shut-in period of 5 days. 64

Figure 4.15. Water recovery factor as a function of production time after a 5-day shut-in period. 65

Figure 5.1. Comparison of fracture half-length vs injection time between the storage-viscosity asymptotic analytical and numerical solutions. 70

Figure 5.2. Comparison of fracture half-length vs injection time (first row) and fracture aperture vs. injection time (second row) between the leak-off-viscosity asymptotic analytical solution, Carrier's numerical solution, and the numerical solution. 72

Figure 5.3. The lost volume per unit surface vs. square root time. The leak-off coefficient is obtained from the slope. 73

Figure 5.4. Comparison of fracture half-length vs. injection time between the leak-off-toughness analytical and numerical solutions. 74

Figure 5.5. A schematic of the top view of the simulation configuration. 76

Figure 5.6. Base case results: (a) hydraulic fracture trajectory as it approaches the monitor well; (b) hydraulic fracture trajectory as it hits the monitor well; (c) waterfall image of the simulated strain rate; (d) real DAS data for comparison. 78

Figure 5.7. Multi-frac case results: (a) fracture trajectory as the main fracture approaches the monitor well; (b) fracture trajectory as the lateral fracture hits the monitor well; (c) waterfall image of the simulated strain rate; (d) real DAS data for comparison. 79

Figure 5.8. Antenna case results: (a) fracture trajectory as the main fracture approaches the monitor well; (b) fracture trajectory as the lateral fracture is reactivated; (c) waterfall image of the simulated strain rate; (d) real DAS data for comparison. 81

Figure 5.9. Waterfall images of (a) simulated strain rate and (b) real DAS data for a higher k_{nfi} case. Comparisons of strain rate vs. time at (c) location = 35 m and (d) location = 38 m between two different k_{nfi}. 84

Figure 5.10. Waterfall images of simulated strain rate at (a) D_M = 35 m, (c) D_M = 55 m, and (e) D_M = 75 m. Comparison of strain rate vs. time on three monitor wells at locations of (b) 40 m, (d) 38 m, and (f) 35 m. 88

Figure 5.11. Strain and strain rate maps for different matrix permeabilities. The first row shows (a) strain and (b) strain rate maps of the base case. The second row represents (c) strain and (d) strain rate plots of the case with matrix permeability of 2×10^{-18} m^2. The (e) strain and (f) strain rate plots of matrix permeability of 2×10^{-17} m^2 are shown in the third row. 90

Figure 6.1. Data acquisition schedule. FFS is far-field strain data, and NW is near-wellbore monitoring data. 92

Figure 6.2. (Top) FFS observed at an offset well and (bottom) engineering curves of a single stage. 95

Figure 6.3. Three approaches are used in this work to identify the fracture hit MD: the midpoint of the top and bottom depths of the heart shape, the center line of the fracture hit corridor (blue dotted rectangle), and the midpoint of the blue tail (yellow dash line). 96

Figure 6.4. Processed High-frequency DAS measurements (200-2000 Hz) from a single stage of the monitoring well. The red triangle is the perforation, and the red dash line is the time for diversion. 97

Figure 6.5. Proppant and fluid allocation in each perforation cluster (#1 – #5). 98

Figure 6.6. Production data recorded via DAS workflow in Well A over five days (3-10 Hz). .. 99

Figure 6.7. A schematic of simulation model setup..... 100

Figure 6.8. Comparison of fracture half-length vs. injection time at Well A for different: (top) cluster spacing and (bottom) well spacing. 102

Figure 6.9. Left top: HF-NW-DAS data observed during the treatment of well A; Right top: proppant and fluid allocation, x = percentage, y = perforation number; Bottom row: Enlarged views of the relative position of perforations and fracture hits, red, green, and blue crosses indicate the MD of the fracture hit from well B, C, and D, respectively. 103

Figure 6.10. Comparison of cumulative production vs. injection time for different (top) cluster spacing and (bottom) well spacing. 105

Figure 6.11. HF-NW-DAS (3-10 Hz) recorded at the same stage as the last section in Well A. 106

Figure 6.12. Variation of fracture half-length (a) at perforation clusters after 10 minutes of injection for each PC and (b) over time. 108

Figure 6.13. Plan view of microseismic cloud distribution across all stages. Each stage is represented with a distinct color. Modified from Ortega Perez (2022). 109

Figure 6.14. The schematic of the microseismic cloud length for each stage of well D. Black arrows indicate alternating fracture length. Modified from Ortega Perez (2022). 110

LIST OF SYMBOLS

A	interface area between two adjacent cells, m^2
a	fracture aperture, m
b	Biot's coefficient, dimensionless
$\boldsymbol{C}$	elasticity tensor, Pa
C	space of constant strain modes
C_L	leak-off coefficient, $m/s^{1/2}$
D	distance from the centroid to interface A, m
D_n	normal fracture closure, m
D_{nmax}	maximum normal fracture closure, m
D_M	the distances between the treatment well and the monitor wells, m
E	Young's modulus, GPa
$\boldsymbol{g}$	gravitational vector, m/s^2
g	fluid leak-off volume per unit length of the fracture, m
h	reservoir height, m
$\boldsymbol{k}$	absolute permeability tensor, m^2
k_f	fracture permeability, m^2
k_M	rock permeability, m^2
$k_{r\alpha}$	relative permeability of phase α, dimensionless
K_{dr}	drained bulk modulus, Pa
K_s	the bulk modulus of solid rock grains, Pa
$\boldsymbol{K}$	stiffness matrix

K_{ni}	initial normal stiffness, Pa/m
L_f	fracture length, m
$\boldsymbol{N_C}$	matrix representation of the basic function of the linear spaces C
$\boldsymbol{N_R}$	matrix representation of the basic function of the linear spaces R
P_{Mi}	initial matrix pressure, Pa
p	fluid pressure, Pa
p_{n}	net pressure, Pa
$\boldsymbol{P_C}$	Projection operator on space C
$\boldsymbol{P_R}$	Projection operator on space R
$\boldsymbol{Q}$	matrix for transferring local variables to global variables
Q	flow rate, m^2/s
R	space of rigid body motions
$\boldsymbol{S^E}$	a matrix that guarantees a positive stiffness matrix
S_H	horizontal stress, Pa
$\boldsymbol{t}$	traction, Pa
T	transmissibility, $m^3/(Pa\ s)$
$\boldsymbol{u}$	displacement vector, m
$\boldsymbol{v}_\alpha$	velocity of phase α, m/s
$\boldsymbol{W_C}$	matrix representation in C space of the projections
$\boldsymbol{W_R}$	matrix representation in R space of the projections

Greek Letters:

ρ_α	density of phase α, kg/m^3
$\boldsymbol{\sigma}$	stress tensor, Pa
$\boldsymbol{\sigma}'$	effective stress vector, Pa
σ_c	critical value, Pa
σ_n	normal stress acting on the fracture planes, Pa
$\boldsymbol{\varepsilon}$	strain tensor, dimensionless
ϕ	true porosity, dimensionless
ϕ_M	reservoir porosity, dimensionless
μ_α	viscosity of phase α, Pa s
ν	Poisson's ratio, dimensionless
Γ	the outer boundary of the domain
Ω	computational domain

Acronyms:

BEM	Boundary Element Methods
CVFD	Control Volume Finite Difference
DAS	Distributed Acoustic Sensing
DDM	Displacement Discontinuity Method
DFM	Discrete Fracture Matrix
DFN	Discrete Fracture Network
DOFS	Distributed Optical Fiber Sensor
DP	Dual-Porosity model

DS	Differential Stress
DTS	Distributed Temperature Sensing
FEM	Finite Element Method
FH	Fracture Hit
FHC	Fracture Hit Corridors
FO	Fiber Optic
FVM	Finite Volume Method
KGD	Khristianovich-Geertsma-Deklerk model
LF-DAS	Low-Frequency Distributed Acoustic Sensing
MD	Measured Depth
MPFA	Multi-Point Flux Approximation
MRST	Matlab Reservoir Simulation Toolbox
PC	Perforation Cluster
PKN	Perkins-Kern-Nordgren model
TPFA	Two-Point Flux Approximation
VEM	Virtual Element Method

CHAPTER 1 : INTRODUCTION

1.1 Background and Motivations

Unconventional tight or shale reservoirs have contributed significantly to the global hydrocarbon production with advances in horizontal well drilling and multi-stage hydraulic fracturing techniques (Wang & Chen, 2019). In order to overcome the difficulties of extremely low permeability and relatively low porosity in unconventional reservoir production, a parent-child well drilling with a multi-stage fracturing technique has been developed and has become an important strategy in recent years (Guo et al., 2019; Lin et al., 2018). Parent wells are drilled under initial conditions. Child wells (also called infill wells) are drilled subsequently near the parent wells to decrease well spacing, improve drainage efficiency between wells, and accelerate recovery, as shown in **Figure 1.1**. After a period of production, the stress state around the hydraulic fracture, especially for infill location, may change dramatically, which can affect the flow pattern and, ultimately, the production characteristics of the reservoir (Samier & De Gennaro, 2007). During the infill drilling process, underperformance may occur in infill wells due to the internal interference between each well. Studying fracture interference will help us have a better understanding of optimizing the development strategy of infill wells.

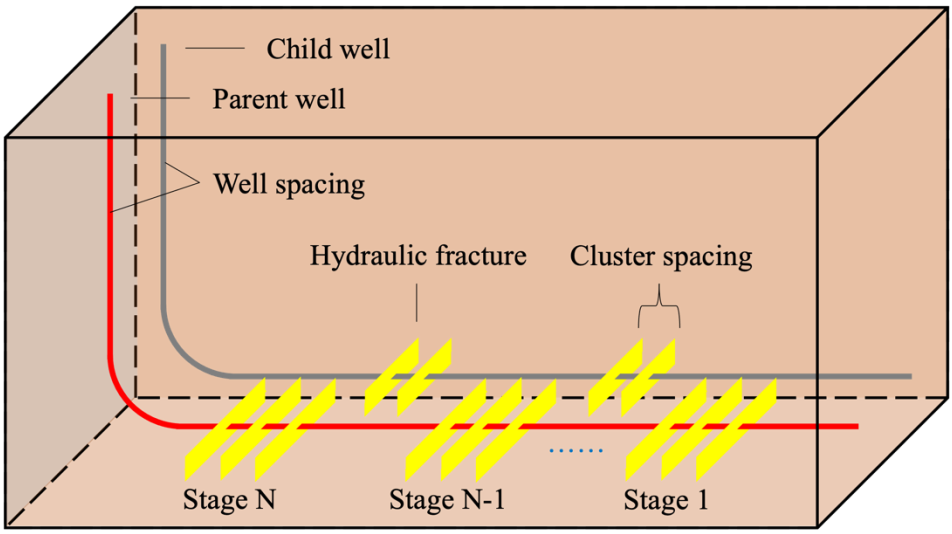

Figure 1.1. A schematic of multiple hydraulic fracturing in parent-child drilling.

Numerical models have been used for simulating stress state changes and pressure depletion distribution due to fracture interference in recent years (Manchanda et al., 2018; Settari et al., 2002; Wu et al., 2018). In the previous work on coupled flow and geomechanical problems, the predominant discretization method is the Finite Element Method (FEM). However, the FEM approach has limitations in computing strain energy on an ill-defined grid due to its dependence on the reference shape factors for mapping between the gird elements (Bower, 2009; Hughes, 2012). The Virtual Element Method (VEM), which is an alternative approach based on the mimetic finite difference method, has been developed. This approach offers the potential to overcome certain limitations associated with FEM and is more suitable for unstructured grid elements and nonorthogonal fractures (Andersen et al., 2017; Gain et al., 2014; Klemetsdal et al., 2017; Nilsen et al., 2018). In the MATLAB Reservoir Simulation Toolbox (MRST), a VEM module is available for solving linear elasticity problems (Beirão da Veiga et al., 2014; Gain et al., 2014). Although it is possible to be coupled with the flow calculation for a single-porosity system (i.e., no fractures),

the coupling of this VEM linear elastic model with flow simulation for a system with discrete fractures is not yet available.

Optimizing completion parameters such as stage length, cluster spacing, and pumping rate, as well as development decisions related to well spacing, is a complex task because many of these elements are interdependent (Ugueto C et al., 2018). Production is the ultimate and most direct measure of completion effectiveness, and conducting production profiling at each perforation cluster can provide critical information on the efficiency of hydraulic fracturing treatments (Ugueto C et al., 2016). Production data (e.g., flow rates, well pressures) are often used to infer or estimate unknown system (model) parameters. This process is described as production history matching, which is an inverse problem with non-unique solutions: uncertain model parameters are perturbed until the model response is consistent with the actual production profiles. In addition to production data, a variety of fracture diagnostic tools can be employed to quantify the stimulation efficiency and other hydraulic fracture properties or characteristics (Warpinski, 1996). Hydraulic fracture diagnostic techniques have received much research interest in recent years. In this work, one of the aims is to investigate the correlation between the coupled model responses and the measurements gathered from one of the major Fiber Optic (FO) based diagnostic technologies – Distributed Acoustic Sensing (DAS).

Inferring hydraulic fracture geometry is an inverse problem and remains challenging due to the complex subsurface conditions (Cipolla & Wright, 2000; Mahmoud et al., 2021; Warpinski, 1996). A better understanding of hydraulic fracture propagation and interference helps optimize well completions design and field development (Jin & Roy, 2017; Ugueto et al., 2019). DAS is one of the important diagnostic techniques to detect and characterize hydraulic fractures (Jin & Roy, 2017; Liu, Wu, et al., 2020; Tan et al., 2020). In addition, FO technology allows continuous

downhole monitoring of production and provides an estimate of production per each perforation cluster (Richards et al., 2015; Ugueto C et al., 2018). In combination with Distributed Temperature Sensing (DTS), DAS has the capacity to visualize and quantify the volumes of injected fluid and proppant at perforations along the entire wellbore (Van der Horst et al., 2014). This knowledge will enhance our ability to integrate DAS, and production data for assessing fracture stimulation efficiency, monitoring interference between wells or fracture hits, and, ultimately, offering insights about optimal design or operations of hydraulic fracturing stimulations.

1.2 Problem Statement

The literature review in the next chapter has revealed several limitations of utilizing coupled flow-geomechanical simulation for analyzing stress/strain responses in hydraulic fracturing and integrating DAS data in the modelling process.

The first problem is the absence of a coupled flow and geomechanics models in a flexible open-source code environment. Moreover, coupling flow and geomechanical simulations to simulate fracture propagation and stress evolution is an ongoing research area. MRST is an open-source reservoir simulation package, which is widely popular among the numerical simulation communities. It has a large collection of flexible and efficient software libraries and data structures. A robust multi-phase flow package is available in MRST for simulating flow responses in DFM; however, coupling that with a linear elastic model is not available yet. In addition, existing modules in MRST cannot simulate the processes of fracture closure and fracture propagation. Hence, the first objective is to construct a coupled model capable of modeling fracture closure/propagation and the associated stress/strain/flow responses. Such a model is essential for analyzing fluid flow and rock deformation in the hydraulic fracturing process.

The second problem is that there is limited simulation work that examines stress reorientation and magnitude changing induced by fracture propagation (during the fracturing/injection stage) and pressure depletion (during the production stage). For example, in the parent-child multi-stage hydraulic fracturing process, stress shadow surrounding hydraulic fractures of the previous stage and inter-well interference between parent and infill wells may affect stimulated reservoir volume and perforation cluster efficiency of infill wells. Thus, the coupled flow and geomechanics model developed in this work can be used for analyzing inter-well interference and exploring the effect of fracture hits on infill well productivity. Insights from this analysis can be used to optimize well spacing and cluster spacing design and to improve productivity prediction capabilities.

The last problem is the absence of correlation between the model responses and fiber optic sensing data. As discussed in the previous section, fiber optic sensing may detect fracture hits and fracture geometry (fracture length, height, width, and density) associated hydraulic fracturing treatments from recorded strain or temperature data. However, much of the existing literature has primarily focused on the acquisition, processing, and qualitative interpretation of such data. Moreover, due to the complex subsurface conditions and potential noise, field DAS results are usually suboptimal and difficult to interpret. The idea is to examine whether the coupled model can be used to reproduce the DAS responses. For example, a valid question would be: can the coupled model predict those unique features associated with fracture hits that are often inferable from DAS data? This would offer an improved quantitative framework for correlating simulation responses with these advanced fracture diagnostics techniques. Finally, numerous studies have explored the positive and negative effects of fracture hits on production and the influence of well interference on fracture geometry. However, these investigations primarily concentrate on the

parent and child well process. The impact of fracture hits on production in scenarios without existing depletion has not been thoroughly investigated.

1.3 Research Objectives

The general goal of this research is to formulate a coupled flow and geomechanical simulation within the MRST framework, and to use the coupled model for simulating the effect of fracture interference on stress evolution and production performance, facilitating improved integration of production responses and fracture diagnostics measurements for fracture characterization. In order to solve the foregoing problems, the corresponding objectives are listed as follows:

(1) Develop a coupled flow and geomechanics simulation model in 2D incorporating the DFM within MRST framework. The flow problem in this model is discretized using the Finite Volume Method (FVM), and the geomechanical discretization is based on the Virtual Element Method (VEM). The solution strategy used in this model is the fixed-stress splitting method.

(2) Combine the fracture deformation model with our coupled flow and geomechanics model to simulate rock deformation and fracture propagation.

(3) Analyze the dynamic-stress evolution and pressure depletion for a parent-child well configuration to study stress-shadow effects and well interference. Analyze the effects of fracture geometry (length and aperture/width), well spacing, cluster spacing on the stress field.

(4) Compare or correlate the predicted strain rate distribution with the waterfall plots obtained from DAS monitoring.

(5) Interpret field measurement DAS data by examining fracture interference, closure, and stress shadowing effects to investigate characteristics of fracture hits from adjacent wells.

(6) Provide insights for optimizing hydraulic fracturing operations (e.g., completions design strategies or infill well placement) by analyzing cluster efficiency.

1.4 Thesis Outline

This thesis consists of 7 chapters, and it is organized as follows:

Chapter 1 presents a general introduction of this thesis including background information and research motivations, problem statement, research objectives and thesis outlines.

Chapter 2 presents a review of the development of hydraulic fracturing models, numerical modeling strategies for fractured media, and distributed acoustic sensing technology. It provides an overview of the background of our study, starting from hydraulic fracturing simulation model development to the optimization of completion design.

Chapter 3 presents the methodology. This work employs a sequentially coupled multi-phase flow and geomechanical simulation model based on the discrete fracture model to simulate flow and stress distribution. The flow problem is discretized using the Finite Volume Method (FVM), and the geomechanical discretization is based on the Virtual Element Method (VEM). The simulation results are compared with the analytical solutions for McNamee-Gibson's and Gu's problems.

Chapter 4 presents the practical implementation of the proposed methodologies. Several case studies demonstrate the utility of the proposed coupling strategy for analyzing production

performance and stress evolution in hydraulically fracturing formations. Furthermore, the factors that impact fracture interference behaviour are examined in this chapter.

Chapter 5 analyzes modelling results to investigate patterns and trends observed in field DAS data. The accuracy of the developed model is validated against the KGD analytical solutions for the leak-off-viscosity and storage-viscosity dominated regimes. Several case studies and sensitivity analyses demonstrate the approach's utility and examine fracture interference, closure, and stress shadowing effects.

Chapter 6 presents several case studies utilizing the in-house numerical simulation model and raw DAS data analysis to explore the effects of cross-well fracture hits and completion designs on fracture propagation and production conductivity.

CHAPTER 2 : LITERATURE REVIEW

2.1 Overview

This chapter presents a review of the development of hydraulic fracturing models, numerical modeling strategies for fractured media, and distributed acoustic sensing technology. It provides an overview of the background of our study, starting from hydraulic fracturing simulation model development to the optimization of completion design.

2.2 Review of the Development of Hydraulic Fracturing Models

Numerous hydraulic fracturing models have been developed to enhance the design of treatments and advance the understanding of certain mechanisms (Chen et al., 2021). This section mainly focuses on the typical two-dimensional models developed during the early years, which assume plane strain conditions and simplify the fracture geometry (Wu, 2014).

2.2.1 KGD Model

The inception of the first simplified theoretical hydraulic fracturing models dates back to the 1950s (Adachi et al., 2007). One well-known model is the KGD model, developed by Khristianovic and Zheltov (1955) and Geertsma and De Klerk (1969). The KGD model assumes plane strain conditions for a fracture in the horizontal plane, with a constant fracture height and no variation in fracture aperture along the vertical axis, as shown in **Figure 2.1**.

The relationship between the fracture aperture a and the net pressure p_n is governed by an integral equation (Garagash, 2006; Sneddon & Lowengrub, 1969),

$$a(x,t) = \frac{4}{\pi E'} \int_0^{L_f} G\left(\frac{x}{L_f}, \frac{x'}{L_f}\right) p_n(x',t) dx', \tag{2.1}$$

where a is the fracture aperture, $E' = E / (1-\nu^2)$ is the plane strain modulus, L_f is the fracture half-length, x is the position along the fracture, t is time, and $p_n = p_f(x, t) - \sigma_0$ is the net pressure, which is the difference between the internal fluid pressure within the fracture and the far-field confining stress. The integral kernel G is expressed as

$$G(\xi,\eta) = ln\left|\frac{\sqrt{1-\xi^2}+\sqrt{1-\eta^2}}{\sqrt{1-\xi^2}-\sqrt{1-\eta^2}}\right|. \tag{2.2}$$

The KGD model is independent of fracture height and is more suitable for short fractures. It is commonly employed during the early injection stages when the fracture height is significantly greater than the fracture length (Adachi et al., 2007; Wu & Olson, 2015b).

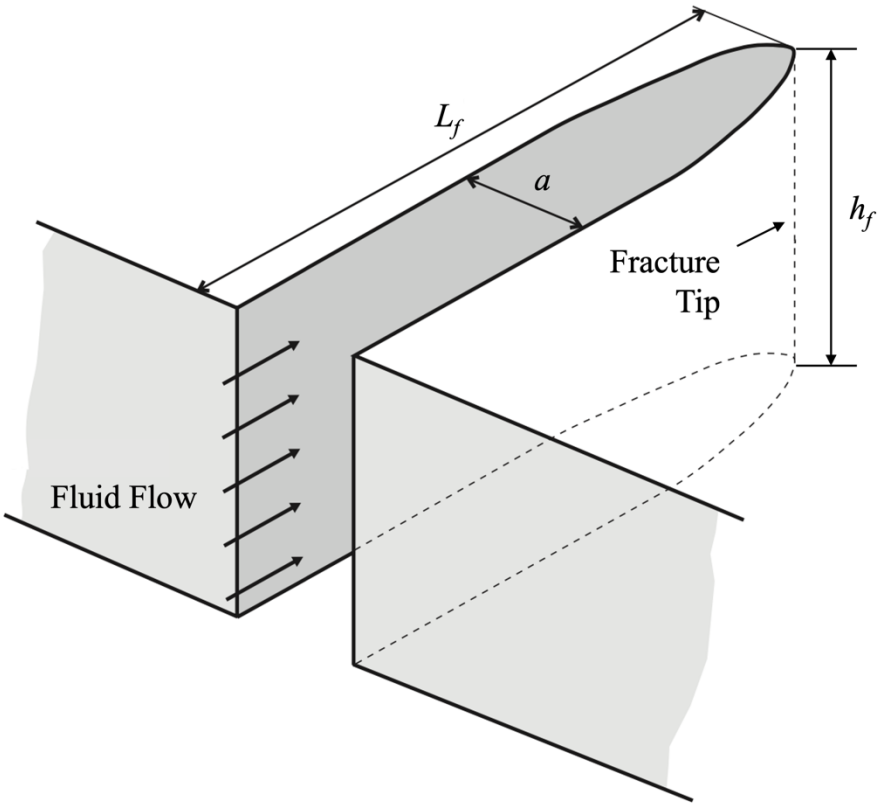

Figure 2.1. Schematic of the KGD model setup. L_f is the fracture half-length, a is the fracture aperture and h_f is the fracture height. Modified from Adachi et al. (2007).

2.2.2 PKN Model

Another well-known hydraulic fracturing model is the PKN model, which came from the work by Perkins and Kern (1961) and Nordgren (1972). The PKN model assumes plane strain conditions; however, in contrast to the KGD model, it specifically considers plane strain for fractures in a vertical plane, with the fracture's vertical cross-section taking on an elliptical shape, as shown in **Figure 2.2**.

The fracture aperture at each vertical section is expressed as (Nordgren, 1972)

$$a(x,t) = \frac{(1-v)}{G}\sqrt{h_f^2 - 4z^2}\,p_n(x,t), \tag{2.3}$$

where G is the bulk shear modulus, ν is the Poisson's ratio, h_f is the fracture height, z represents the coordinate in vertical direction, and p_n is the net pressure, and the variation of p_n with z is neglected here. In this model, the fracture aperture is affected solely by the relative location within the fracture and the local pressure. With these assumptions, the PKN model is suitable for long fractures with limited height and elliptical vertical cross-sections. This implies that the PKN model may be more applicable during the late injection stage when the fracture length exceeds the fracture height (Wu, 2014).

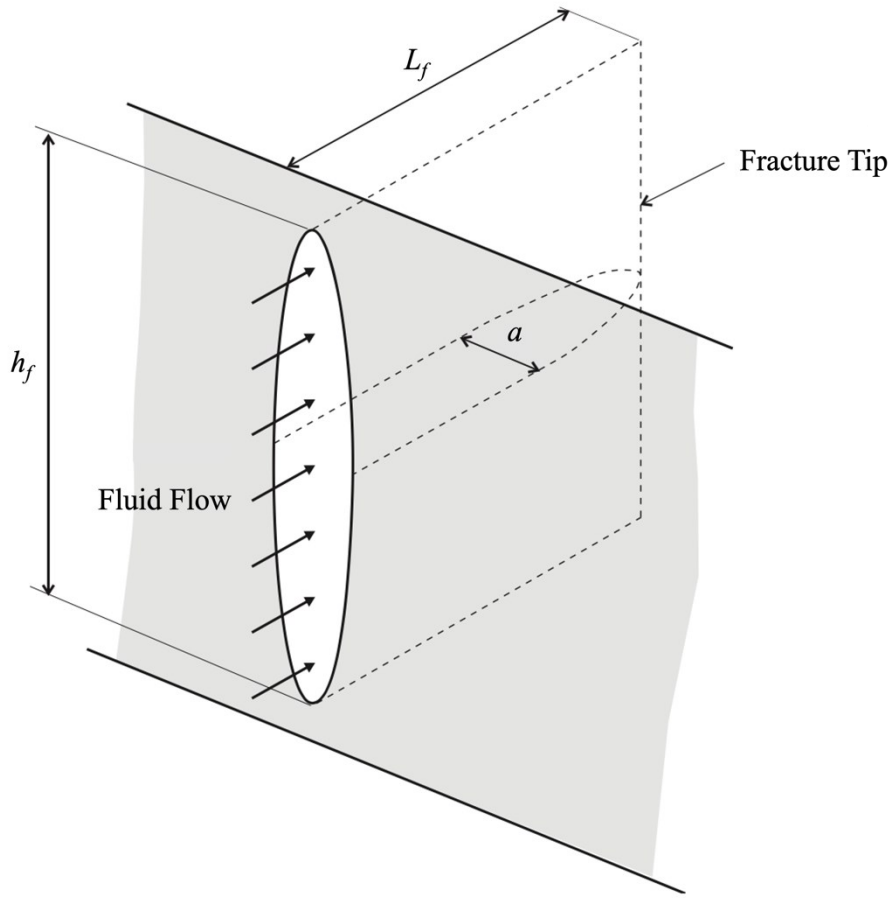

Figure 2.2. Schematic of the PKN model setup. L_f is the fracture half-length, a is the fracture aperture, and h_f is the fracture height. Modified from Adachi et al. (2007).

2.2.3 Radial Model / Penny-Shaped Model

The governing equations for the radial model are similar to the KGD model and were first solved by Sneddon (1946) and Green and Sneddon (1950). This model assumes the wellbore is aligned with the minimum principal stress direction, forming a penny-shaped hydraulic fracture perpendicular to the wellbore (Chen et al., 2021), as shown in **Figure 2.3**. The profile of the fracture is characterized as parabolic rather than elliptical (Geertsma & De Klerk, 1969). The governing equations of the radial model exhibit a similar structure to the KGD model (Geertsma & De Klerk, 1969), the average fracture width can be calculated as (Valkó & Economides, 1995)

$$\bar{a} = 2.24\left(\frac{\mu Q r}{E'}\right)^{1/4}, \tag{2.4}$$

where μ is the fluid viscosity, Q is a constant injection rate, and r is the fracture radius. Different constants are used in the literature depending on the author's preference for applying analogy (Geertsma, 1989).

Traditional two-dimensional hydraulic fracturing models and their variations were commonly employed for treatment designs until the 1990s and are occasionally utilized today (Adachi et al., 2007; Detournay et al., 1990; Valkó & Economides, 1995). However, they have been largely superseded by pseudo-3D (P3D) (Simonson et al., 1978) and planar 3D models (Clifton & Abou-Sayed, 1979; Clifton & Abou-Sayed, 1981) in practical fracture designs. Nevertheless, these classic two-dimensional models continue to play a role in verifying numerical models and enhancing our understanding of the fracture process (Adachi & Detournay, 2008; Bunger et al., 2005; Fu et al., 2013).

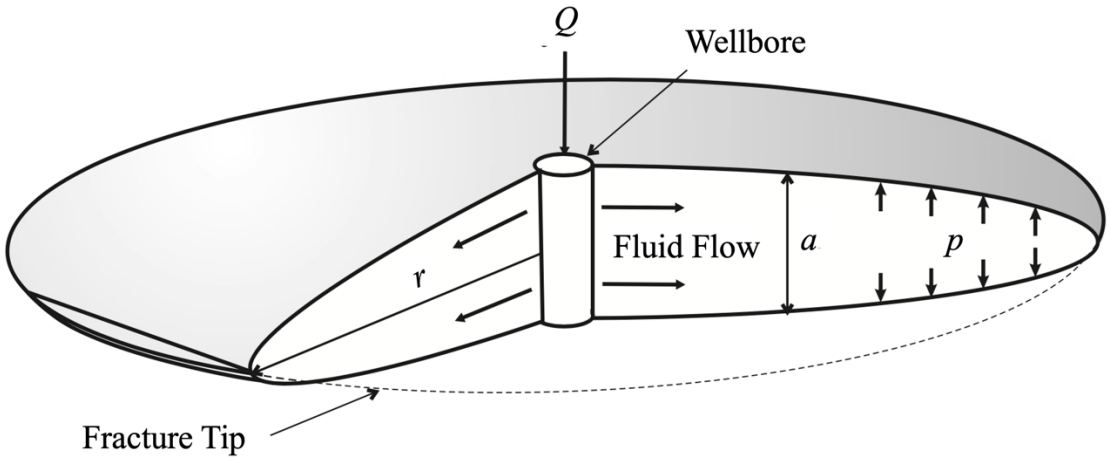

Figure 2.3. Schematic of the radial model setup. *a* is the fracture aperture, *p* is the internal fluid pressure, and *r* is the fracture radius. Modified from Adachi et al. (2007).

2.3 Review of Numerical Model Strategies for Fractured Media

As the complexity of hydraulic fracturing models has increased, the analytical analysis commonly used in early-stage models has proven insufficient for solving the governing equations. In response to these challenges, numerous numerical approaches have been developed to address the complexities involved in advanced hydraulic fracturing models (Chen et al., 2021).

2.3.1 Flow Modelling of Fractured Rocks

- **Dual continuum approach**

One of the most widely adopted methods for simulating multiphase flow through fractured porous media is the dual-porosity (DP) model, which was first developed by Warren and Root (1963). It describes a medium with separate fracture and matrix systems. The dual-porosity model assumes that matrix-to-matrix flow is ignored, while a transfer function is used to model flow between the matrix and fracture network. One of the key assumptions is that the fractures are densely populated, as in the case of naturally fractured reservoirs; however, it often fails to capture the effects of large-scale fractures, such as hydraulic fractures, that are more sparsely populated in the domain (Geiger et al., 2013).

- **Finite element method (FEM)**

There are two main discretization approaches for unstructured fracture networks: finite element and finite volume (or control volume finite difference). Baca et al. (1984) were pioneers in proposing a 2D finite element model for single-phase flow with heat transfer. Juanes et al. (2002) extended the finite element model and proposed a general formulation for 2D and 3D single-phase flow in fractured porous media. Building upon their work, Kim and Deo (2000) and Karimi-Fard and Firoozabadi (2003) extended the finite element method to handle two-phase flow. However,

in the case of multiphase flow in highly heterogeneous reservoirs, these existing FEM models do not ensure local mass conservation (Karimi-Fard et al., 2004).

- **Finite volume method (FVM) / Control volume finite difference (CVFD)**

Existing reservoir simulators are mostly based on finite volume methods. Granet et al. (2001) introduced a cell-based finite volume approach for 2D two-phase flow and specifically addressed the challenge of handling multiphase flow at fracture intersections. Karimi-Fard et al. (2004) applied an unstructured CVFD technique with a two-point flux approximation for flow calculations. Monteagudo and Firoozabadi (2004) presented a control volume approach for simulating two-phase immiscible and incompressible flow in two- and three-dimensional discrete-fractured media.

- **Discrete facture matrix model (DFM)**

The discrete fracture-matrix model was first introduced by Noorishad and Mehran (1982). Sandve et al. (2012) presented the Discrete Fracture Matrix (DFM) model by introducing a Control Volume Finite Difference (CVFD) method with a multi-point flux approximation (MPFA), where discrete fractures are explicitly defined and represented as equi-dimensional objects in the computational domain. The MPFA technique has the advantage of reproducing consistent fluxes for anisotropic permeabilities.

However, in this research, two-point flux approximation (TPFA) is used because isotropic permeability is assumed. Despite its simplicity, the TPFA technique may not be overly susceptible to strong grid orientation errors (Andersen et al., 2017).

2.3.2 Geomechanical Modelling of Fractured Rocks

In general, numerical approaches in geomechanical modelling can be broadly classified into continuum and discontinuum methods (Chen et al., 2021; Hawez et al., 2021; Jing, 2003). The selection of a specific modelling method is influenced by factors such as the scale of the problem and the complexity of the fracture network system. The continuum approach is known for its efficiency in handling large-scale problems, whereas the discontinuum approach excels in accurately integrating complex fracture networks and fragmentation processes (Hawez et al., 2021; Wu & Olson, 2015a).

- **Continuum approaches**
  - **Finite element method (FEM)**

The Finite Element Method (FEM) is the predominant discretization method in most previous coupled flow and geomechanical simulation studies. The term "Finite Elements" was firstly introduced by Clough (1960), and it has been rapidly and widely adopted in various scientific and engineering fields since the 1970s (Zienkiewicz & Morice, 1971).

Garipov et al. (2016) presented a discrete fracture model for coupled flow and geomechanics, combining the finite-volume method and finite-element approximation. Kim et al. (2011) analyzed the stability properties of several sequential-implicit FEM discretization solution strategies for coupled flow and mechanical deformation. Liu, Liu, et al. (2020) developed a coupled model incorporating a DFM to analyze fracturing fluid recovery and in-situ fluid distribution.

  - **Boundary element method (BEM) / Displacement discontinuity method (DDM)**

The BEM is another widely used numerical approach for modeling fracture networks. The displacement discontinuity method (DDM) developed by Crouch (1976) is a variant of the BEM

that relies on discretizing a continuous distribution of displacement discontinuity along a fracture. This method simplifies the elastic problem discretization by focusing only on the fracture elements (Seth et al., 2018; Shrivastava & Sharma, 2018; Wu et al., 2018). Wu and Olson (2015a) presented a simplified three-dimensional DDM by neglecting vertical shear stress and simplifying the discretization in the vertical direction, enhancing computational efficiency and reducing memory usage. Shrivastava and Sharma (2018) simulated hydraulic fracture propagation in the presence of a complex natural fracture system using the three-dimensional DDM. They investigated the effect of different natural fracture attributes and geometries. The main advantage of DDM in comparison to FEM is computational efficiency because only fracture boundaries are discretized, and refinement around fracture tips and re-meshing can be avoided when fractures propagate.

- **Finite difference method (FDM) / Virtual element method (VEM)**

The FDM is an approximation of the governing partial differential equations (PDEs) (Hawez et al., 2021; Jing & Hudson, 2002). The conventional FDMs have limitations in handling material heterogeneity, complicated boundary conditions, and fractures due to the inflexibility (Shojaei et al., 2019).

The Virtual Element Method (VEM) is an alternative approach based on the mimetic finite difference method. This approach offers the potential to overcome certain limitations associated with FEM and is more suitable for unstructured grid elements and nonorthogonal fractures (Andersen et al., 2017; Gain et al., 2014; Klemetsdal et al., 2017; Nilsen et al., 2018).

- **Discontinuum approaches**

- **Discrete element method (DEM)**

The DEM was originally developed by Cundall (1971), which considers the material as an assembly of separate blocks or particles, each bounded by intersecting discontinuities (Khan, 2010;

Lisjak & Grasselli, 2014). The key difference between the DEM and continuum approaches lies in the contact patterns between components. In DEM, the contact patterns continuously change during the deformation process, whereas in continuum-based methods, they remain fixed (Jing, 2003).

The DEM can be classified into two main approaches: explicit and implicit methods. The best-known implementation of explicit DEM is the universal distinct element code (UDEM), created by Cundall (1980) (Cundall, 1988; Inc, 2014). The implicit DEM was represented mainly by the discontinuous deformation analysis (DDA) approach, designed by Shi (1988) and further developed by Shyu (1993) and Chang (1994).

While the DEM offers simplicity and accuracy in simulating geomechanical problems, including intact rock behavior, shearing/opening of pre-existing fractures, and interaction between multiple fractures and blocks (Lei et al., 2017), its computational demands may be excessive compared to continuum approaches (Ferretti, 2020).

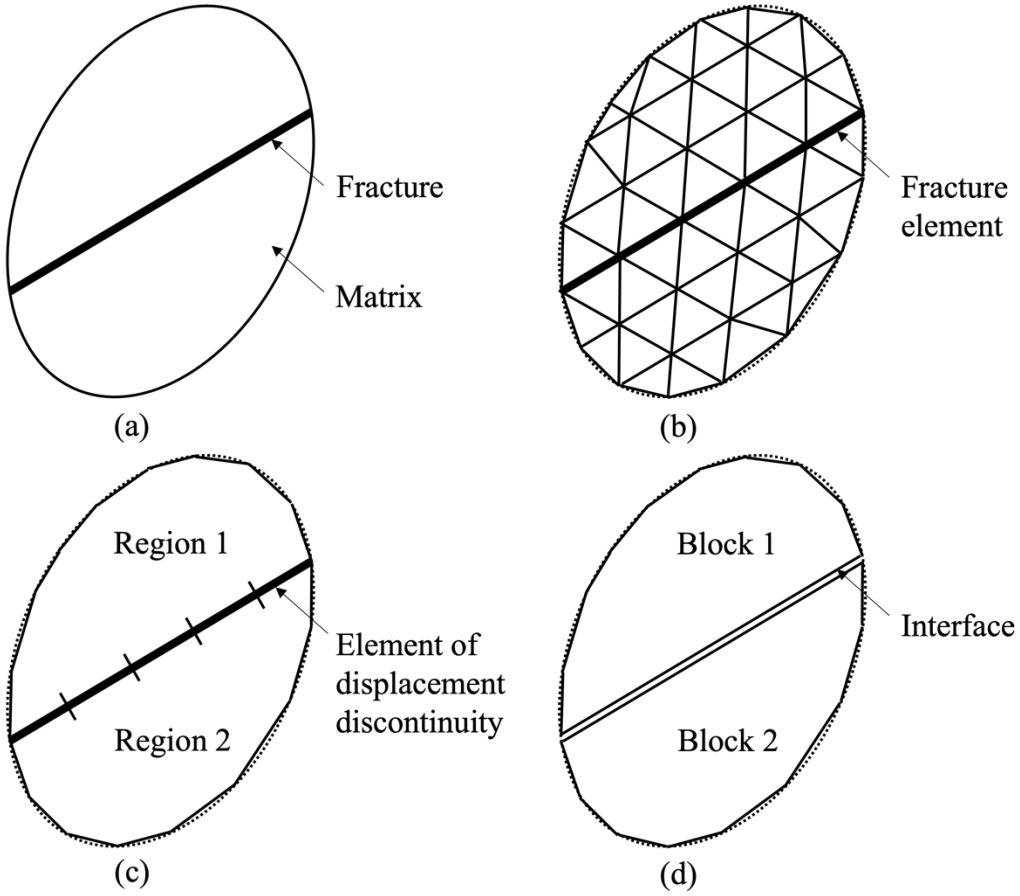

Figure 2.4. Schematic of discretization concepts for (a) the fractured rock mass, (b) FDM or FEM, (c) BEM, and (d) DEM, modified from (Jing, 2003).

2.3.3 Approaches for Coupling Fluid Flow and Geomechanics Simulations

There are several options regarding coupling strategies. Kim et al. (2011) analyzed the stability properties of four sequential-implicit solution strategies: drained split, undrained split, fixed-strain split, and fixed-stress split for coupled flow and mechanical deformation. The analysis indicated that among these methods, the undrained and fixed-stress split schemes were unconditionally stable, and the convergence rate of the fixed-stress split was higher than the undrained split. Andersen et al. (2017) indicated that the fully coupled approach is unconditionally stable but can be computationally expensive, which is not implemented in most existing, highly

sophisticated, commercial simulator software packages. Therefore, for this study, the coupled flow and geomechanical simulation model is based on the fixed-stress split scheme.

2.4 Review of Distributed Acoustic Sensing Technology

2.4.1 Historical Development of Fiber Optic Sensors

Optical fibers have conventionally been engineered to efficiently transmit light over long distances with minimal signal loss and distortion. These characteristics have enabled the development of long-distance broadband optical transmission systems worldwide. Furthermore, the high light confinement and low power losses of optical fibers have also made them highly suitable for various specialized applications, including optical sensing (Fernández-Ruiz et al., 2020).

The development of fiber-optic (FO) sensors began in earnest in 1977 (Giallorenzi et al., 1982). FO sensors have been proved to have notable advantages over traditional electronic sensor, offering unmatched performance in various applications (Fernández-Ruiz et al., 2020). The field of fiber optic sensing was initially introduced through the application of single-point sensors (Molenaar & Cox, 2013). In order to address cost concerns and enable measurement of longer distance, the concept of distributed optical fiber sensor (DOFS) was introduced (Hartog, 2017). DOFSs are capable of measuring a continuous spatial profile of the measurand along the entire length of the sensing fiber, instead of a finite number of discrete locations (Hartog, 2017). This allows for the simultaneous monitoring of a large number of independent sensing points over a single optical fiber (Becker et al., 2020; Fernández-Ruiz et al., 2020).

2.4.2 Distributed Acoustic Sensing Technology

Since the 1990s, oil and gas industry has utilized fiber-optic sensing technology to monitor steam injection, injection profiling, and hydraulic fracture diagnostics (Ghahfarokhi et al., 2019; Karaman et al., 1996; Sierra et al., 2008). Among the various techniques available, Distributed Acoustic Sensing (DAS) stands out as a powerful tool that can greatly impact well surveillance evaluations (Molenaar & Cox, 2013).

DAS is a novel near-wellbore diagnostic technology that can be used from in-well completions to geophysical monitoring (Jin & Roy, 2017; Molenaar et al., 2012). The DAS market was reported recently that it has a consistent and steady growth in recent years and is projected to exceed $2 billion by the year 2025 (Muanenda, 2018). In this method, fiber-optic sensors are permanently or temporarily installed on the outside of the production casing, and laser energy back-scattered by impurities within the silica lattice structure is sent it back to the surface interrogation units to analyze the acoustics, strain, and temperature change (Jin & Roy, 2017; Molenaar & Cox, 2013; Tan et al., 2020; Webster et al., 2013). The working principle for DAS system is illustrated in **Figure 2.5**. The raw DAS data are mostly recorded in the form of an optical phase, which is determined from the interference pattern of the back-scattered light at two neighbouring observation points separated by a certain distance known as the gauge length (Jin & Roy, 2017; Ugueto et al., 2019). The optical phase can be approximated as the axial strain change of the gauge-length fiber, such that it exhibits a linear relationship with the strain rate (Jin & Roy, 2017).

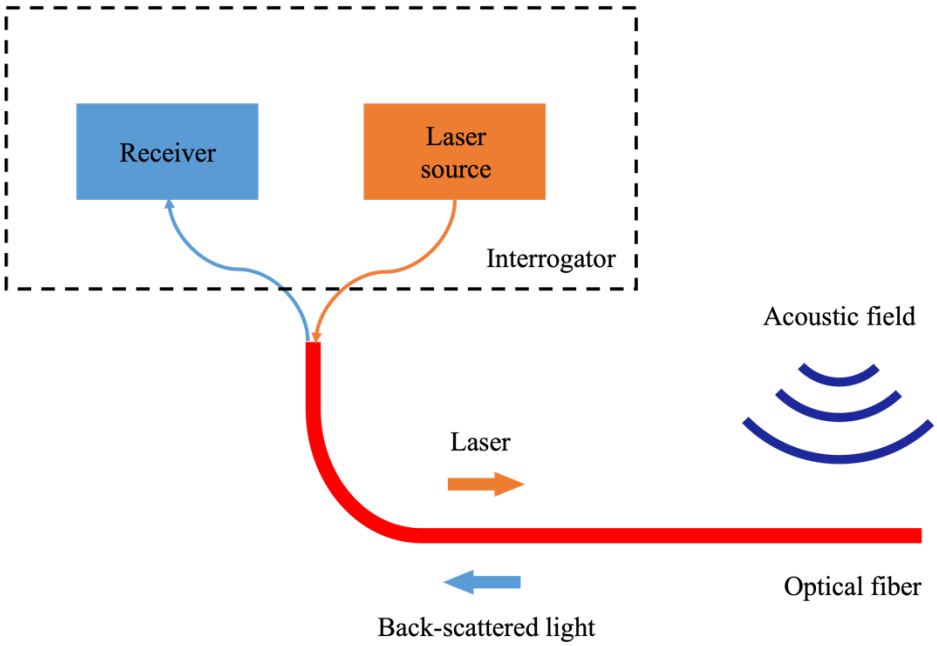

Figure 2.5. Description of working principle for DAS system.

Figure 2.6 (a) illustrates the hypothetical evolution of the DAS response during the progression of a propagating hydraulic fracture as it approaches the monitoring well and eventually intersects with it. At time 1 and time 2, the fracture gradually advances towards the monitoring well, resulting in a narrower strain rate front and a gradual reduction in the extension region, created by tension ahead of the fracture tip (Shahri et al., 2021). The field DAS waterfall plot provides a visual representation of this phenomenon, displaying a distinctive heart-shaped or triangle pattern, as shown in time 1 and time 2 area of **Figure 2.6 (b)**.

When the hydraulic fracture reaches the monitor well at time 3, expansion occurs along the fracture path, resulting in compression of the surrounding rock. Subsequently, as the fracture passes the monitoring well, it continues to open. During time 3 in the DAS waterfall plot, the visual representation of expansion and compression is depicted by the formation of red stripes and blue wings, respectively. These distinct patterns arise because of the net pressure exerted from within the hydraulic fracture (Tan et al., 2020).

At time 4, which corresponds to the cessation of the stimulation pumping, an immediate reversal in the DAS response pattern is observed, forming a blue tail during time 4 in **Figure 2.6 (b)**. This can be attributed to the stress of the surrounding rock formation, causing the hydraulic fracture to initiate closure (Shahri et al., 2021; Zhang et al., 2020).

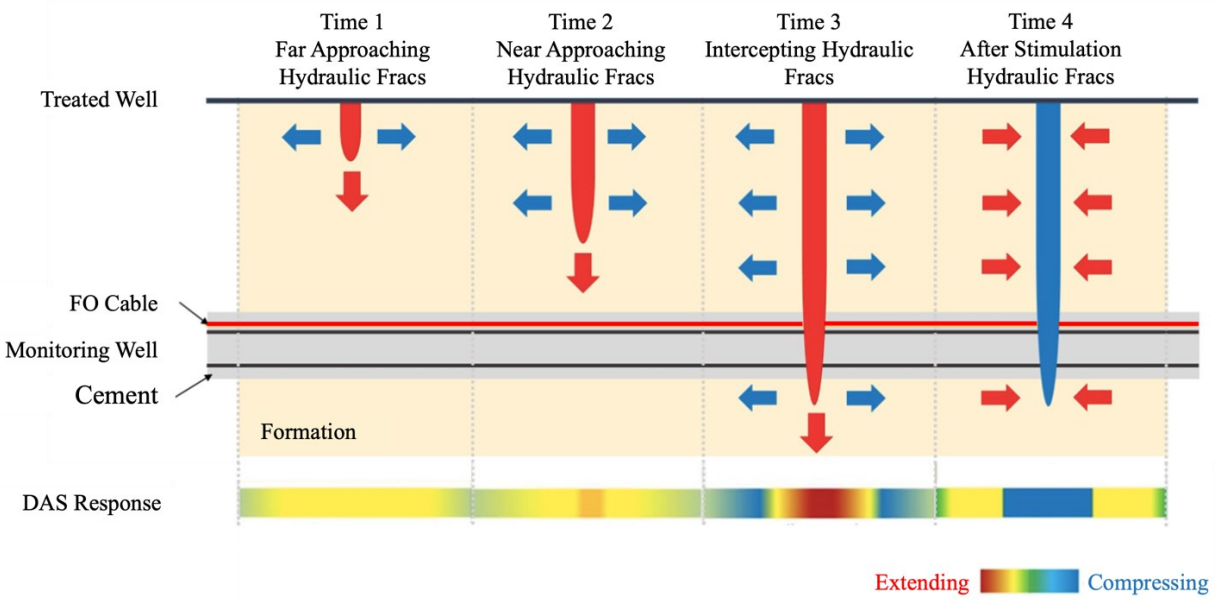

(a) Hypothetical evolution of DAS response of a propagating hydraulic fracture

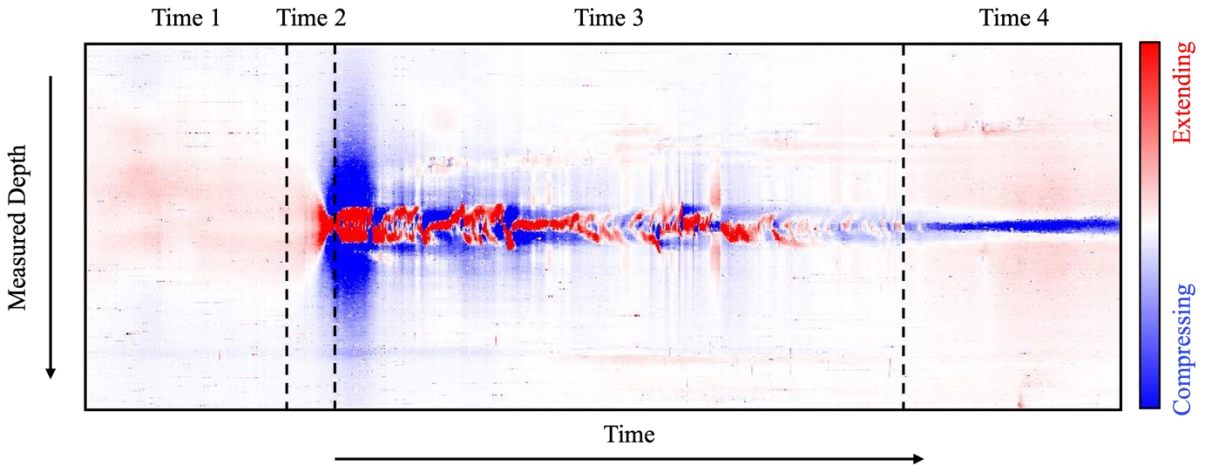

(b) Field LF-DAS waterfall plot

Figure 2.6. (a) Hypothetical evolution of DAS response of a propagating hydraulic fracture, modified from Ugueto et al. (2019) and Ortega Perez (2022). (b) Field LF-DAS waterfall plot.

Fracture diagnostics based on DAS can provide a quantitative assessment of the fluid and proppant placement (Sierra et al., 2008). Molenaar and Cox (2013) presented two case studies using Distributed Temperature Sensing (DTS) and DAS to show how fracture diagnostic technologies help assess the efficiency of open-hole multi-stage and hydraulic fracture stimulation. Jin and Roy (2017) demonstrated that DAS signal in the low-frequency band (<0.05Hz) can effectively capture small and gradual strain variations along the fiber. The low-frequency DAS (LF-DAS) signal proves to be a valuable tool for measuring and characterizing fracture hits and hydraulic fracture geometry, including fracture length, density, and width. Li et al. (2020) measured a variety of physical effects (i.e., temperature, strain, and microseismicity) of 4 wells using DTS and low-frequency DAS data. They discussed its benefits for the fluid and proppant allocations and completion problems. Liu, Wu, et al. (2020) compared numerical simulation results with field DAS measurements for a four-cluster fracture propagation case, while Tan et al. (2020) simulated strain changes for horizontal and vertical FO setups to interpret fracture geometry in the DAS data and optimize completion designs. All the researchers mentioned above agree that the DAS diagnostic technology can provide better insights into open-hole completion stimulation effectiveness and proppant placement designs.

2.4.3 Interpretations of DAS Data and the Impact on Optimization of Completion Design

Optimizing completion design is a complex task because of many interdependent system variables and considerations (Ugueto C et al., 2018). Production is the most direct measure of completion effectiveness, and conducting production profiling at each perforation cluster can provide critical information on the efficiency of hydraulic fracturing treatments (Ugueto C et al., 2016). A better understanding of stimulated fracture geometry is also important for optimizing

well production and hydraulic fracturing treatments (Jin & Roy, 2017). A promising option for achieving continuous observation of fracture geometry and well productivity is the implementation of DAS technology, which allows continuous downhole monitoring of production and provides an estimate of production per each perforation cluster (Richards et al., 2015; Van der Horst et al., 2014).

Several researchers have presented interpretations of the DAS deployment and investigations of the field data recorded by the DAS system. Molenaar et al. (2012) presented the results of initial investigations into the DAS data from its first downhole deployment. The presented case studies, from the surface interrogator systems to hydraulic fracture monitoring, demonstrated the utility of the DAS technique for monitoring dynamic changes during hydraulic fracturing treatment and optimization of completion design. Ugueto et al. (2019) showed several examples of DAS waterfall plots in wells stimulated in the Montney Formation via a variety of completion systems. DAS data was utilized in their paper to enhance understanding of fracture geometry and optimize stage offsetting and well azimuth strategies by mapping hydraulic fracture azimuths. Wu et al. (2020) introduced a new concept, the Frac Hit Corridor (FHC), to identify fracture hits (it is also referred to as far-field strain, FFS) and evaluate hydraulic fracture efficiency. In order to enhance the understanding of the complex impact of fracture interference between parent-child wells, as well as to validate the hypotheses derived from the field data process, it is imperative to perform numerical simulations.

Tan et al. (2020) simulated strain changes for horizontal and vertical FO setups to interpret fracture geometry in the DAS data and optimize completion designs. In both cases, strain and strain rate waterfall plots of strain rate vs. time were compared against the field DAS signals. Zhang et al. (2020) simulated cross-well strain and strain rate responses on horizontal and vertical

monitoring wells. Y. Liu et al. (2021) compared numerical simulation results with field DAS measurements for a four-cluster fracture propagation case to propose a guideline for fracture-hit detection. A set of field case studies were further interpreted by the conclusions drawn from the numerical simulations. However, their studies focused primarily on scenarios of fracture hits due to a single hydraulic fracture. They did not provide detailed interpretations of the effects of multiple wells on fracture growth and well productivity at the monitoring well.

The impact of fracture hits from child wells on parent wells has been discussed by many researchers. Pankaj (2018) subdivided fracture hits into three different forms: fluid fracture hit, propped fracture hit, and pressurized fracture hit, and presented their positive and negative impacts on the productivity of the parent wellbore. Lindsay et al. (2018) analyzed production data from major US unconventional basins, including the Bakken, Barnett, Eagle Ford, and others. The study found that, in most cases, parent wells exhibited higher oil and gas production than infill wells, indicating that infill wells may negatively impact production. Gupta et al. (2021) conducted a critical review of fracture-hit impacts and factors that affect the extend of fracture hits. The studies conducted by the aforementioned researchers primarily focused on analyzing production data from the entire wellbore. On the other hand, by utilizing DAS technology, it is possible to obtain more detailed information on the production characteristics of each stage or each perforation cluster, which can lead to more effective stimulation optimization strategies.

CHAPTER 3 : STATIC MODEL SETUP AND VALIDATION

3.1 Overview

In this chapter, the methodology is presented. This work employs a sequentially coupled multi-phase flow and geomechanical simulation model based on the discrete fracture model to simulate flow and stress distribution. The flow problem is discretized using the Finite Volume Method (FVM), and the geomechanical discretization is based on the Virtual Element Method (VEM). The simulation results are compared with the analytical solutions for McNamee-Gibson's and Gu's problems (Gu et al., 2014; Moradi et al., 2017). To the best of the author's knowledge, although many methods for modeling hydraulic fracturing have been proposed, no such models have been implemented in the MRST framework, where flow and geomechanical computations are solved based on fixed-stress splitting in a DFN model.

3.2 Mathematical Model

3.2.1 Governing Equations

The governing equations are based on the conservation of mass and linear elasticity for coupled flow and geomechanics simulation. The isothermal multi-phase flow of a slightly compressible fluid and small deformation in the reservoir is considered, and the mass balance for each phase α can be expressed as

$$\frac{\partial(\rho_\alpha \phi)}{\partial t} + \nabla \rho_\alpha \boldsymbol{v}_\alpha - R_\alpha = 0, \tag{3.1}$$

where ρ_α is the density of phase α, and ϕ is the true porosity. $\rho_\alpha \boldsymbol{v}_\alpha$ is the mass flux of phase α, and R_α is the rate of appearance. The velocity for each phase is described by Darcy's law:

$$\boldsymbol{v}_\alpha = -k_{r\alpha}\frac{\boldsymbol{k}}{\mu_\alpha}(\nabla p_\alpha - \rho_\alpha \boldsymbol{g}), \tag{3.2}$$

where $k_{r\alpha}$ is the relative permeability of phase α, $\boldsymbol{k}$ is the absolute permeability tensor, μ_α is the viscosity of phase α, p_α is the pressure of phase α, and $\boldsymbol{g}$ is the gravitational vector. The governing equation for the geomechanics model is the conservation of linear momentum for a porous continuum, and for a quasi-static state, the acceleration term is zero:

$$\nabla \boldsymbol{\sigma} + \rho_b \boldsymbol{g} = 0, \tag{3.3}$$

where $\boldsymbol{\sigma}$ is the total stress tensor, $\rho_b = (1-\phi)\rho_s + \phi\rho_f$ is the bulk density, ρ_s is the solid skeleton density, $\rho_f = \sum_\alpha f_\alpha \rho_\alpha$ is the fluid density, and f_α is the volume fraction of phase α. Assuming infinitesimal deformation, the relationship between volumetric strain ε_v and linearized strain tensor $\boldsymbol{\varepsilon}$, volumetric stress σ_v and Cauchy stress tensor $\boldsymbol{\sigma}$, can be expressed as:

$$\varepsilon_v = tr(\boldsymbol{\varepsilon}), \sigma_v = \frac{1}{3}tr(\boldsymbol{\sigma}). \tag{3.4}$$

Strain-displacement relation can be reduced to the linearized strain tensor:

$$\boldsymbol{\varepsilon} = \frac{1}{2}(\nabla \boldsymbol{u} + \nabla^T \boldsymbol{u}) = \frac{1}{2}\left(\frac{\partial u_i}{\partial x_j} + \frac{\partial u_j}{\partial x_i}\right), \tag{3.5}$$

where $\partial u/\partial x$ represents the displacement gradient tensor, and the subscript i and j refer to the Cartesian coordinate system.

3.2.2 Constitutive Relations

Under the premise of isothermal flow and infinitesimal deformation assumption, the stress-strain relation can be written as

$$\boldsymbol{\sigma} - \boldsymbol{\sigma_0} = \boldsymbol{C\varepsilon} - b(p - p_0)\boldsymbol{I}, \tag{3.6}$$

where $\boldsymbol{C}$ is the fourth-order tensor of skeleton tangent elastic stiffness modulus, $\boldsymbol{C\varepsilon} = \boldsymbol{\sigma'}$ is the effective stress vector, $b = 1 - K_{dr}/K_s$ is the Biot coefficient, K_{dr} is the drained bulk modulus, K_s is the bulk modulus of solid rock grains, $p = \sum_\alpha s_\alpha p_\alpha$ is average fluid pressure in the case of multi-phase flow, s_α is the saturation of the phase α, $N = K_s/(b - \phi_0)$ is the Biot tangent modulus that is a function of pressure variation and porosity variation, and the subscript "0" refers to the reference state. At isotropic state, the above equation can be re-written as:

$$(\sigma_v - \sigma_{v0}) = K_{dr}\varepsilon_v - b(p - p_0). \tag{3.7}$$

Substitution of **Eq. 3.7** and the definition of Biot coefficient b and Biot tangent modulus N in **Eq. 3.8** [Detailed derivations can be found in Coussy (2004)] would yield **Eq. 3.9**:

$$\phi - \phi_0 = b\varepsilon_v + \frac{1}{N}(p - p_0), \tag{3.8}$$

$$\phi = \phi_0 + \frac{b}{K_{dr}}(\sigma_v - \sigma_{v0}) + \frac{b + (b-1)\phi_0}{K_{dr}}(p - p_0). \tag{3.9}$$

Eq. 3.9 describes the coupling between pressure and stress, where the solution of both variables will be coupled based on the fixed-stress split method.

3.2.3 Fracture Deformation Mechanism

The original MRST package used in this work has a limitation in that it only supports the coupling of flow and geomechanical calculation for a single porosity system (i.e., no fractures). We extended the capabilities of the code by incorporating explicit representation of discrete fractures in the computational domain and enabling the coupling of flow and geomechanical calculations. Additionally, we introduced a fracture deformation function to accurately capture the behaviour of fractures during the process of treatment. The fracture properties are modelled as a function of stress. As pressure depletes, the space between two fracture surfaces is compressed,

reducing the fracture aperture. A stress-dependent empirical model for fracture deformation is used to simplify the calculation and reduce the computational cost. A hyperbolic model presented by Bandis et al. (1983) and Barton et al. (1985) is used to simulate the normal fracture closure:

$$D_n = \frac{D_{nmax}\sigma_n'}{\sigma_n' + K_{ni}D_{nmax}}, \tag{3.10}$$

where D_n is the normal fracture closure, D_{nmax} is the maximum fracture normal closure, σ_n' is the effective normal stress acting on the fracture plane, and K_{ni} is the initial normal stiffness. In comparison to normal stress, the effect of shear stress on fracture flow is negligible; hence, only the normal fracture deformation is considered in this work. The effective normal stress is defined as:

$$\sigma_n' = \sigma_n - bP_p, \tag{3.11}$$

where σ_n is the normal total stress acting on the fracture plane, and P_p is the pore pressure. Incorporating D_n, the fracture aperture is updated according to the following relationship:

$$a = a_i - \frac{D_{nmax}\sigma_n'}{\sigma_n' + K_{ni}D_{nmax}}, \tag{3.12}$$

Combining the Poiseuille law and the cubic law, fracture permeability is given by

$$k_f = k_{fi}\left(\frac{a}{a_i}\right)^2. \tag{3.13}$$

3.2.4 Boundary Conditions

In this work, only the matrix deformation is considered. Therefore, for the mechanics problem, the fracture surfaces corresponding to each fracture are treated as fixed internal boundaries (Γ_f). The traction force on a fracture surface is defined as the projection of effective stress on the normal vector. The fracture is assumed to be in mechanical equilibrium, where the

two fracture surfaces are separated only by the fluid pressure. The total tractions can be written as follows:

$$t_N^+ = -t_N^- = t_N, \tag{3.14}$$

where t_N is traction along the normal direction. The signs (+, -) denote the two surfaces of a fracture (Jiang & Yang, 2018; L. Liu et al., 2021). It should be noted that the fracture permeability is updated using **Eq. 3.13** after the geomechanical calculation is completed. In other words, although the positions of the fracture surfaces are fixed, the effect of fracture closure is captured by the reduction in fracture permeability, which, in turn, would affect the flow (i.e., pressure and velocity) calculations.

For the flow problem, a fixed flux ($\overline{\boldsymbol{v_\alpha}}$) boundary is imposed along Γ_q, a fixed pressure ($\overline{p_\alpha}$) boundary is imposed along Γ_p, and a fixed bottom hole pressure ($\overline{p_{wf}}$) boundary is imposed along the inner boundary Γ_w. We assume that $\Gamma_q \cap \Gamma_p = \emptyset$ and $\Gamma_q \cup \Gamma_p = \Gamma$, where Γ is the outer edge of the domain. For the mechanical problem, a fixed displacement ($\overline{\boldsymbol{u}} = 0$) boundary is defined along Γ_u, while fixed traction ($\overline{\boldsymbol{t}}$) boundary is defined along Γ_t. We assume that $\Gamma_u \cap \Gamma_t = \emptyset$ and $\Gamma_u \cup \Gamma_t = \Gamma$. The boundary conditions for this particular problem are shown in **Figure 3.1**, and can be expressed as:

$$\begin{gathered}
\boldsymbol{u} = \overline{\boldsymbol{u}}\,,\ \boldsymbol{\sigma}\cdot\boldsymbol{n} = \overline{\boldsymbol{t}} \text{ on outer boundaries } \Gamma_u \text{ and } \Gamma_t \text{, respectively,} \\
\boldsymbol{\sigma}\cdot\boldsymbol{n} = \boldsymbol{t}_N \text{ on inner boundary } \Gamma_f. \\
\boldsymbol{v_\alpha}\cdot\boldsymbol{n} = \overline{\boldsymbol{v_\alpha}},\ p_\alpha = \overline{p_\alpha} \text{ on outer boundaries } \Gamma_q \text{ and } \Gamma_p \text{, respectively,} \\
p = \overline{p_{wf}} \text{ on inner boundary } \Gamma_w.
\end{gathered} \tag{3.15}$$

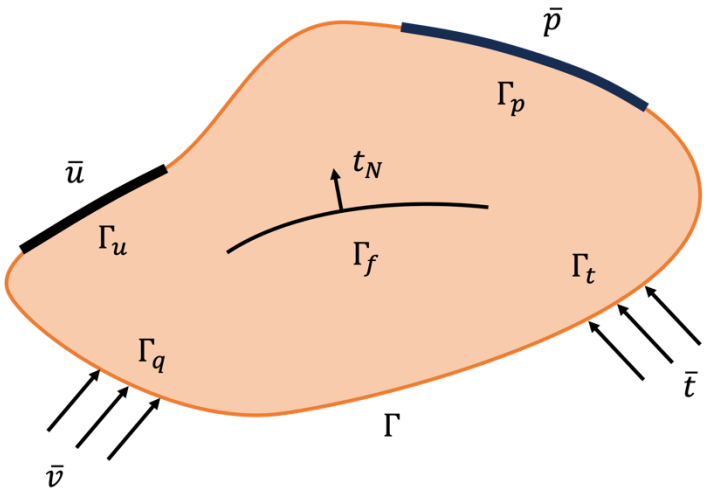

Figure 3.1. Boundary conditions for a fractured porous medium.

3.3 Discretization and Solution Strategy

The numerical strategies of the coupled flow and geomechanics computations in 2D or 3D are discussed. First, an integral grid structure is created. Next, the flow equation is solved based on the finite volume method, while the virtual element method is used to solve the geomechanical problem. Finally, a sequentially coupling strategy based on the fixed-stress splitting method is implemented to iterate between the flow and geomechanical calculations within a time step.

All computations are implemented within the MATLAB Reservoir Simulation Toolbox (MRST) framework. MRST is an open-source reservoir simulation package offering an extensive collection of flexible and efficient software libraries and data structures that can be adapted for specific research purposes (Lie, 2019).

3.3.1 Grid Structure

For the flow calculation, the discrete fractures are lower-dimensional objects in the geometric grid but are explicitly represented as equidimensional objects in the computational

domain. The DFM model can be used for both unstructured and structured meshes in MRST. The fracture is discretized into a series of interface segments between adjacent matrix elements. An example is shown in **Figure 3.2** (a). Although the existing MRST implementation can couple the flow and geomechanics computations, it is incompatible with the DFN grid structure. If a DFN grid structure is used, only the flow computations can be performed (i.e., the simulation cannot handle the additional fracture interfaces between two adjacent matrix cells). For the geomechanical calculation, the fractures should be implicitly represented in both the geometric and the computational domains, as shown in **Figure 3.2** (b), and the fracture surfaces are treated as the internal boundaries for the geomechanical problem. Therefore, the MRST source code is modified to create indexes and nodes for all fracture cells that are consistent with those for the adjacent matrix cells, as well as to ensure consistency between the flow and geomechanical problem variables. For the flow problem, the unknown fluid pressure is located at the centroid of a matrix or fracture cell, while for the geomechanical problem, the unknown displacement is located at the vertex of every matrix element.

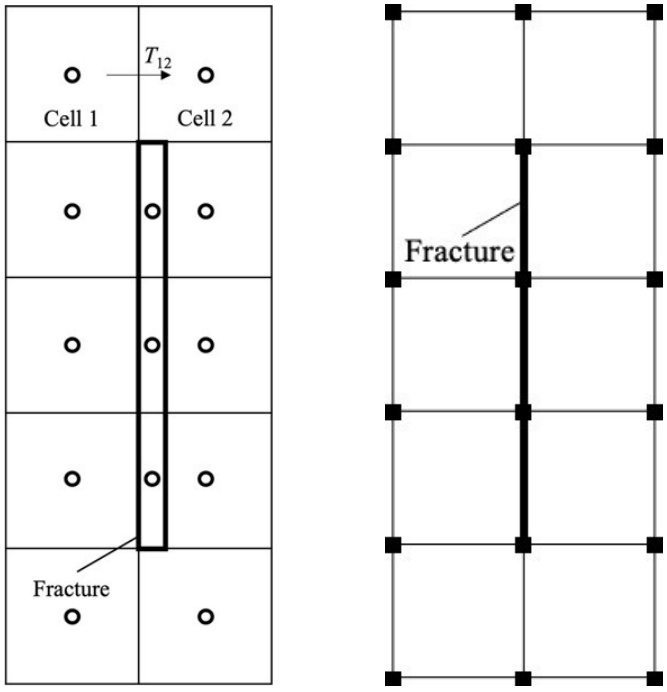

(a) (b)

Figure 3.2. The computational grid structure for (a) the flow problem and (b) the geomechanics problem. The white circle marks the pressure variables, and the black square represents the displacement variables.

3.3.2 Finite Volume Discretization of Flow Equations

Applying the implicit Euler method for time, formulating **Eqs. 3.1** and **3.2** for a control volume would yield **Eq. 3.16** for control volume 1

$$\frac{\Delta V_1}{\Delta t}(\rho_{\alpha 1}^{n+1}\phi_1^{n+1} - \rho_{\alpha 1}^{n}\phi_1^{n}) + \sum Q_{\alpha 12} = R_{\alpha 1}\Delta V_1, \tag{3.16}$$

where ΔV is the control volume, n+1 is a new time step, while n is the old time step. $Q_{\alpha 12}$ is the flow rate from cell 1 to its adjacent cell 2 of phase α in **Figure 3.2**. A two-point flux approximation method is used to calculate the transmissibility, which can be expressed as

$$T_{12} = \left(\frac{1}{\frac{A_1 k_1}{D_1}} + \frac{1}{\frac{A_2 k_2}{D_2}} \right)^{-1}, \tag{3.17}$$

where k_i is the permeability of cell i, A_i is the surface area of cell i, and D_i is the distance from the centroid to A_i. Therefore, the total flow rate $Q_{\alpha 12}$ between two adjacent cells is given by

$$Q_{\alpha 12} = T_{12}\lambda_{\alpha}(p_{\alpha 2} - p_{\alpha 1}), \tag{3.18}$$

where λ_{α} is the fluid mobility of phase α, defined as the ratio of fluid density to fluid viscosity. **Eq. 3.18** is used to compute the matrix-matrix, matrix-fracture, and fracture-fracture connections. The star-delta transformation computes the connections between intersecting fracture elements (Karimi-Fard et al., 2004).

3.3.3 Discretization for Mechanical Problems.

In MRST, the geomechanical problem is solved using the virtual element method (VEM), which is a generalization of the standard finite element method (FEM) for arbitrary polytopal meshes, where the local shape function space in each element is defined implicitly (Mengolini et al., 2019). The method was more suited to handle arbitrarily shaped polygonal and polyhedral elements, which are especially convenient for meshing complex DFN geometries.

Multiplied by a virtual work $\delta\boldsymbol{u}$ and integrated over the whole domain, the weak form of **Eq. 3.3** becomes

$$\int_{\Omega} \delta\boldsymbol{u}_i[-\frac{\partial\sigma_{ij}}{\partial x_j} - \rho_b\boldsymbol{g}]d\Omega = 0. \tag{3.19}$$

Apply the divergence theorem to **Eq. 3.19** would yield:

$$\int_{\Omega} \boldsymbol{\sigma}_{ij}\delta\boldsymbol{\varepsilon}_{ij}d\Omega - \int_{\Gamma_t} \overline{\boldsymbol{t}_N}\delta\boldsymbol{u}_i d\Gamma - \int_{\Gamma_f} \boldsymbol{t}_N\delta\boldsymbol{u}_i d\Gamma - \int_{\Omega} \delta\boldsymbol{u}_i\rho_b\boldsymbol{g}d\Omega = 0. \tag{3.20}$$

Substituting **Eq. 3.6** into **Eq. 3.20**, the strain energy term of **Eq. 3.20** can be represented as

$$\int_{\Omega} \boldsymbol{\sigma}_{ij}\delta\boldsymbol{\varepsilon}_{ij}d\Omega = \int_{\Omega} \boldsymbol{\sigma}'_{ij}\delta\boldsymbol{\varepsilon}_{ij}d\Omega - \int_{\Omega} bp\delta_{ij}\delta\boldsymbol{\varepsilon}_{ij}d\Omega. \tag{3.21}$$

Therefore, the final weak form can be written as

$$\begin{aligned}\int_{\Omega} \boldsymbol{\sigma}'_{ij}\delta\boldsymbol{\varepsilon}_{ij}d\Omega - \int_{\Omega} bp\delta_{ij}\delta\boldsymbol{\varepsilon}_{ij}d\Omega - \int_{\Gamma_t} \overline{\boldsymbol{t}_N}\delta\boldsymbol{u}_i d\Gamma - \int_{\Gamma_f} \boldsymbol{t}_N\delta\boldsymbol{u}_i d\Gamma \\ = \int_{\Omega} \delta\boldsymbol{u}_i\rho_b\boldsymbol{g}d\Omega,\end{aligned} \tag{3.22}$$

where $\delta_{ij} = [1,1,0]^T$ in 2D and $[1,1,1,0,0,0]^T$ in 3D. The associated virtual strain field $\delta\boldsymbol{\varepsilon}$ is defined as

$$\delta\boldsymbol{\varepsilon} = \delta\boldsymbol{\varepsilon}_{ij} = \frac{1}{2}\left(\frac{\partial\delta u_i}{\partial x_j} + \frac{\partial\delta u_j}{\partial x_i}\right). \tag{3.23}$$

An approximation of the bilinear energy form associated with an element E is computed as follows:

$$a_E(\boldsymbol{u}, \delta\boldsymbol{u}) = \int_E \boldsymbol{\sigma}(\boldsymbol{u}){:}\,\boldsymbol{\varepsilon}(\,\delta\boldsymbol{u})d\Omega = \int_E \boldsymbol{\sigma}_{ij}\delta\boldsymbol{\varepsilon}_{ij}d\Omega. \tag{3.24}$$

A detailed derivation of the stiffness matrix can be found in Gain et al. (2014). The final local stiffness matrix is given by

$$\boldsymbol{K}_h^E = a_h^E(\varphi_i, \varphi_j) = |E|\boldsymbol{W}_c^T\boldsymbol{D}\boldsymbol{W}_c + (\boldsymbol{I} - \boldsymbol{P})^T\boldsymbol{S}^E(\boldsymbol{I} - \boldsymbol{P}). \tag{3.25}$$

The global stiffness matrix is then given by

$$\boldsymbol{K} = \boldsymbol{Q}^T\boldsymbol{K}_h^E\boldsymbol{Q}, \tag{3.26}$$

where $\boldsymbol{P} = \boldsymbol{P}_C + \boldsymbol{P}_R$, $\boldsymbol{P}_R = \boldsymbol{N}_R\boldsymbol{W}_R^T$, $\boldsymbol{P}_C = \boldsymbol{N}_C\boldsymbol{W}_C^T$. $\boldsymbol{N}_C$ and $\boldsymbol{N}_R$ are matrix representations of the basis function of the linear spaces R and C, respectively, where R and C refer to the spaces of rigid body motions and constant strain modes. $\boldsymbol{W}_C$ and $\boldsymbol{W}_R$ are the matrix representations in these spaces of the projections. Matrices $\boldsymbol{P}_C$ and $\boldsymbol{P}_R$ are projections onto the range of $\boldsymbol{N}_C$ and $\boldsymbol{N}_R$, respectively. $\boldsymbol{S}^E$ is a symmetric positive matrix that guarantees positivity of the stiffness matrix, the choice of

$\boldsymbol{S}^E$ can be found in Gain et al. (2014). $\boldsymbol{D}$ is a function of the elasticity tensor $\boldsymbol{C}$. $\boldsymbol{Q}$ is the matrix for transferring local variables to global variables. In summary, the stiffness matrix can be calculated from $\boldsymbol{N}_C$, $\boldsymbol{N}_R$, $\boldsymbol{W}_C$ and $\boldsymbol{W}_R$.

The body force caused by gravity can be ignored in 2D cases, and the weak form (**Eq. 3.22**) can be simplified as

$$\boldsymbol{K}\boldsymbol{u} + b \cdot (\mathrm{Tr}\boldsymbol{W}_c\boldsymbol{Q})^T p = \boldsymbol{t}_N + \overline{\boldsymbol{t}_N}, \tag{3.27}$$

3.3.4 Solution Strategy

The fixed-stress splitting method is generally stable and exhibits satisfactory convergence behaviour (Kim et al., 2011). The flow equations are solved first by freezing the temporal change of the total volumetric stress:

$$\left(\frac{\partial \sigma_v}{\partial t}\right)_n = \left(\frac{\partial \sigma_v}{\partial t}\right)_{n+1}. \tag{3.28}$$

Therefore, **Eq. 3.9** can be simplified to

$$\phi = \phi_0 + \frac{b + (b-1)\phi_0}{K_{dr}}(p - p_0). \tag{3.29}$$

The scheme can be summarized as follows: (1) Solving **Eqs. 3.1** and **3.2** for the flow problem to obtain p^{n+1}; (2) Solving **Eq. 3.27** for the geomechanical problem using p^{n+1} from step (1). This process is repeated until the whole coupled solution converges. The resulting pressure is then used to update porosity for the new time step using **Eq. 3.29**. The updated porosity is used to solve the flow problem for the next time step. The fracture aperture and permeability are also re-calculated to update the transmissibility at the end of each time step. The flow chart is shown in **Figure 3.3**.

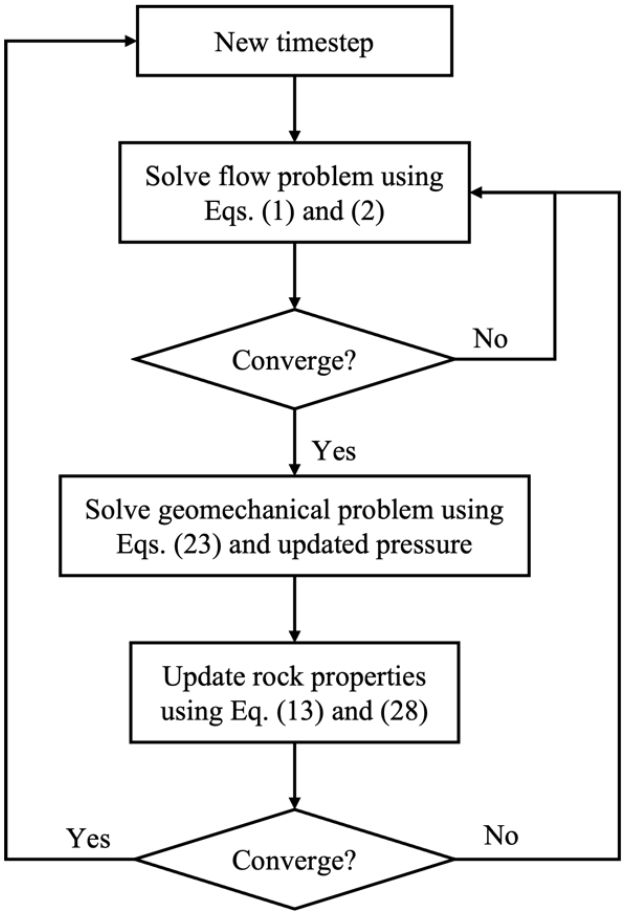

Figure 3.3. Flow chart for the present coupled model.

3.4 Model Validation

3.4.1 McNamee Gibson's Problem

The accuracy of the coupled flow and geomechanics numerical solution is validated against the well-known McNamee Gibson's problem (McNamee & Gibson, 1960a, 1960b). The problem setup and the boundary conditions are shown in **Figure 3.4** (a). The surface tractions T_1 and T_2 are imposed on the top boundary at $t > 0$, causing the pressure to build up instantaneously within the domain. Fixed normal displacement boundaries are set for the left, right, and bottom boundaries. No-flow boundary conditions are applied everywhere except for the top edge, where a piecewise traction is imposed. The entire domain is fully saturated with a single-phase, slightly compressible,

fluid. The parameters used in this case are recorded in **Table 3.1**. The normalized pressure vs. dimensionless time of the observation point located at (2.5, 2) is provided in **Figure 3.4** (b). The dimensionless time is ct/l_2^2, where c is the consolidation coefficient and is written as

$$c = kM\left(K_{dr} + \frac{4}{3}G\right)\Big/\left(\mu K_{dr} + \mu b^2 M + \frac{4}{3}\mu G\right). \quad 3.30$$

M is the Biot modulus, G is the shear modulus, and l_2 is the domain's vertical length. In **Figure 3.4** (b), the solution obtained using the proposed approach is with the analytical solution and numerical solution of Liu, Liu, et al. (2020), and a good match between these solutions.

Parameters	Value
Model dimension, $l_1 \times l_2$	110 m ×110 m
Porosity, ϕ	0.25
Permeability, k	4.935×10^{-14} m^2
Young's modulus, E	450 MPa
Poisson's ratio, v	0
Biot's coefficient, b	1
Fluid compressibility, c_f	4×10^{-10} Pa^{-1}
Fluid viscosity, μ	10^{-3} Pa·s
Traction1 T_1, range a_1	20 MPa, 4 m
Traction2 T_2, range a_2	10 MPa, 106 m
Initial pressure, p_i	10 MPa

Table 3.1. Parameters used in McNamee Gibson's problem.

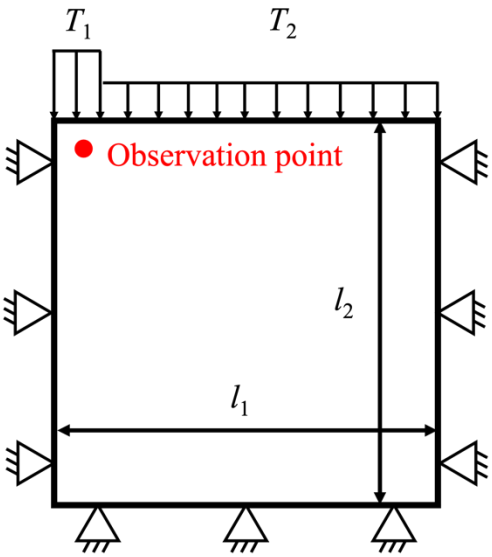

(a)

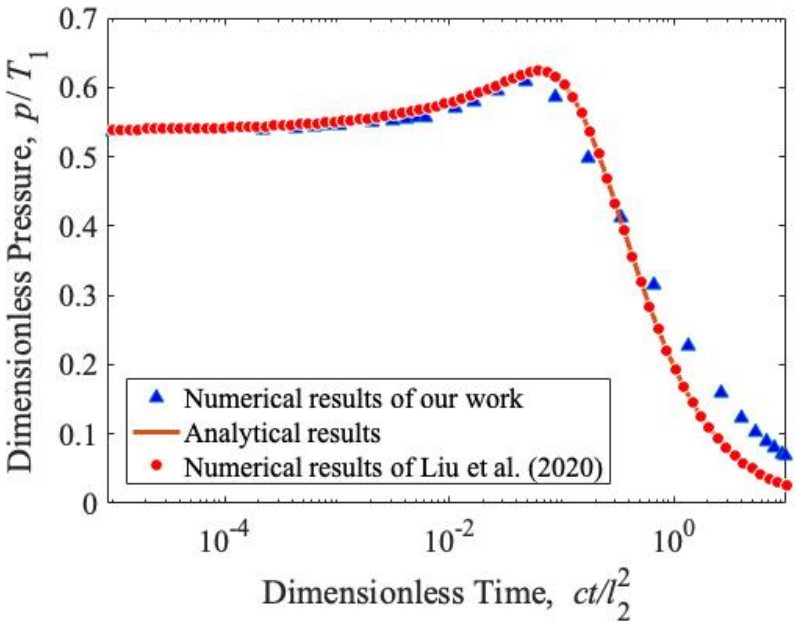

(b)

Figure 3.4. (a) The geometry and boundary conditions of the McNamee Gibson's problem and (b) comparison of the analytical and the numerical solutions.

3.4.2 Fracture Deformation Verification

To verify the accuracy and assess the performance of the fracture deformation model, a single-phase validation case is compared to the solutions obtained by Gu et al. (2014) and Moradi

et al. (2017). The 2D simulation domain with four fractures and two horizontal wells is shown in **Figure 3.5**. Fracture (a) is the longest connecting the two wellbores. Fracture (b) and Fracture (c) are 100 m in length and are connected to the injector and the producer, respectively. Fracture (d), with a length of 100 m, is located midway between two wells. Fixed displacement boundaries are set for the left and bottom edges, while the other two boundaries are subjected to the constant stress of 20 MPa. Parameters for this model setup are summarized in **Table 3.2**, and they are extracted from Moradi et al. (2017). The fracture permeability is computed according to the cubic law based on the initial fracture aperture. The fractures are aligned along the same direction of horizontal traction; hence, any shear displacement of fracture can be ignored.

Figure 3.6 compares the numerical solutions of fracture aperture between the present model with the previous works after 360 days of production. The comparison verifies the model's accuracy presented in this study; there is a particularly close match between the present work and Moradi et al. (2017). The small discrepancy between the results in this study and others can be attributed to neglecting shear dilation in the present model.

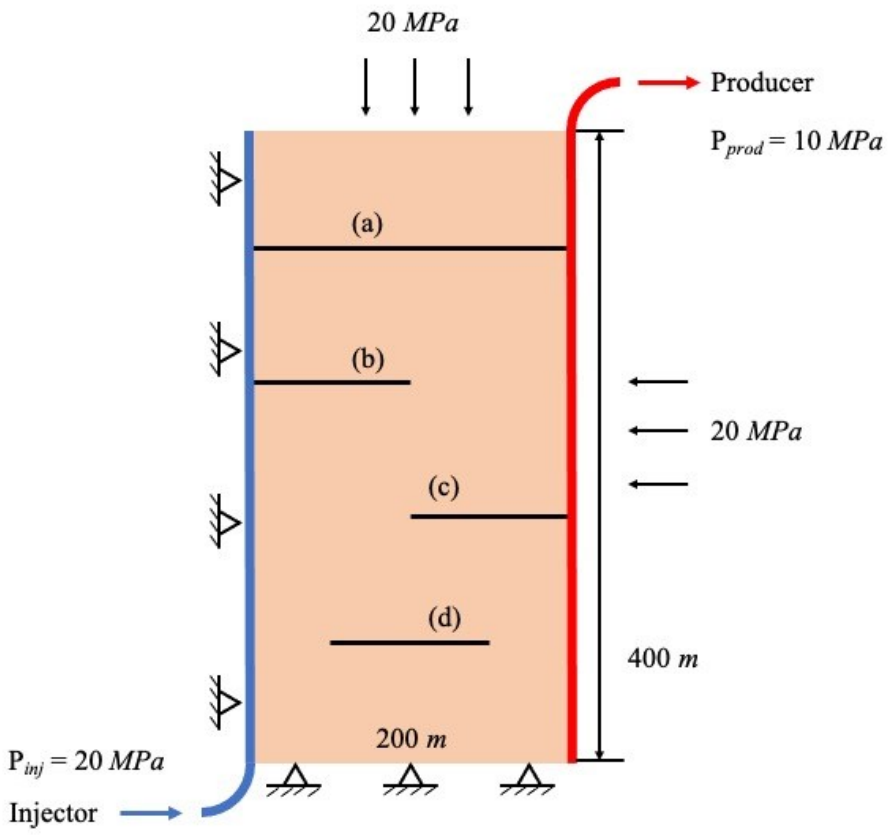

Figure 3.5. Fracture deformation validation model setup.

Parameters	Value
Model dimension, $L \times L$	200 m × 400 m
Matrix porosity, ϕ_M	0.15
Matrix permeability, k_M	5×10^{-14} m^2
Fracture porosity, ϕ_f	0.8
Fracture permeability, k_f	5.2×10^{9} m^2
Initial normal stiffness, K_{ni}	1.2×10^{11} Pa/m
No-load fracture aperture, a	2.5×10^{-4} m
Maximum fracture aperture closure, D_{nmax}	2.4×10^{-4} m
Fluid viscosity, μ	1.8×10^{-4} Pa s
Fluid compressibility, c_f	5.39×10^{-9} Pa^{-1}
Young's modulus, E	5.8 GPa
Poisson's ratio, v	0.3

Biot's coefficient, b	0.83
Initial pressure, P_i	10 MPa
Horizontal stress, S_{Hmax}/S_{Hmin}	20 MPa
Bottom hole pressure of injector, P_{inj}	20 MPa
Bottom hole pressure of producer, P_{prod}	10 MPa

Table 3.2. Parameters used in fracture deformation verification case.

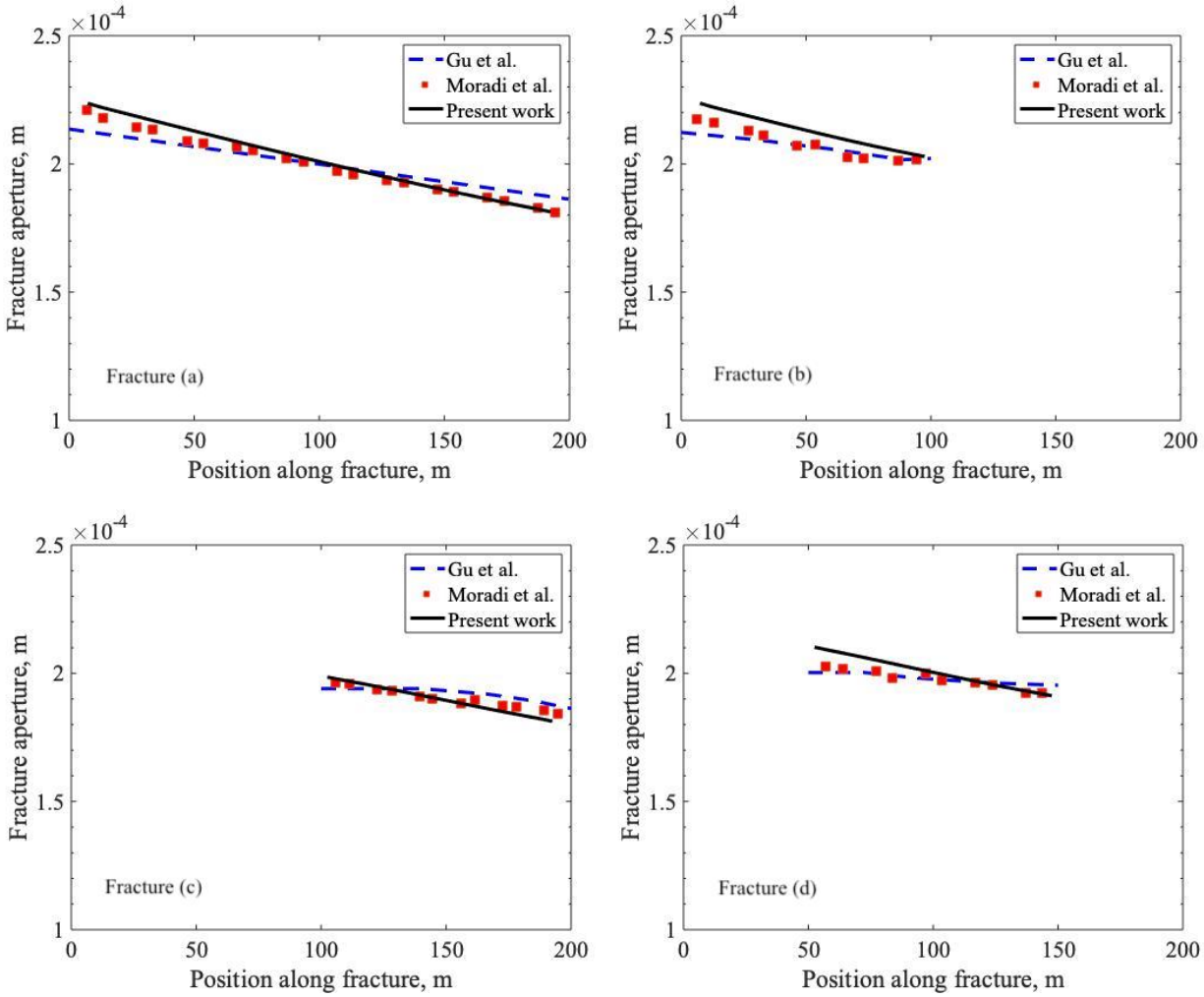

Figure 3.6. Comparison of numerical solutions of fracture aperture between the present work and previous studies.

CHAPTER 4 : ANALYSIS OF FRACTURE INTERFERENCE AND PRESSURE DISTRIBUTION

4.1 Overview

Several case studies demonstrate the utility of the proposed coupling strategy for analyzing production performance and stress evolution in hydraulically fracturing formations. This model considers the effects of poroelasticity and stress or strain variation in the fractured domains, and factors influencing the behaviour of fracture interference are examined. This simulation approach can more accurately capture the dynamic behaviour of stress evolution and fracture interference in hydraulically fractured wells. The results illustrate the significance of incorporating geomechanical effects in the flow simulation process. Insights pertinent to the operational strategies are also highlighted based on the simulation results.

4.2 Analysis of Hydraulic Fracturing Pressure Distribution

4.2.1 Single Planar Hydraulic Fracture Model Setup

To illustrate the effects of geomechanics on the pressure distribution, two models with a single hydraulic fracture in the middle of the domain are simulated (Liu, Liu, et al., 2020); one of which solves only the flow problem (i.e., the uncoupled model), and the other solves the coupled fluid flow and geomechanical simulation. A production well is located in the middle of the fracture. The geomechanical boundary conditions of the coupled problem are shown in **Figure 4.1** (a), where the no-flow boundary is applied on all sides, as shown in **Figure 4.1** (b). Other parameters are recorded in **Table 4.1**.

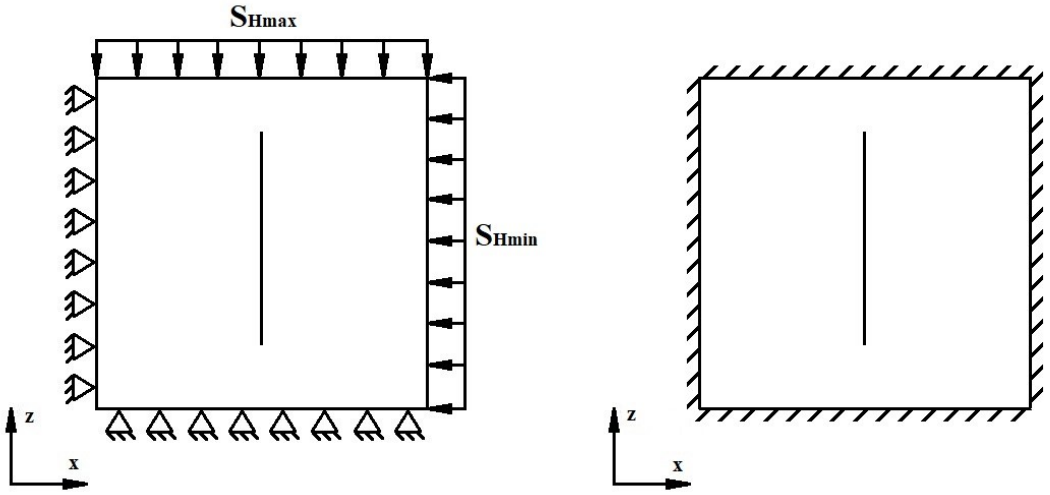

(a) (b)

Figure 4.1. The geometry and boundary conditions for the (a) geomechanical and (b) flow problems corresponding to the single planar hydraulic fracture case.

Parameters	Value
Model dimension, $L \times L$	100 m × 100 m
Matrix porosity, ϕ_M	0.09
Matrix permeability, k_M	5×10^{-19} m^3
Fracture half-length, $L_f/2$	30 m
Fracture porosity, ϕ_f	0.8
Fracture permeability, k_f	1×10^{-12} m^3
Fracture aperture, a	1×10^{-3} m
Young's modulus, E	29 GPa
Poisson's ratio, v	0.2
Biot's coefficient, b	1
Initial pressure, P_i	4.69×10^7 Pa
Horizontal stress, S_{Hmax}/S_{Hmin}	5×10^7 Pa
Bottom hole pressure, P_{wf}	2 x 10^7 Pa
Matrix initial water saturation, S_{wM}	0.2
Initial normal stiffness, K_{ni}	5×10^9 Pa/m
Maximum fracture aperture closure, D_{nmax}	9.8×10^{-4} m

Table 4.1. Parameters used in the single planar hydraulic fracture problem.

4.2.2 Comparison of Pressure Distribution, Production Rate, and Cumulative Production

Pressure distributions of the uncoupled and coupled models are compared in **Figure 4.2**. A pressure-depleted area around the hydraulic fracture can be easily detected, and the depleted area for the uncoupled model is noticeably more extensive than that of the coupled model. Their production profiles are compared in **Figure 4.3**. The coupled model yields a slightly lower oil production, particularly during the initial 100 days. This decrease in production correlates with the fracture closure and reduction in pressure depletion. The difference in cumulative production between the coupled model and the uncoupled model is 0.042 m^3 (approximately 10%) after a year of production.

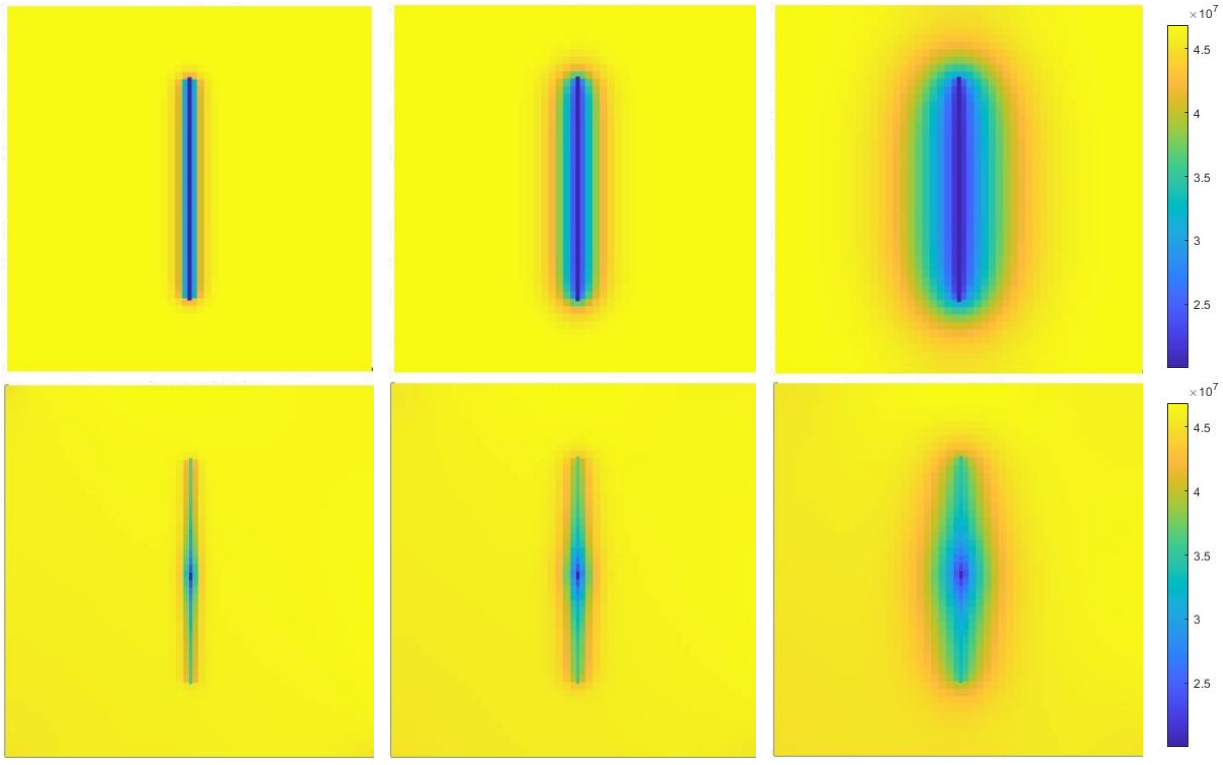

(a) 2 days (b) 15 days (c) 90 days

Figure 4.2. Comparison of pressure distribution after (a) 2 days (b) 15 days and (c) 90 days of production: uncoupled model (first row) and coupled model (second row).

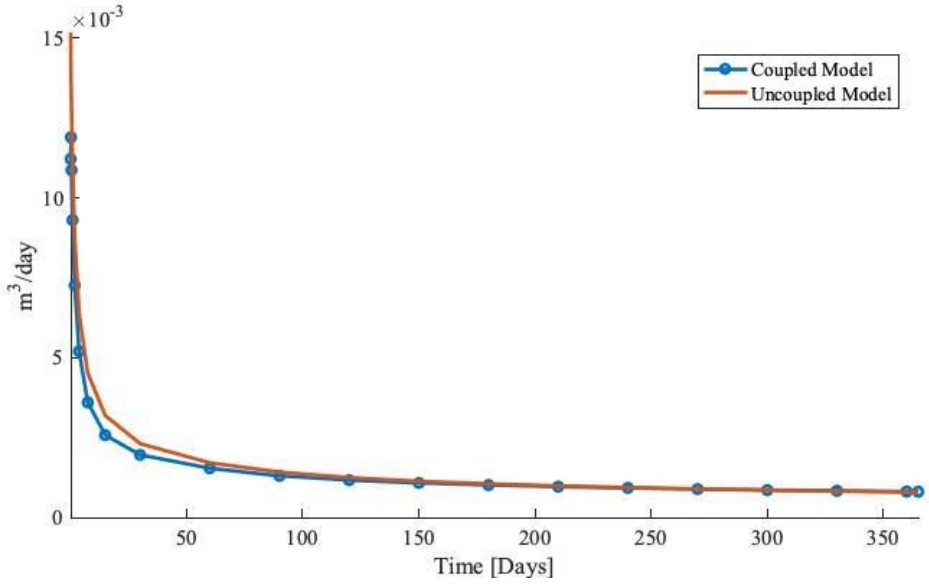

(a) Production rate of the oil phase

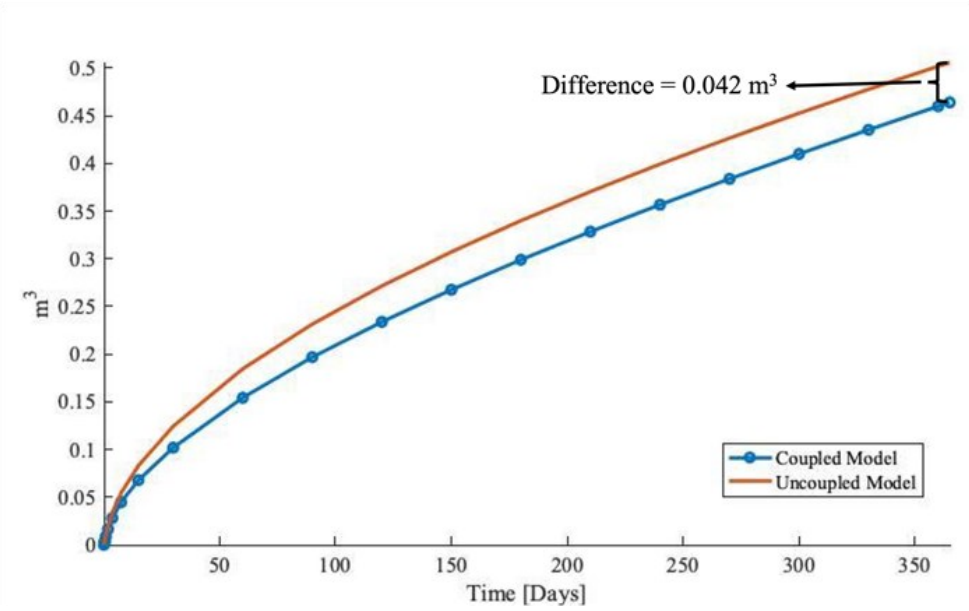

(b) Cumulative production of the oil phase

Figure 4.3. Comparison of (a) production rate and (b) cumulative production between the uncoupled and coupled models.

4.3 Sensitivity Analysis of Geomechanical Properties

In recent years, mathematical models and their application in simulating stress state changes and pressure depletion distribution due to fracture interference have been widely studied

(Manchanda et al., 2018; Settari et al., 2002; Wu et al., 2018). Many factors often influence well-to-well interference, including fracture geometry, well spacing, and cluster spacing. Guo et al. (2019) demonstrated the importance of modelling non-uniform hydraulic fracture geometry and well spacing on fracture hits for an Eagle Ford Shale well. Kurtoglu and Salman (2015) indicated that well spacing might control how fracture interference would affect recovery efficiency. Lin et al. (2018) analyzed the optimal cluster spacing in the Fuling shale gas field. They concluded that a balance between managing pressure interference and increasing stimulated reservoir volume should be considered. With small cluster spacing, the pressure depletion behaviour surrounding individual hydraulic fractures may overlap significantly; on the other hand, the stimulated reservoir volume could be too small if the cluster spacing is too wide. Li and Zhang (2018) further illustrated that fracture interference would disturb fracture growth if the cluster spacing was less than a critical stress value. Roussel et al. (2013) studied the effects of stress reversal on fracture propagation in infill wells. Their results illustrated that it is essential to quantify the extent of stress interference in parent-child and multi-stage completions to maximize stimulated reservoir volume. Bhardwaj et al. (2016) analyzed the thermal effects corresponding to multi-well and multi-fracture production. They concluded that stress re-orientation is strongly influenced by mechanical displacement, poroelasticity, and thermoelasticity.

Fracture interference has a significant impact on the efficiency of hydrocarbon recovery. Stress field evolution due to pressure depletion results in stress shadowing and inter-well interference, which, in turn, would affect the propagation of nearby fractures from later stages or adjacent wells. Therefore, a detailed sensitivity analysis involving hydraulic fracture geometry, well spacing, cluster spacing, and differential stress is performed to assess the effect of spacing between wells or fracturing clusters on pressure depletion and stress evolution.

4.3.1 Model Setup

For the base case, most of the model parameters are similar to the previous example (e.g., **Figure 4.1**); however, a different set of geometry and geomechanical boundary conditions are adopted: For the initial state, S_{hmin} is 55 MPa, and S_{Hmax} is 58 Mpa, as shown in **Figure 4.4** (a). In addition, the initial normal stiffness K_{ni} has also been changed to 200 Gpa/m. Three equally spaced hydraulic fractures with uniform lengths are placed in this multi-stage hydraulic fracturing case. The pressure distribution and effective maximum principal stress (S'_{Hmax}) orientation (represented by the white dash line) after 1 year are shown in **Figure 4.4** (b). S'_{Hmax} orientation is affected significantly by the pressure drop in the vicinity of hydraulic fractures. The hydraulic fracture is oriented along the direction of the S'_{Hmax}. There is less effect on S'_{Hmax} orientation as the distance away from the hydraulic fracture increases. **Figure 4.4** (c) and (d) show the magnitude of S'_{Hmax} and effective minimum principal stress (S'_{hmin}), respectively. The stress evolution for both maximum and minimum stress extends over a larger area than the pressure depletion zone, as shown in **Figure 4.4** (b). Besides, effective stress would decrease from the fracture to the domain boundary, while pressure would decrease towards the perforations. This is due to the imposed total stress being fixed.

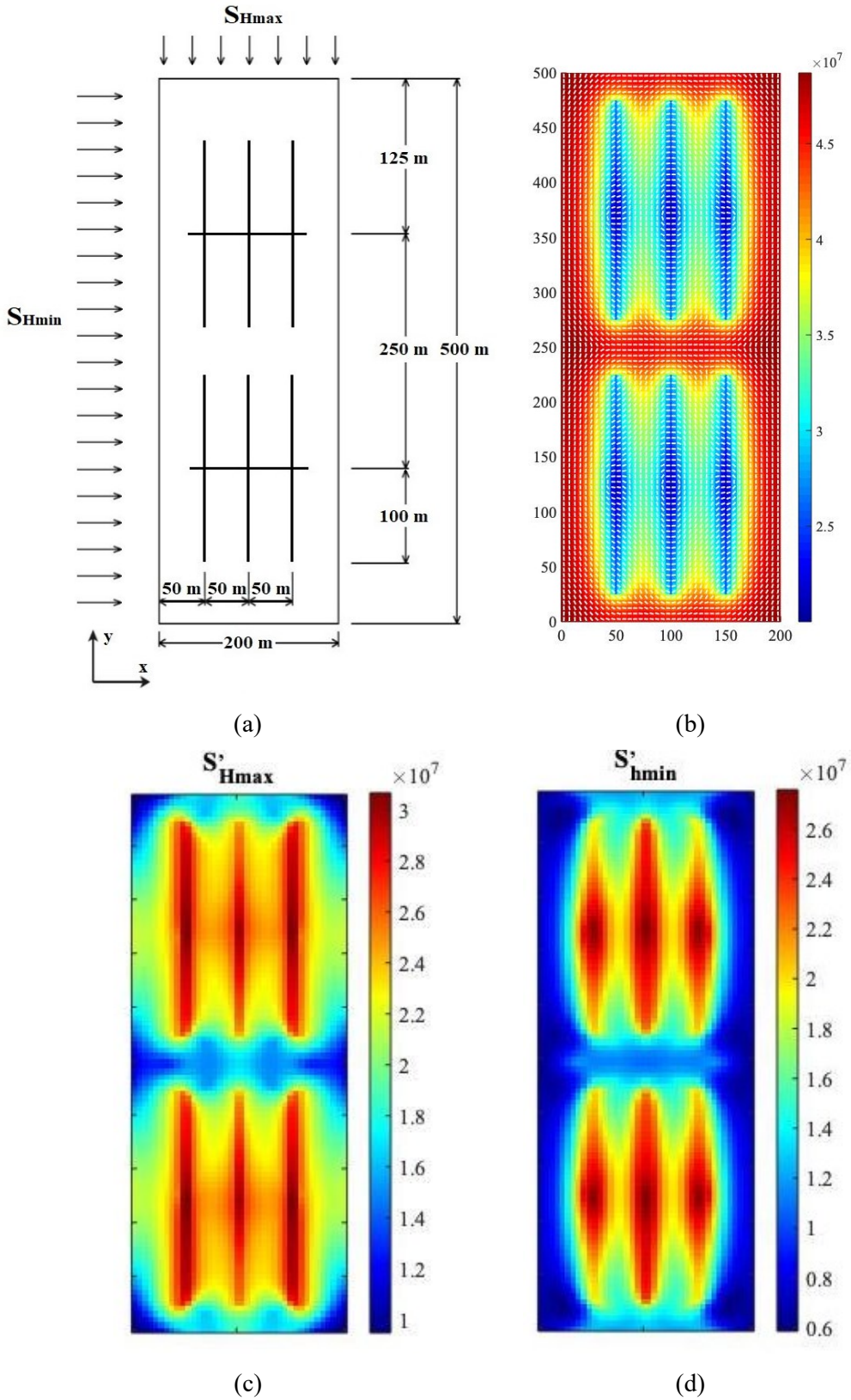

Figure 4.4. (a) Geometry of the multi-stage hydraulic fracturing case, (b) pressure distribution and S'_{Hmax} orientation, (c) S'_{Hmax}, and (d) S'_{hmin} magnitude after 1 year.

4.3.2 Effects of Hydraulic Fracture Geometry

Two non-uniform fracture geometries are analyzed here. For fracture geometry 1, the half-length of the two outer fractures is much longer than the middle one (100 m vs. 30 m). For fracture geometry 2, the situation is reversed. This case is to assess potential stress-shadowing effects. **Figure 4.5** shows the corresponding pressure distribution, S'_{Hmax} orientation, and magnitudes of S'_{Hmax} and S'_{hmin} for geometry 1 and geometry 2 after 1 year of production. **Figure 4.6** illustrates the difference (in degrees) between the initial orientation of S'_{Hmax} and the current orientation, pressure change, and the evolution of effective principal stress for the two cases.

As expected, the fracture geometry significantly impacts stress evolution and pressure distribution. The stress and pressure distribution in **Figure 4.5** resemble the trends shown in the Base Case. **Figure 4.6** (a) reveals that S'_{Hmax} is reoriented and rotated 90 degrees around the hydraulic fracture tips, and this change is minimal at the locations furthest away from the fractures. Comparing **Figure 4.6** (b) and (c), the trends for pressure change are opposite to those of S'_{Hmax} change. However, comparing **Figure 4.6** (b) and (d), the trends for pressure change are opposite to those of S'_{hmin} only in areas far away from the hydraulic fractures. In contrast, the trends are similar in the vicinity of the hydraulic fractures. In **Figure 4.6** (d), S'_{hmin} magnitude corresponding to the Base Case is the highest, and the pressure in the two wells is also the lowest in the Base Case. In **Figure 4.6** (d), there are three local minima for geometry 1, indicating that S'_{hmin} at a certain location is affected not only by its proximity to nearby hydraulic fractures but also by the proximity to all other fractures in the domain. **Figure 4.6** also supports the observation that the drainage area for geometry 2 is the smallest; thus, from the perspective of production enhancement, configurations similar to geometry 2 should be avoided.

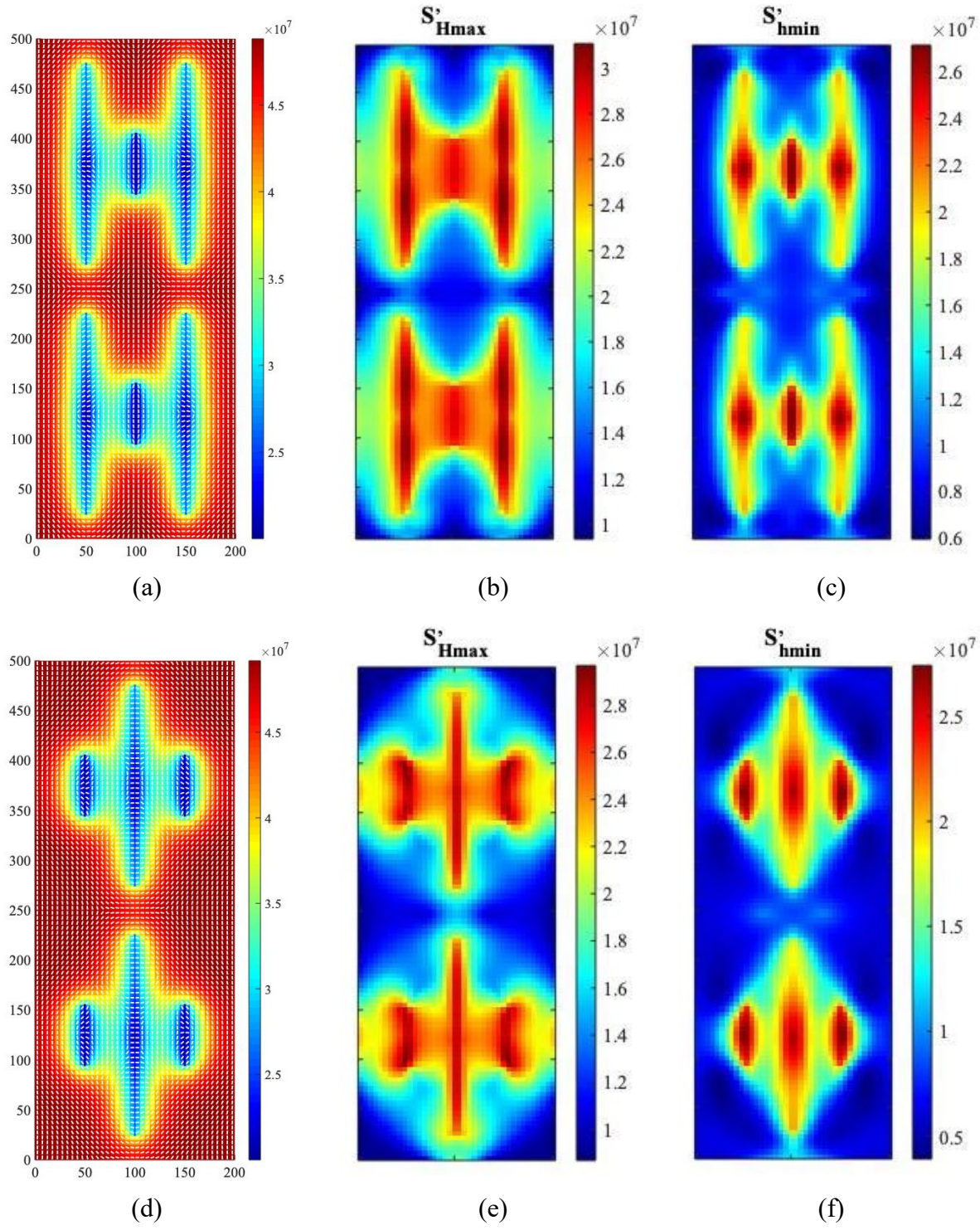

Figure 4.5. (a), (d) Pressure distribution and S'_{Hmax} orientation; (b), (e) S'_{Hmax} magnitude; and (c), (f) S'_{hmin} magnitude for geometry 1 and geometry 2, respectively, after 1 year of production.

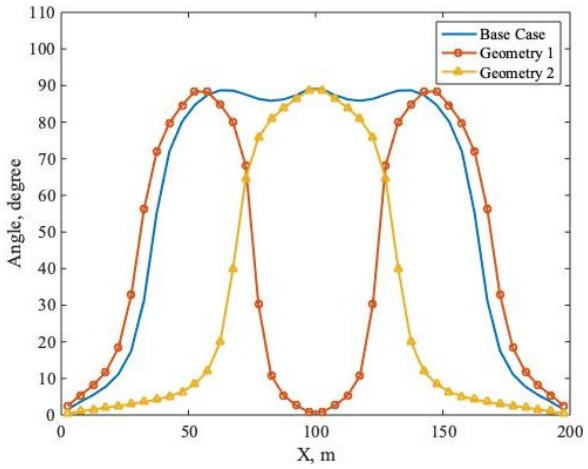

(a) $\boldsymbol{S'_{Hmax}}$ orientation change

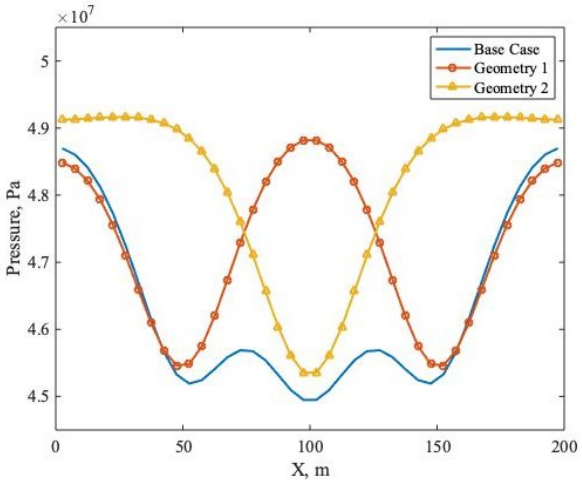

(b) Pressure changes with location

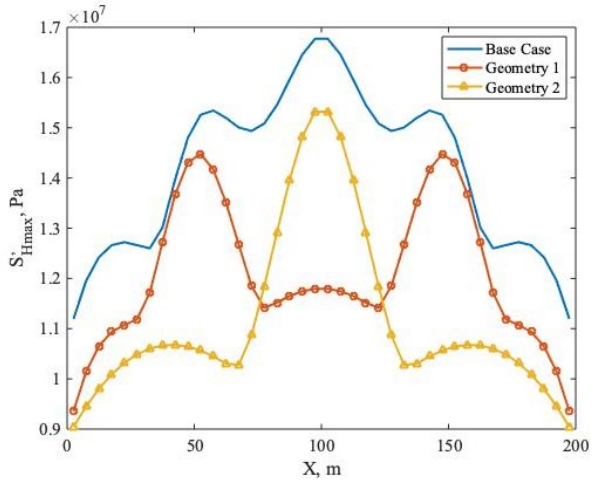

(c) $\boldsymbol{S'_{Hmax}}$ change with location

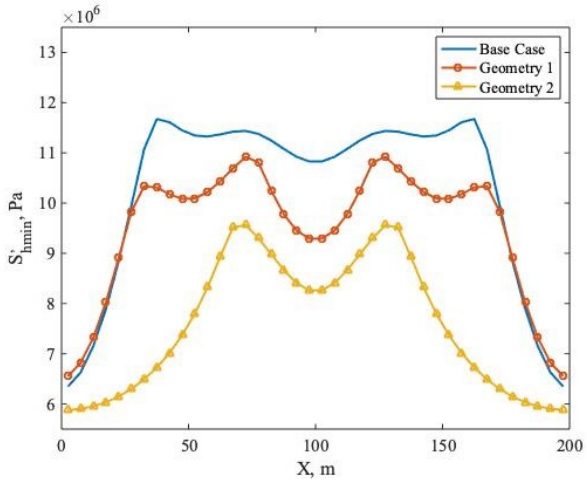

(d) $\boldsymbol{S'_{hmin}}$ change with location

Figure 4.6. (a) S'_{Hmax} orientation change, (b) pressure changes, (c) S'_{Hmax} magnitude change, and (d) S'_{hmin} magnitude change along the x-direction at y = 250 m after 1 year.

4.3.3 Effects of Well Spacing

Two additional models with different well spacing (220 m and 280 m, respectively) are simulated. **Figure 4.7** shows the corresponding pressure distributions and effective principal stress evolutions after 1 year of production. **Figure 4.8** compares the difference (in degrees) between the

initial orientation of S'_{Hmax} and the current orientation, pressure change, and the evolution of effective principal stress for the two cases.

Figure 4.8 (a) shows that the orientation of S'_{Hmax} is not overly sensitive to well spacing; for example, the same change in S'_{Hmax} orientation around the hydraulic fracture area is observed for all three cases. Not surprisingly, the smaller the well spacing, the higher the effective principal stress at y = 250 m because of more excessive pressure depletion, as shown in **Figure 4.8** (b), (c), and (d). The results also resemble those presented in the previous subsections, where the trends for pressure change are opposite to those of S'_{Hmax} change.

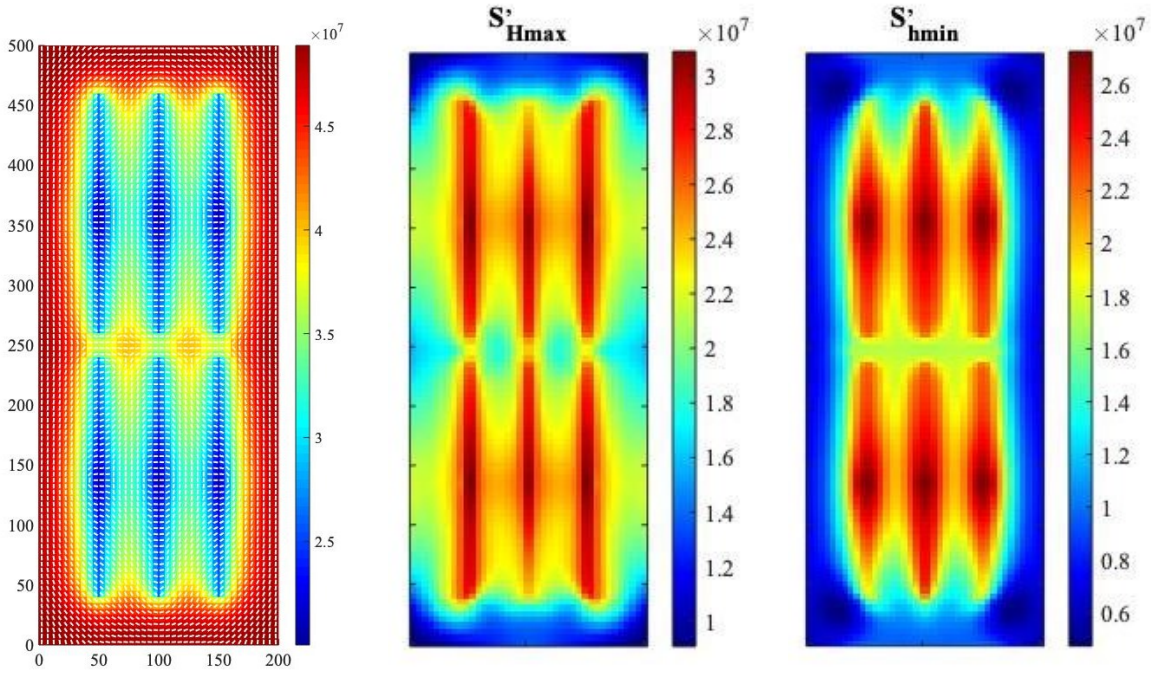

(a) (b) (c)

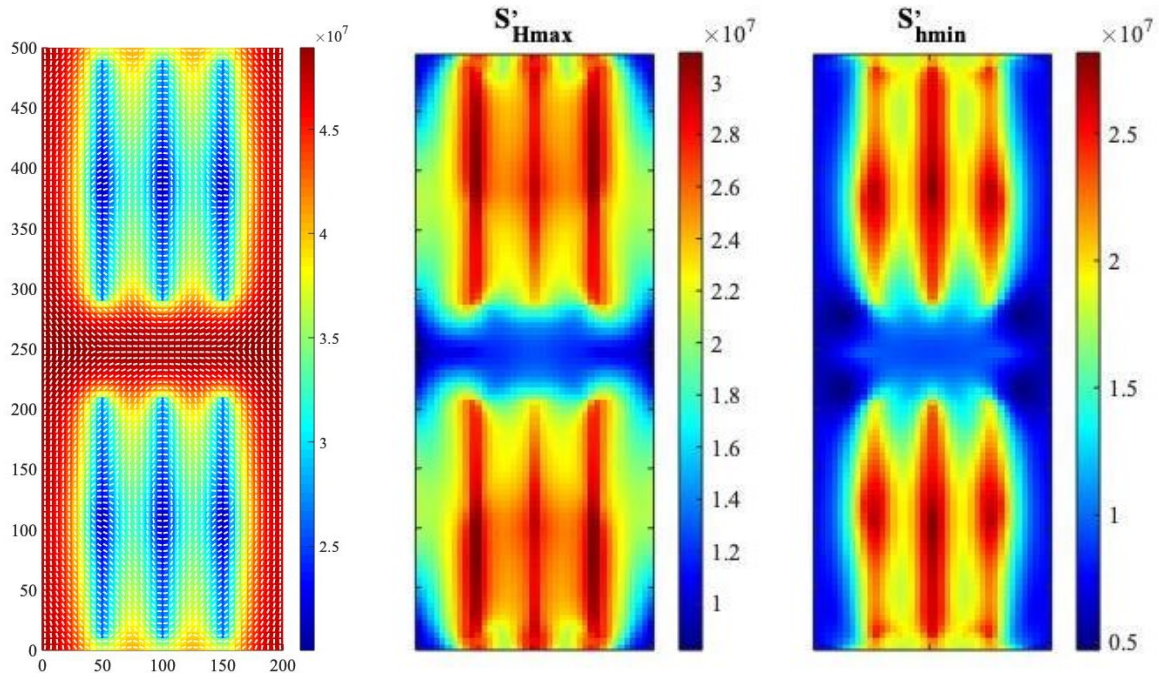

(d) (e) (f)

Figure 4.7. (a), (d) Pressure distribution and S'_{Hmax}; (b), (e) S'_{Hmax} magnitude; and (c), (f) S'_{hmin} magnitude for well spacing of 220 m and well spacing of 280 m, respectively, after 1 year of production.

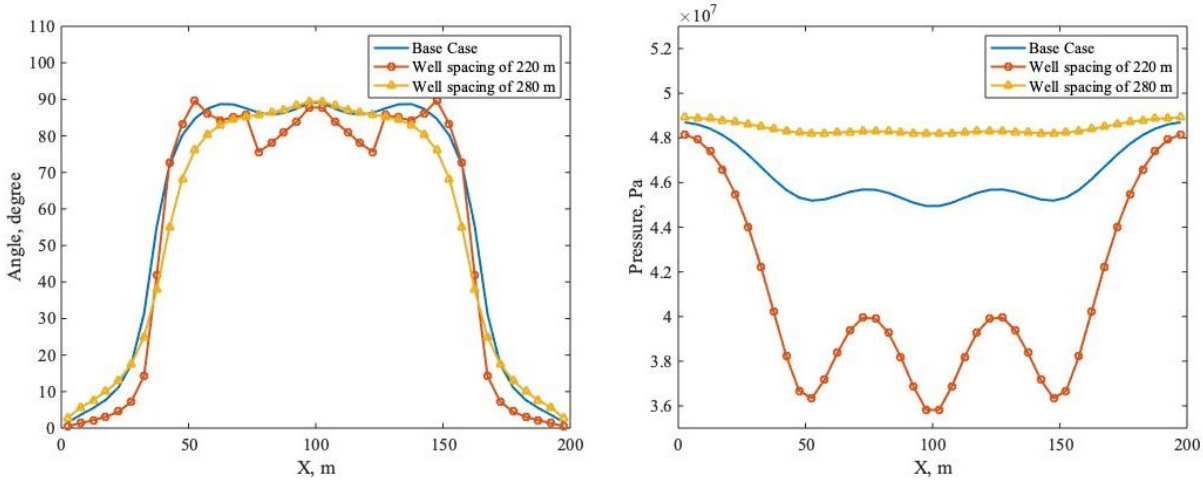

(a) S'_{Hmax} orientation change (b) Pressure changes with location

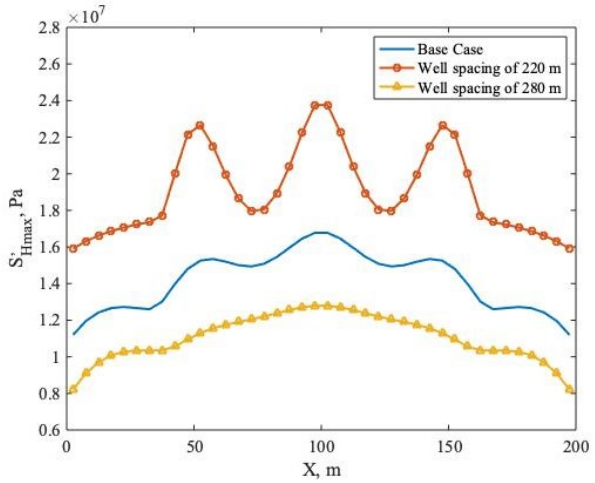

(c) S'_{Hmax} change with location

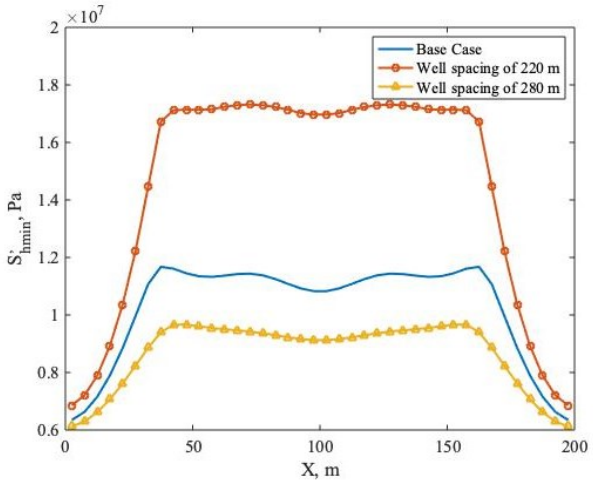

(d) S'_{hmin} change with location

Figure 4.8. (a) S'_{Hmax} orientation change, (b) pressure change, (c) S'_{Hmax} change, and (d) S'_{hmin} change along the x-direction at y = 250 m after 1 year.

4.3.4 Effects of Cluster Spacing

Two cases with different cluster spacing (25 m vs. 75 m) are simulated. The locations of the middle fractures are the same as the multi-stage hydraulic fracturing base case. **Figure 4.9** shows the pressure depletion, S'_{Hmax} orientation, and effective principal stress evolutions after 1 year of production. **Figure 4.10** shows the stress orientation change, pressure, and stress field variation after 1 year.

Figure 4.9 and **Figure 4.10** (b) show that when the fractures are placed too close to one another, there is a substantial overlapping in the pressure and effective stress fields. However, if the fractures are placed too far apart, there will be an area between fractures that cannot be drained. **Figure 4.10** (a) resemble those presented in the previous subsection: more significant changes in S'_{Hmax} orientation in regions closer to the hydraulic fractures. **Figure 4.10** (d) shows that an increase in cluster spacing also leads to a rise in S'_{Hmax}.

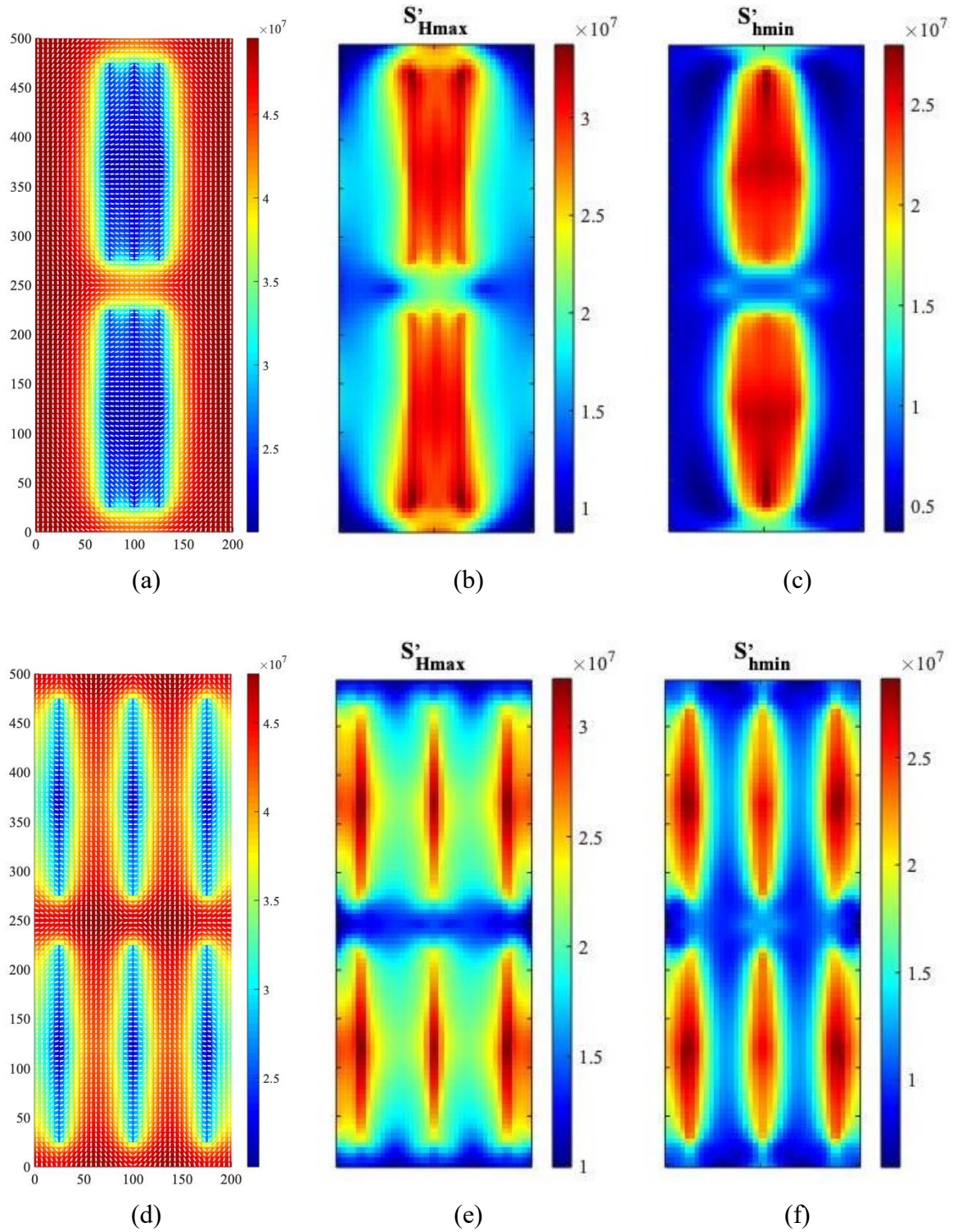

Figure 4.9. (a), (d) Pressure distribution and S'_{Hmax}; (b), (e) S'_{Hmax} magnitude; and (c), (f) S'_{hmin} magnitude for cluster spacing of 25 m and cluster spacing of 75 m respectively after 1 year of production.

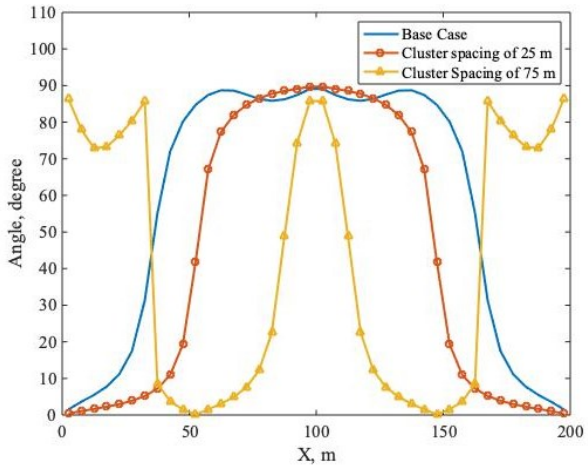

(a) S'_{Hmax} orientation change

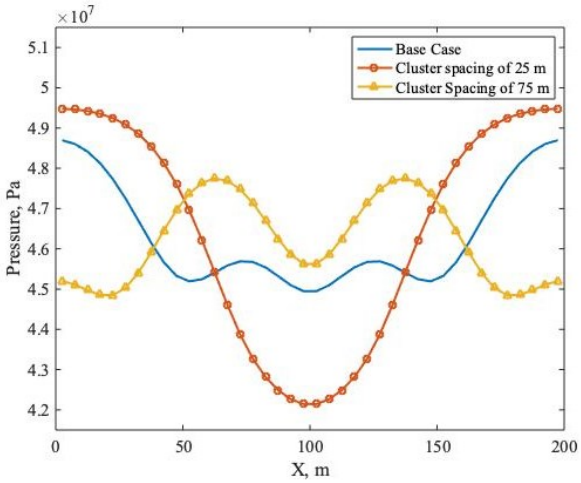

(b) Pressure changes with location

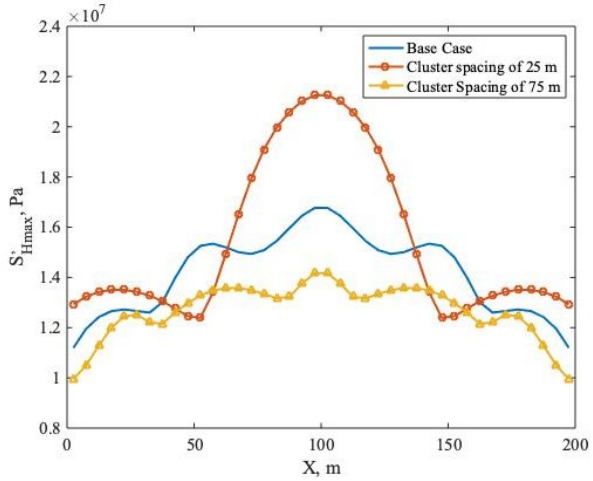

(c) S'_{Hmax} change with location

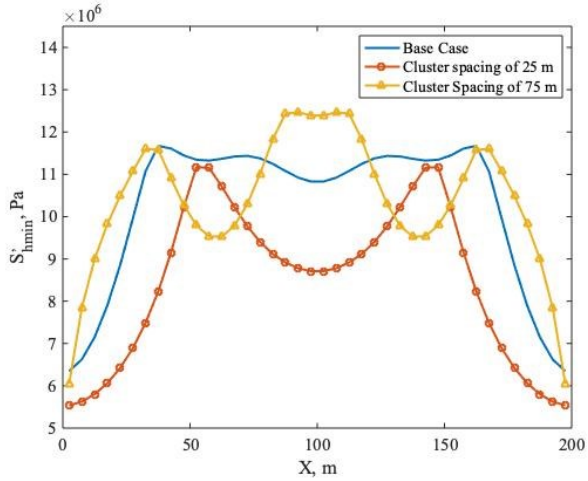

(d) S'_{hmin} change with location

Figure 4.10. (a) S'_{Hmax} orientation change, (b) pressure changes, (c) S'_{Hmax} change, and (d) S'_{hmin} change along the x-direction at y = 250 m after 1 year.

4.3.5 Effects of Differential Stress (DS)

Two cases with different differential stress (DS = 5 MPa vs. 10 MPa) are simulated. The minimum stresses on both cases' left and right boundaries are not changed and remain as 55 MPa. However, the maximum stresses are changed to 60 MPa and 65 MPa, respectively. **Figure 4.11** shows the pressure depletion, S'_{Hmax} orientation, and effective principal stress evolutions after 1

year of production. **Figure 4.12** shows the stress orientation change, pressure, and stress field variation after 1 year.

There is a significant impact on stress evolution and pressure depletion. In **Figure 4.12** (a), if the DS is large enough, the stress re-orientation phenomenon is much subdued in most regions between two adjacent wells. However, some degree of stress re-orientation still exists in the middle of the domain due to nearby hydraulic fractures. **Figure 4.12** (b) reveals that an increase in DS leads to higher pressure. The pressure drop in the vicinity of hydraulic fractures is comparable in all three cases. In **Figure 4.12** (c), S'_{Hmax} increases with increasing differential stress near the domain boundaries, while for the areas in the vicinity of fractures, S'_{Hmax} remains the same. The opposite trend is observed in **Figure 4.12** (d), where S'_{hmin} will not change with increasing DS near the boundaries and increases with DS in the vicinity of the hydraulic fractures.

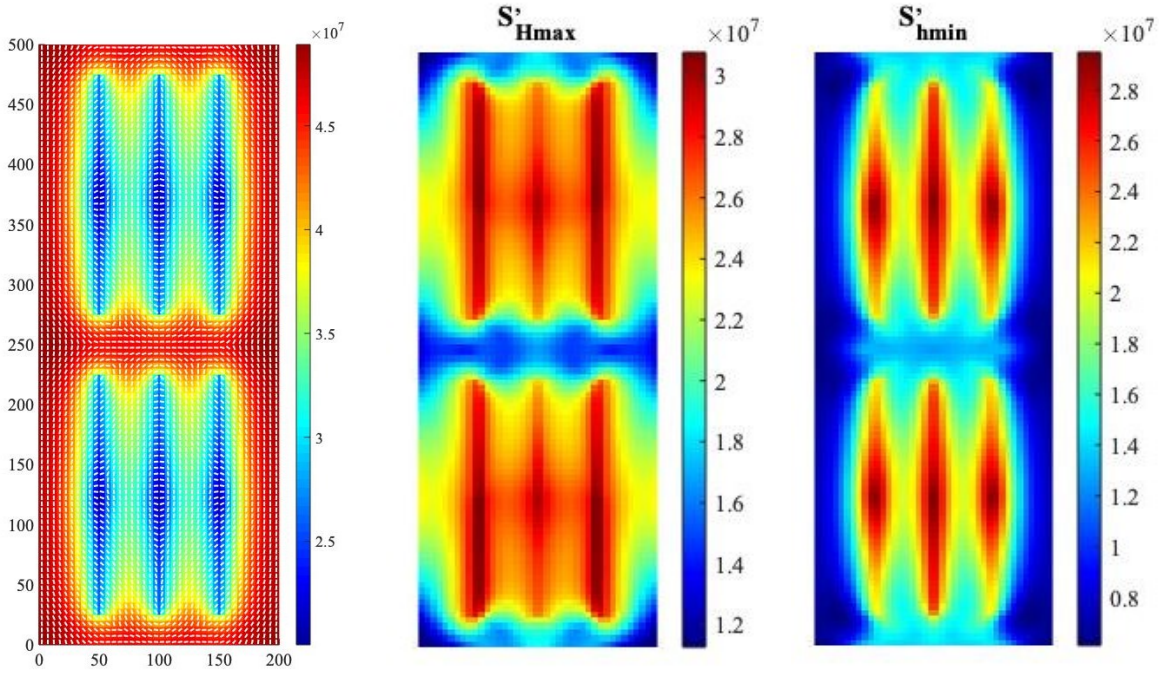

(a) (b) (c)

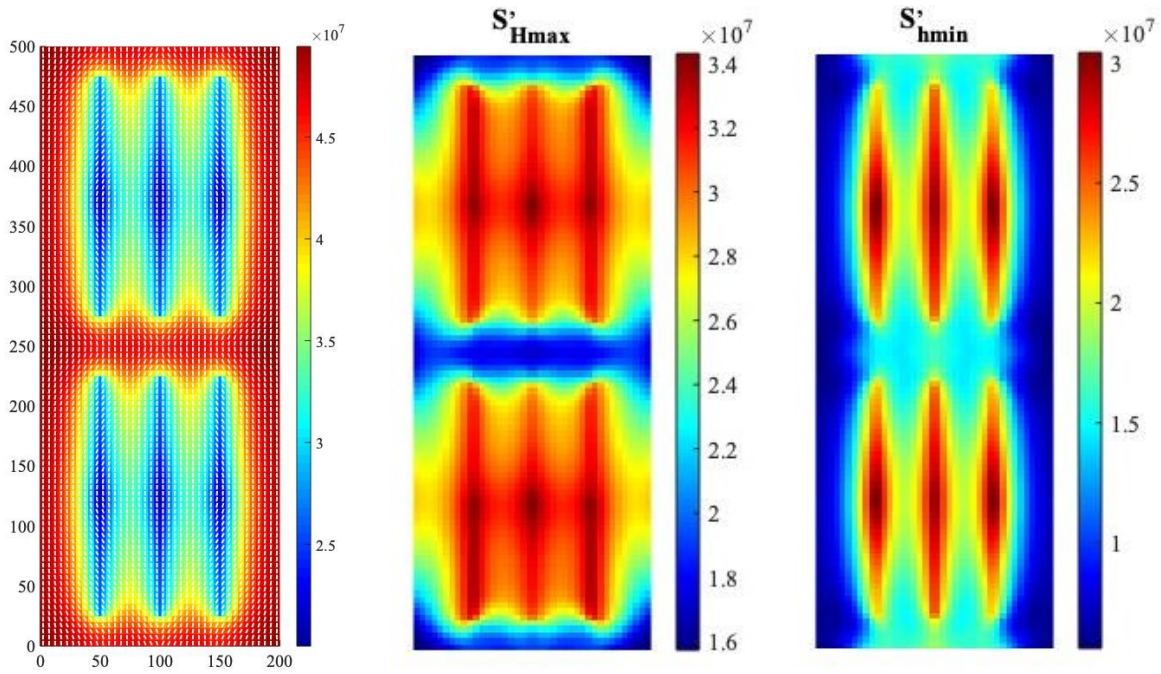

(d) (e) (f)

Figure 4.11. (a), (d) Pressure distribution and S'_{Hmax}, (b), (e) S'_{Hmax} magnitude, and (c), (f) S'_{hmin} magnitude for DS of 5 MPa and DS of 0 MPa respectively after 1 year of production.

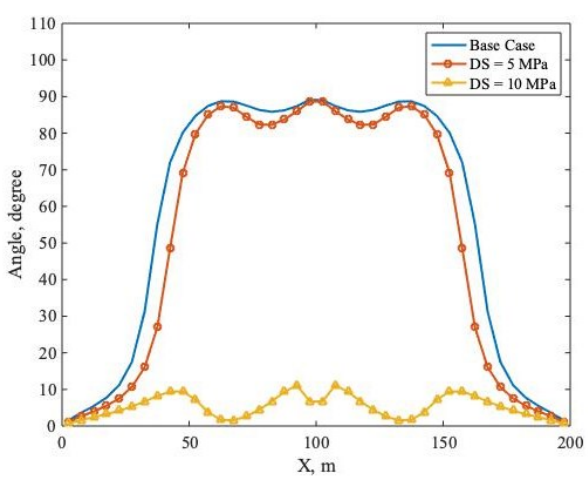

(a) $\boldsymbol{S'_{Hmax}}$ orientation change

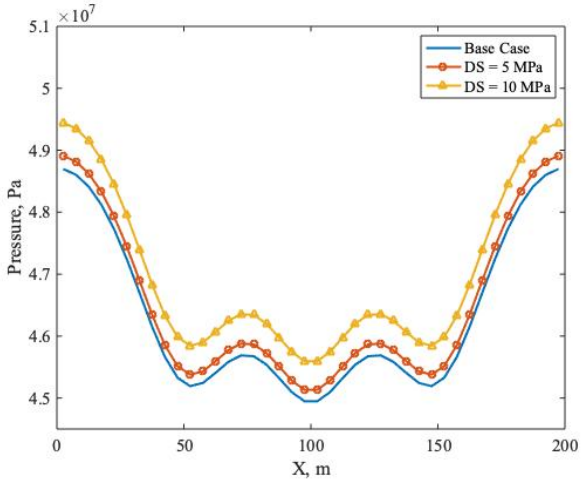

(b) Pressure changes with location

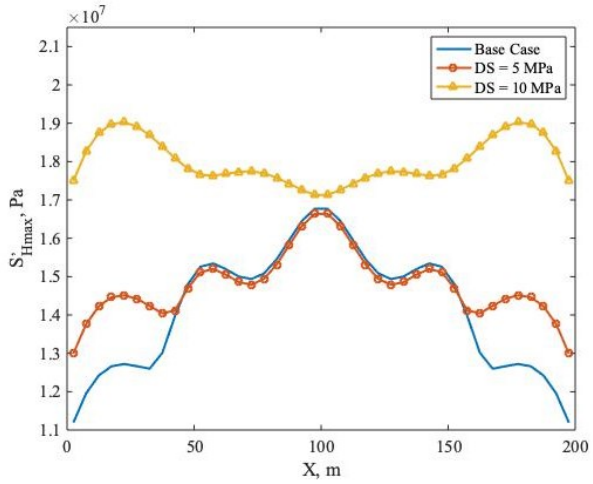

(c) $\boldsymbol{S'_{Hmax}}$ change with location

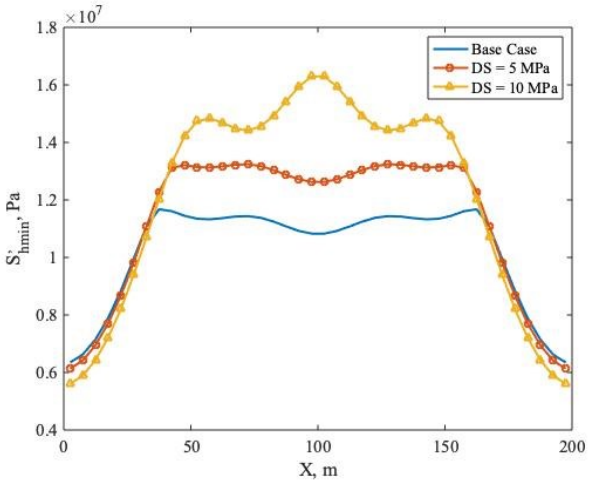

(d) $\boldsymbol{S'_{hmin}}$ change with location

Figure 4.12. (a) S'_{Hmax} orientation change, (b) pressure changes, (c) S'_{Hmax} change, and (d) S'_{hmin} change along the x-direction at y = 250 m after 1 year.

4.4 Fluid Loss Mechanism Analysis

Many recent research studies have reported the water-loss mechanisms and their effects on production (Bertoncello et al., 2014; Cheng, 2012; Liu, Liu, et al., 2020; Wang & Leung, 2015). The main limitation of these studies is that relatively coarse grids were used: detailed fracture geometries and arbitrarily distributed natural fractures were not explicitly modeled. Wang and Leung (2015) investigated water retention and trapping in the matrix and natural fracture systems, but geomechanical calculations were neglected and only orthogonal natural fractures were modeled. Liu, Liu, et al. (2020) developed a coupled flow and geomechanical simulation model to predict fluid distribution and recovery. The drawback was that complex branching natural fracture networks were not included, and, hence, fluid distribution in the fracture cells was not fully analyzed. Therefore, the coupled flow-geomechanical simulation model developed in this study is used here to analyze fracturing fluid loss mechanisms.

4.4.1 Model Setup

Two cases are examined in this section. One has a simple fracture network with four natural fractures intersecting with a planar hydraulic fracture, while the other has a branching natural fracture network. The geomechanical properties are listed in **Table 4.2**, and a schematic of the fracture network and boundary conditions are shown in **Figure 4.13**. No flow boundaries are applied on all the edges. Zero displacement boundaries are applied on the left and bottom edges of the domain, and the same horizontal stress is applied on the top and right boundaries. The relative permeability and capillary pressure for the matrix, natural fracture and hydraulic fracture systems are assigned according to the functions presented in Wang and Leung (2015).

Parameters	Value
Model dimension, $L \times L$	50 m × 50 m
Matrix porosity, ϕ_M	0.06
Matrix permeability, k_M	2×10^{-19} m^3
Hydraulic fracture half-length, $L_{hf}/2$	10 m
Hydraulic fracture porosity, ϕ_{hf}	0.9
Hydraulic fracture permeability, k_{hf}	1×10^{-12} m^3
Natural fracture porosity, ϕ_{nf}	0.5
Natural fracture permeability, k_{nf}	1×10^{-14} m^3
Fracture aperture, a	1×10^{-3} m
Young's modulus, E	29 GPa
Poisson's ratio, v	0.2
Biot's coefficient, b	0.7
Initial matrix pressure, P_{Mi}	3.2×10^7 Pa
Initial hydraulic fracture pressure, P_{hfi}	5.5×10^7 Pa
Initial natural fracture pressure, P_{nfi}	3.2×10^7 Pa
Horizontal stress, S_{Hmax}/S_{Hmin}	5.5×10^7 Pa
Bottom hole pressure, P_{wf}	2 x 10^7 Pa

Initial matrix water saturation, S_{wM}	0.25
Initial hydraulic fracture water saturation, S_{wH}	1
Initial natural fracture water saturation, S_{wN}	1
Initial normal stiffness, K_{ni}	5×10^9 Pa/m
Maximum fracture aperture closure, D_{nmax}	9.8×10^{-4} m

Table 4.2. Parameters used in fluid loss analysis cases.

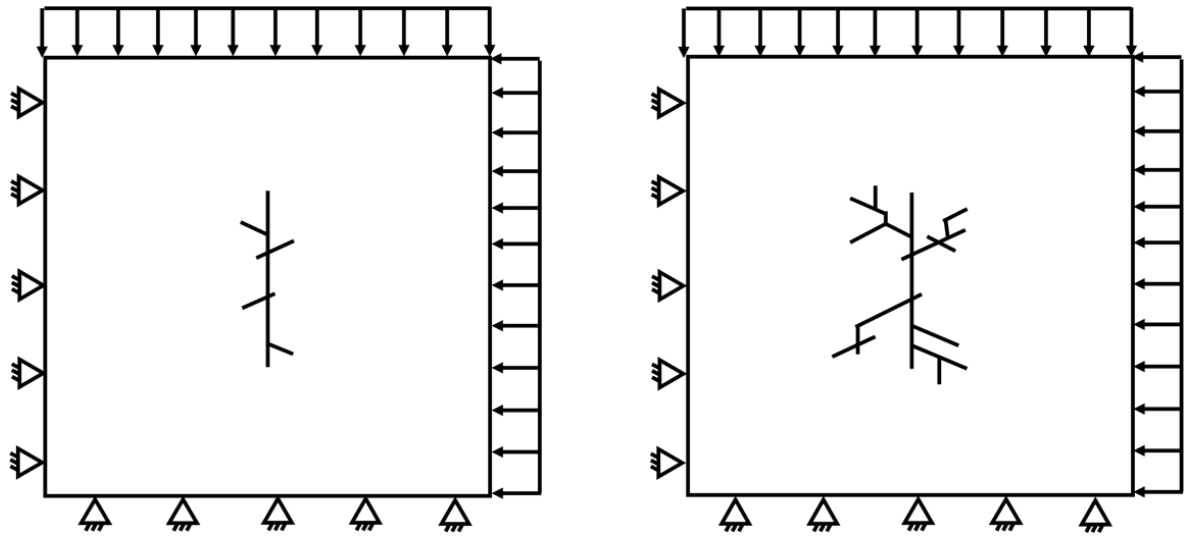

(a) (b)

Figure 4.13. Schematic of the fracture network configuration and boundary conditions for case (a) simple natural fracture network and (b) branching natural fracture network.

4.4.2 Model Initialization

As fracture propagation is not considered in this work, an alternative strategy was adopted to incorporate injection fluid and hydraulic-fracturing treatment (Liu, Liu, et al., 2020; Wang & Leung, 2015; Zhong & Leung, 2020): a well is located at the center of the hydraulic fracture. At the beginning of the shut-in period, the initial pressure of hydraulic fracture is set to be the same as the initial horizontal stress to model the fully open hydraulic fracture and high buildup pressure upon shutting in the well. During the shut-in and flowback periods, the deformation of all fractures

will be calculated in the geomechanical solver and allows fluid within the fractures to flow into the matrix. The shut-in duration is five days, and the production duration is ten days.

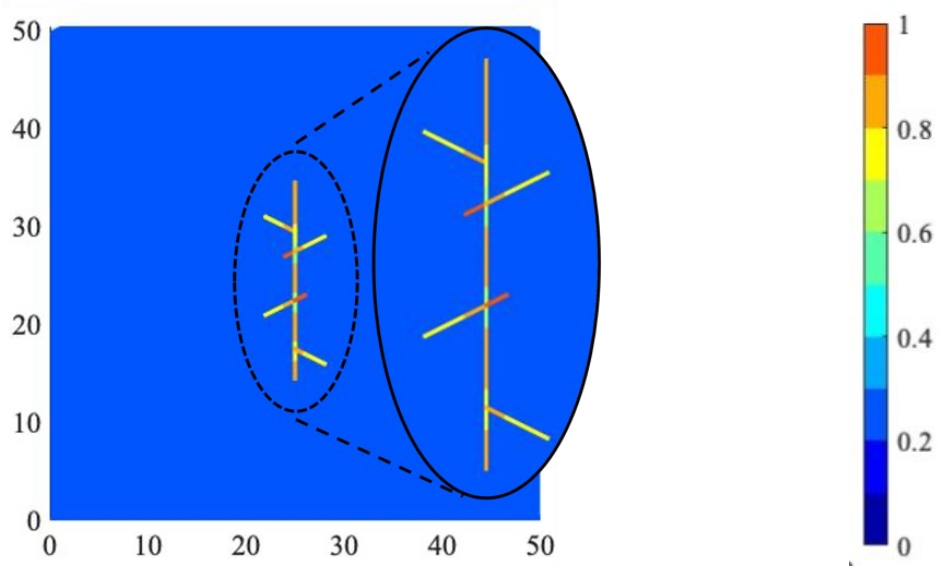

(a)

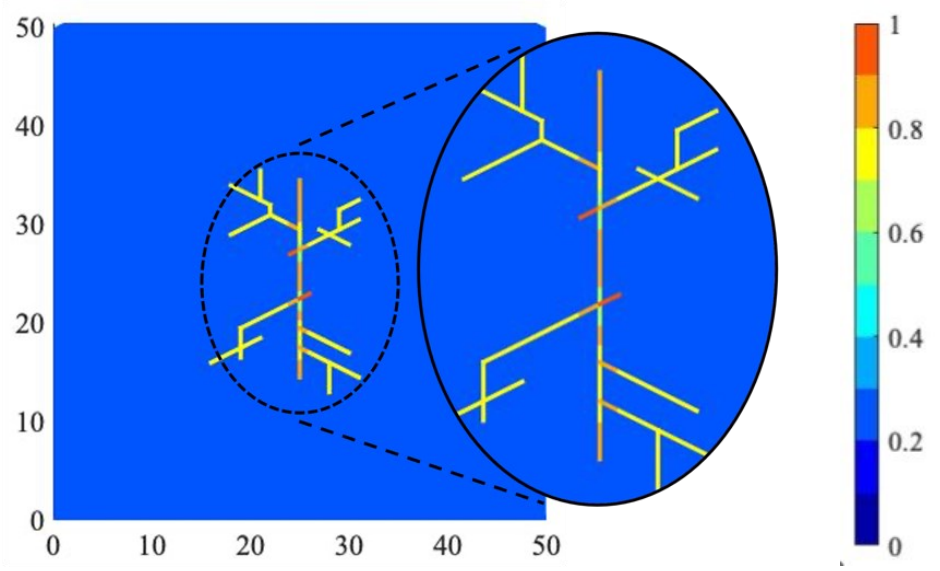

(b)

Figure 4.14. Water saturation distribution for (a) simple natural fracture network and (b) complex natural fracture network after a shut-in period of 5 days.

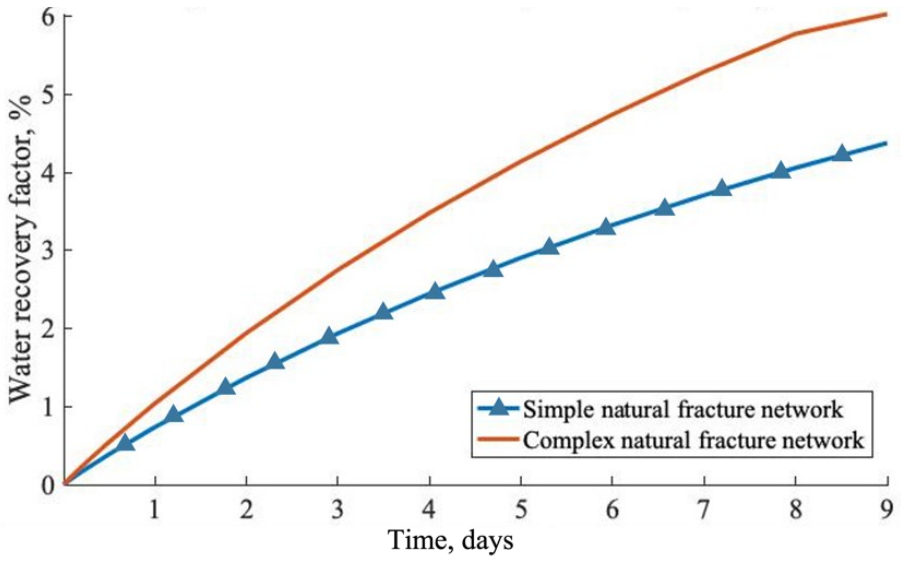

Figure 4.15. Water recovery factor as a function of production time after a 5-day shut-in period.

4.4.3 Results and Discussion

Water saturation distributions after five days of shut-in period for two cases are shown in **Figure 4.14**. Near the intersection among multiple branches of natural fractures, the water saturation is higher (in comparison to the tip regions). However, an opposite trend is observed near the intersection between hydraulic fracture and a natural fracture branch, where the water saturation is the lowest. Liu, Liu, et al. (2020) also reported higher water saturation at the natural fracture intersections, but saturation distribution in hydraulic fracture was not captured in that work. The results clearly illustrate that fracturing fluid flows preferentially from the hydraulic fractures into the natural fractures and then into the matrix; however, given the drastic drop in conductivity between the natural fractures and the matrix, the fluid tends to pool or collect at the intersections.

Figure 4.15 compares the water recovery behavior between the two fracture configurations. Higher water recovery is observed for the more complex network, given more water is present in the natural fractures and the overall conductivity is higher; it is easier to produce water during flow back. This analysis is facilitated by the coupled geomechanical and flow model developed in this

work. The ability to simulate arbitrarily oriented fractures offers a novel opportunity to study mechanistically how the complexity and configuration of fracture networks would affect fracturing fluid recovery. This aspect was often neglected in previous works, where only orthogonal fractures were modeled. The results presented here illustrate that the more complex the natural fracture network intersects with the hydraulic fractures, the faster the fracturing fluid recovery would be during flow back.

CHAPTER 5 : CHARACTERIZATION OF DISTRIBUTED ACOUSTIC SENSING SIGNALS IN HYDRAULIC FRACTURING STIMULATION

5.1 Overview

Low-frequency distributed acoustic sensing (LF-DAS) is one of the promising diagnostic techniques to detect and characterize hydraulic fractures. LF-DAS signals can capture fracture hits and the strain field around the hydraulic fracture. However, the interpretation of field LF-DAS data and the relationship between fluid allocation and production can be challenging due to the complexity of the underground conditions. This study develops a fracture propagation model to simulate the hydraulic fracturing process. The modelling results are analyzed to examine patterns and trends observed in interpreting field DAS data.

The fracture propagation model, coupled with the flow and geomechanical computations, is implemented in the MATLAB Reservoir Simulation Toolbox (MRST). The flow and geomechanical calculations are discretized by the finite volume and the virtual element methods, respectively. The hydraulic fracture is set to propagate along a prescribed path with a specific propagation or activation criterion. The accuracy of our model is validated against the KGD analytical solutions for the leak-off-viscosity and storage-viscosity dominated regimes.

The simulated stress and strain features are consistent with those interpreted from field DAS signals. Several case studies and sensitivity analyses demonstrate the approach's utility and examine fracture interference, closure, and stress shadowing effects. The modelling work facilitates interpreting field measurement data by investigating characteristics of fracture hits from adjacent wells. The modelling method provides insights into fracture interference and its implications on optimal designs during hydraulic fracturing stimulation.

5.2 Fracture Propagation Model

A potential fracture path is prescribed in advance: a fracture consisting of a series of inactive elements is defined. The properties of these inactive fracture cells are the same as the rock properties. It is assumed that the fracture would initiate when the minimum effective stress σ'_{min} at the fracture tip cells is less than a critical stress value σ_c, which is related to the rock's tensile strength. The propagation criterion can be defined as:

$$\sigma'_{min} = (\sigma_y - bp) \leq \sigma_c. \tag{5.1}$$

Once the criterion in **Eq. 5.1** is met, the inactive fracture cell neighbouring the current fracture tip is activated – its properties (porosity, permeability) are updated to those corresponding to the fracture.

The total length of fracture (L_f) is the sum of the lengths (Δl) of all N active fracture cells along the propagation path.

$$L_f = \sum_{i=1}^{N} \Delta l_i, \tag{5.2}$$

5.3 Validation of Fracture Propagation Model

Model validation is essential for the numerical simulation of hydraulic fractures, since it involves a non-linear moving boundary problem, and numerical errors may arise and accumulate during the simulation (Warpinski et al., 1994). There are three commonly used analytical solutions for the fracture propagation model: Khristianovich-Geertsma-Deklerk (KGD) (Geertsma & De Klerk, 1969; Khristianovic & Zheltov, 1955), Perkins-Kern-Nordgren (PKN) (Nordgren, 1972; Perkins & Kern, 1961) and penny-shaped model (Abe et al., 1976). The KGD model is selected for model validation, as it assumes plane-strain deformation in the horizontal plane and a constant

rate of laminar Newtonian flow along the fracture plane. This setup is consistent with the proposed numerical model. There are two competing dissipation mechanisms when considering the KGD model: leak-off vs. storage and viscosity vs. toughness. Four regimes are possible by combining these two sets of mechanisms: storage-viscosity, storage-toughness, leak-off-viscosity, and leak-off-toughness. The KGD fluid leak-off is given by the Carter's model (Howard & Fast, 1957):

$$g(x,t) = \frac{2C_L}{\sqrt{t - t_0(x)}}, \tag{5.3}$$

where $t_0(x)$ is the time when the crack arrives at x, C_L is the leak-off coefficient, and $g(x,t)$ is the leak-off volume per unit length of the fracture. It should be noted that although most assumptions of the KGD model are consistent with the numerical model, the simplified leak-off model does not explicitly consider many important parameters captured in the flow computations, including matrix and fluid properties. Instead, the effects of all these factors are lumped into the single leak-off coefficient.

5.3.1 Storage-Viscosity Dominated Regime

An injection well is located in the middle of the domain, and a single planar hydraulic fracture is modelled. The input parameters are given in **Table 5.1**. In **Figure 5.1**, simulation predictions of increasing fracture half-length with time are compared with the analytical KGD storage-viscosity solution (Adachi & Detournay, 2008), and the two solutions are in good agreement.

Parameters	Value
Model dimension, $L \times L$	50 m × 50 m
Height, h	0.5 m
Matrix porosity, ϕ_M	0.2
Matrix permeability, k_M	1×10^{-12} m^2

Young's modulus, E	17 GPa
Poisson's ratio, v	0.2
Biot's coefficient, b	0.75
Initial reservoir pressure, P_{Mi}	3.5 MPa
Horizontal stress, S_{Hmax}/S_{Hmin}	3.7 MPa
Injection rate, Q_i	0.001 m^2/s
Viscosity, μ	0.1 Pa s

Table 5.1. Parameters used for storage-viscosity dominated regime modelling.

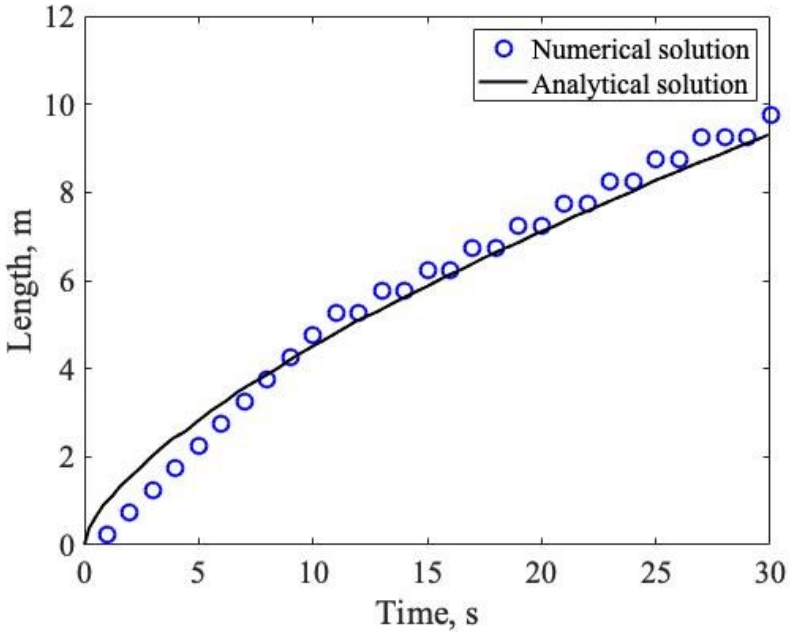

Figure 5.1. Comparison of fracture half-length vs injection time between the storage-viscosity asymptotic analytical and numerical solutions.

5.3.2 Leak-Off-Viscosity Dominated Regime

The same model setup as in the last case is adopted, except for the following parameters: $k_M = 5\times10^{-12}$ m^2, $S_{Hmax} = S_{Hmin} = 7.2$ MPa, and the total simulation time = 200 s. The numerical solution is consistent with Carrier's simulation results for two-dimensional diffusion (Carrier & Granet, 2012) in isotropic media. In contrast, the KGD analytical solution of the leak-off-viscosity regime (Adachi & Detournay, 2008) is inconsistent with the numerical solution. According to

Carrier's explanation (Carrier & Granet, 2012), unidimensional diffusion is assumed in the analytical solution. However, the numerical solution can model the anisotropy in flow conductivity surrounding the fracture, enabling the fracture to grow faster along the direction with more fluid flow.

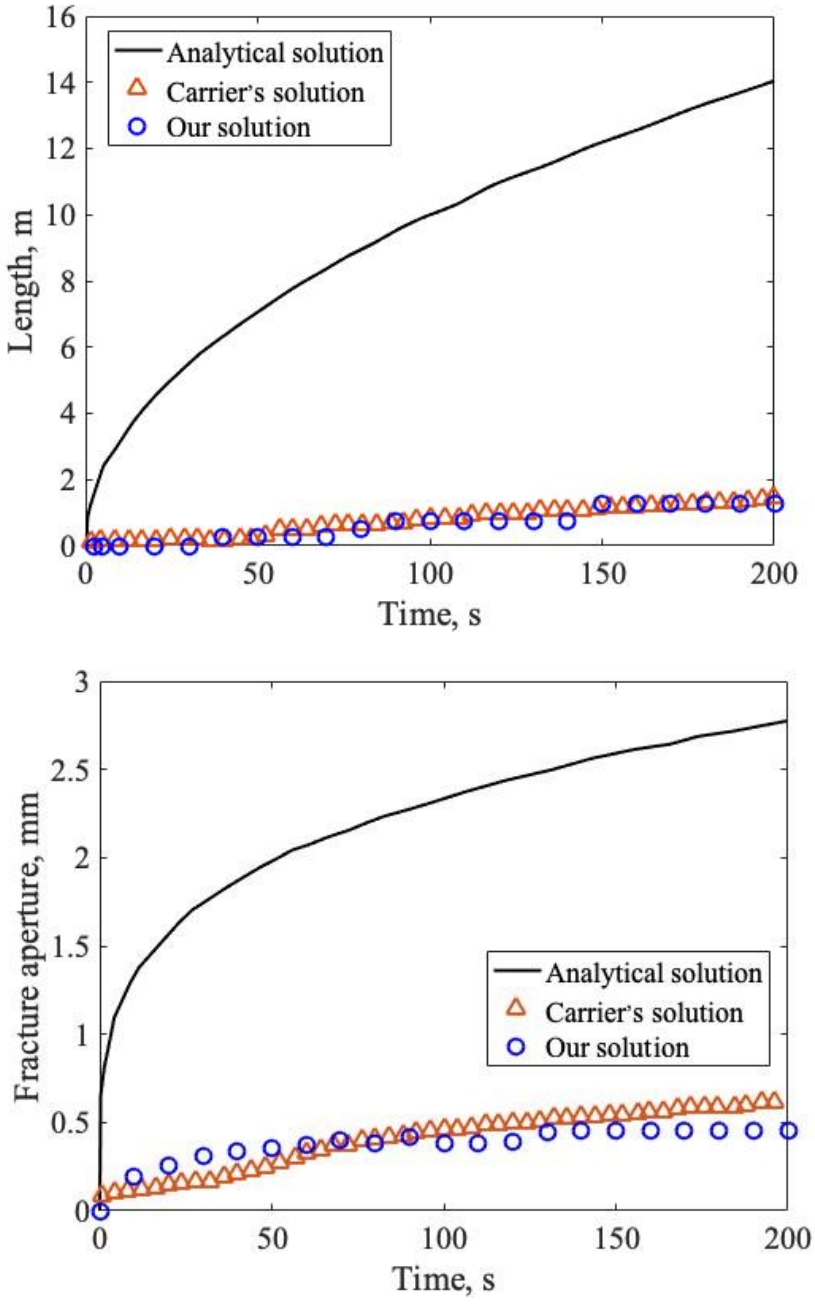

Figure 5.2. Comparison of fracture half-length vs injection time (first row) and fracture aperture vs. injection time (second row) between the leak-off-viscosity asymptotic analytical solution, Carrier's numerical solution, and the numerical solution.

5.3.3 Leak-Off-Toughness Dominated Regime

The model setup is slightly different from the last two regimes, and the different parameters used in this case are listed in **Table 5.2**. Water is injected into the water-saturated matrix. The leak-off coefficient can be calculated by the Carter equation (Howard & Fast, 1957; Valkó & Economides, 1995)

$$\frac{V_L}{A_L} = 2C_L\sqrt{t} + S_p, \tag{5.4}$$

where V_L is the leak-off volume, A_L is the fracture surface area, and S_p is the spurt loss coefficient (Valkó & Economides, 1995).

Parameters	Value
Model dimension, $L \times L$	60 m × 30 m
Height, h	1 m
Matrix permeability, k_M	5×10^{-15} m^2
Fracturing energy, G_c	625 Pa m
Initial reservoir pressure, P_{Mi}	2.5 MPa
Horizontal stress, S_{Hmax}/S_{Hmin}	5.0 MPa
Viscosity, μ	1×10^{-4} Pa s

Table 5.2. The parameters used for leak-off-toughness dominated regime modelling.

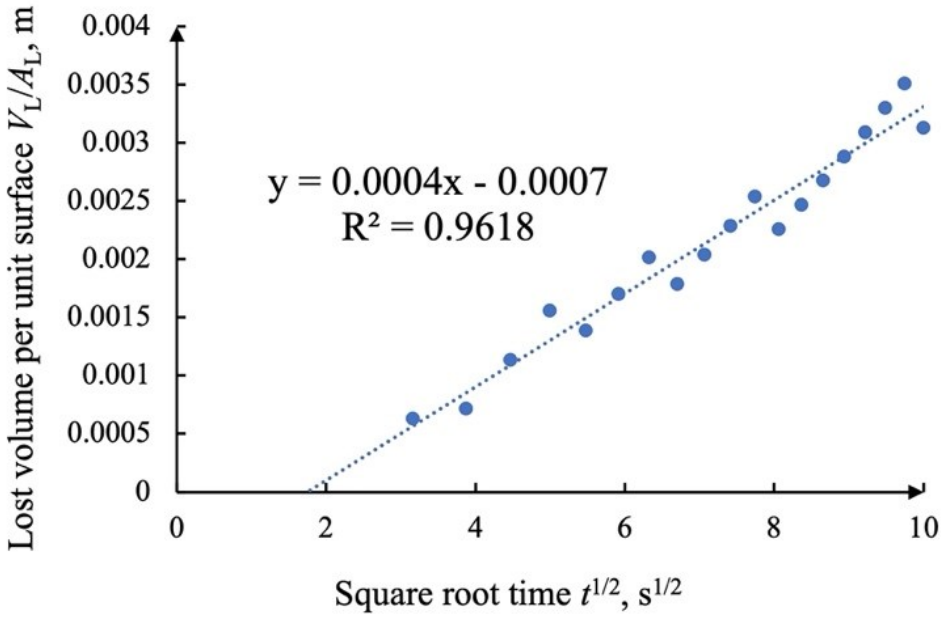

Figure 5.3. The lost volume per unit surface vs. square root time. The leak-off coefficient is obtained from the slope.

Figure 5.3 indicates a strong linear relationship between lost volume per unit surface and square root time. The slope of the linear equation is $2C_L$, so the leak-off coefficient C_L is 0.0002 $m/s^{1/2}$. The analytical solution can be obtained from this leak-off coefficient and other parameters in **Table 5.2** (Bunger et al., 2005). **Figure 5.4** shows a strong agreement in fracture growth computed using the analytical and numerical solutions. It should be noted that not practically observed case of storage-toughness dominated is not considered.

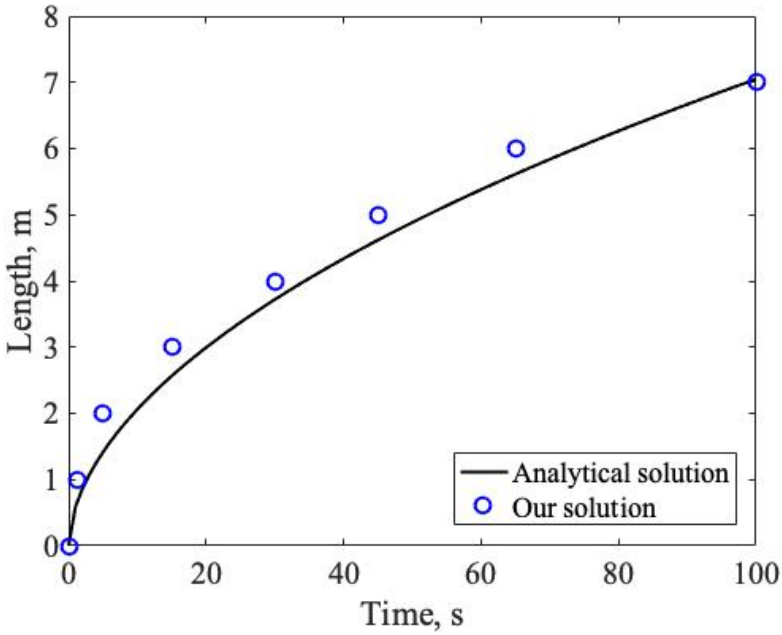

Figure 5.4. Comparison of fracture half-length vs. injection time between the leak-off-toughness analytical and numerical solutions.

5.4 Characterization of DAS Signals

In this section, several fracturing scenarios are examined. The objective is to investigate whether or not these scenarios would explain the features observed in the DAS data. Therefore, the plots of simulated strain and strain rate vs. time (i.e., waterfall plots) are compared against the actual DAS profiles. The model parameters are shown in **Table 5.3**. Due to the symmetry of the setup, only half the domain is modelled, as shown in **Figure 5.5**. No overburden is considered in this study (i.e., only 2D geometry is considered). The injection information and triaxial tests data set in **Table 5.3** and the DAS field data used in this section were provided by an anonymous company. Four horizontal wells are operated with open-hole ball drop completion in the Middle Member of the Montney Formation. Three are treatment wells (or treated well); the other is a monitor well with fiber optic cables installed.

The Montney Formation is located in the Western Canadian Sedimentary Basin in northeast British Columbia and northwest Alberta. It is one of the largest economically feasible resource plays among the shale gas fields (Vishkai et al., 2017). The Montney is divided into three informal members: the Lower Member, the Coquinal Dolomite Middle Member and the Upper Member (Davies et al., 1997). Our data area is in the Coquinal Dolomite Middle Member. It is the area of the Lower Member of the Montney covered in thick dolomitized coquina, forming a nearly continuous unit of 400×30 square kilometres (Davies et al., 1997). The Coquinal Dolomite Middle Member is classified as a tight gas reservoir.

In **Figure 5.5**, the blue line is the treated well, and a perforation is located in its middle. The injection rate through this perforation is considered to be half of the total flow rate $Q_i/2$, as only half of the production area is simulated. The red line is the monitor well with fiber optics installed. The simulated geomechanical responses on this red line represent the predicted DAS signals and are used to construct the waterfall image. The yellow line in the middle is the pre-defined potential growth path for hydraulic fracture, while the green line represents a pre-existing natural fracture or a hydraulic fracture from a previous cluster – a second possible growth path for the hydraulic fracture. In other words, the hydraulic fracture can propagate following the yellow, green, or both paths.

Parameters	Value
Model dimension, $L \times L$	80 m × 100 m
Height, h	1 m
Matrix porosity, ϕ_M	0.06
Matrix permeability, k_M	2×10^{-19} m^2
Hydraulic fracture initial permeability, k_{hfi}	1×10^{-11} m^2
Natural fracture initial permeability, k_{nfi}	5×10^{-13} m^2
Young's modulus, E	38.6 GPa

Poisson's ratio, v	0.22
Biot's coefficient, b	0.75
Initial reservoir pressure, P_{Mi}	2.5 MPa
Horizontal stress, S_{Hmax}/S_{Hmin}	3.7 MPa
Injection rate, Q_i	0.155 m^2/s
Viscosity, μ	0.005 Pa s

Table 5.3. Parameters used for field DAS data comparison.

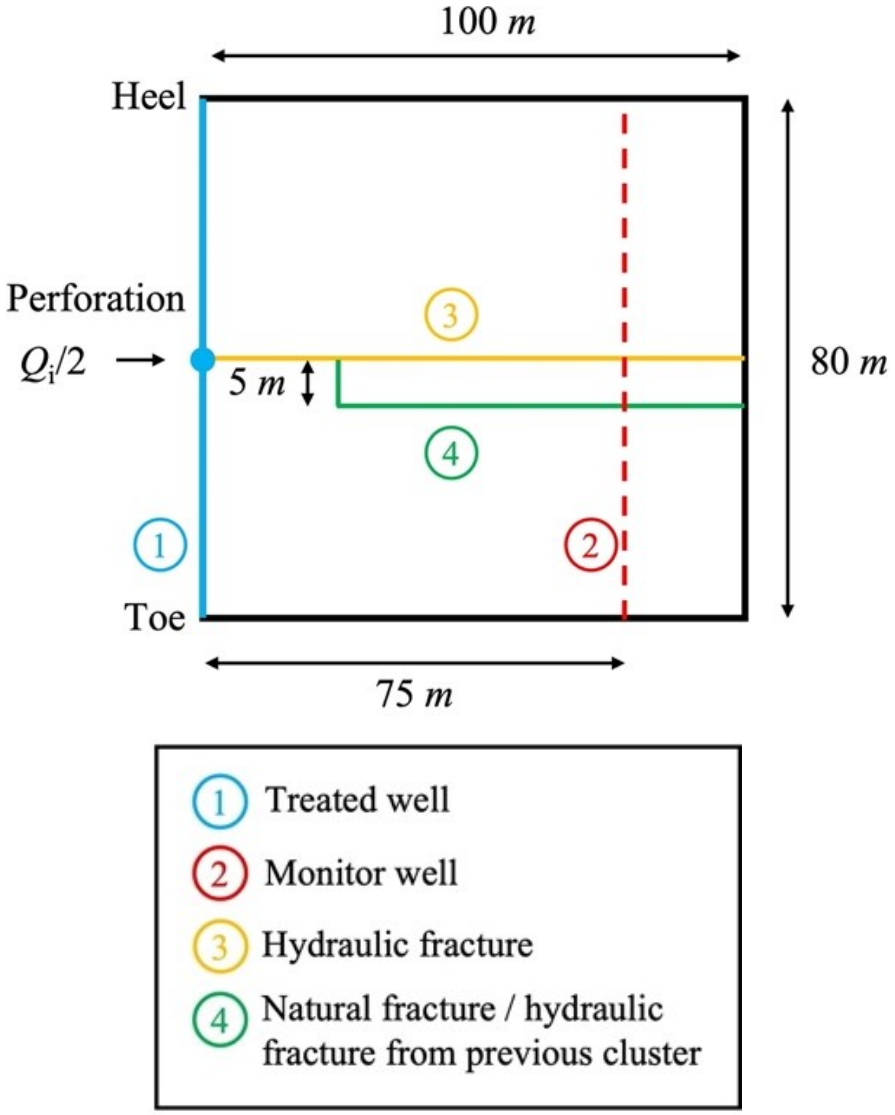

Figure 5.5. A schematic of the top view of the simulation configuration.

5.4.1 Base case

A single planar hydraulic fracture (the yellow line) is simulated, and the green line is not modelled. Fracture trajectories at two different times, along with the strain rate profiles or waterfall images, are plotted in **Figure 5.6**. Red denotes expansion, and blue represents compression in the waterfall images. Heart shape, red band, blue wings, and fracture hit can be observed in numerical simulation results and field DAS data [**Figure 5.6** (d)]. In **Figure 5.6** (a), as the hydraulic fracture from the treated well approaches the monitor well, the expansion signal detected by the cable gradually narrows, but the magnitude increases, making a red heart shape. "Fracture hit" at the monitor well is picked at the bottom of the heart shape. When the hydraulic fracture finally reaches the monitor well [**Figure 5.6** (b)], there is expansion along the fracture path, and the rock around the fracture is compressed, forming red stripes and blue wings in **Figure 5.6** (c) at the dashed line ②. When the fracture passes the monitor well, the fracture continues to open and extends the red band. For the strain rate map [**Figure 5.6** (c)], the blue wings are predicted right after the fracture hit. The narrow blue wings in the strain rate map are consistent with the field DAS data.

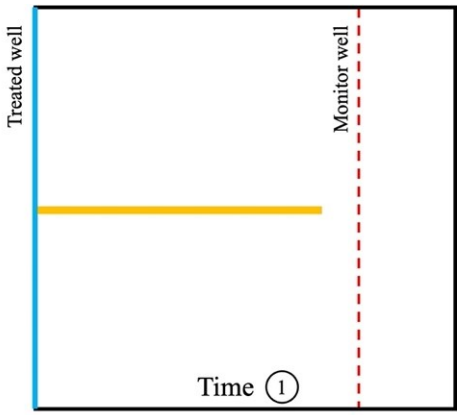

(a) The fracture is approaching the MW

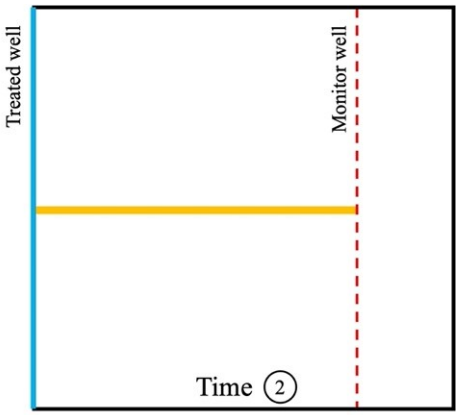

(b) The fracture hits the monitor well

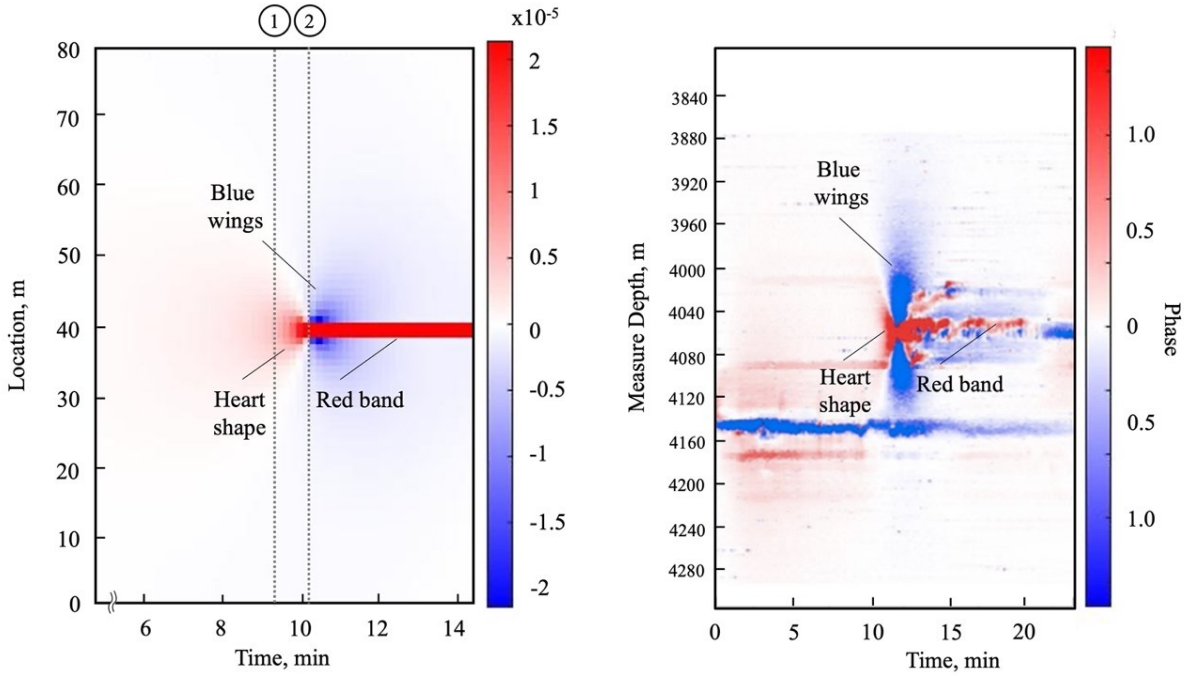

(c) Strain rate map (d) Field DAS data map

Figure 5.6. Base case results: (a) hydraulic fracture trajectory as it approaches the monitor well; (b) hydraulic fracture trajectory as it hits the monitor well; (c) waterfall image of the simulated strain rate; (d) real DAS data for comparison.

5.4.2 Multi-Frac Case

In the second case, the hydraulic fracture will initiate from the perforation along the yellow line in **Figure 5.5** and split into two branches when it reaches the intersection of the green and yellow lines. **Figure 5.7** shows fracture trajectories at two different times, and the waterfall image of changing stress along the monitor well in our model and DAS data show similar characteristics.

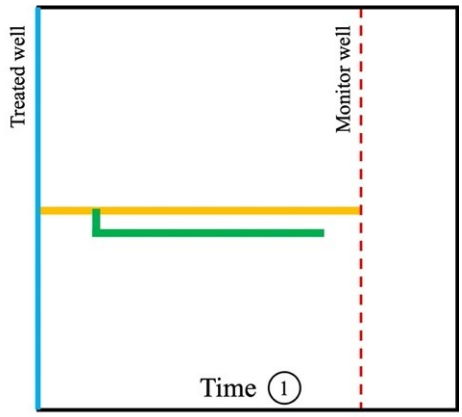

(a) The main fracture hits the MW

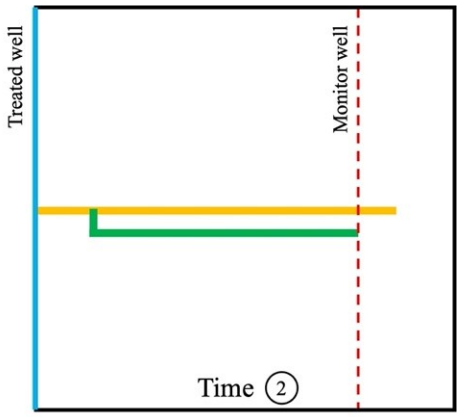

(b) The lateral fracture hits the MW

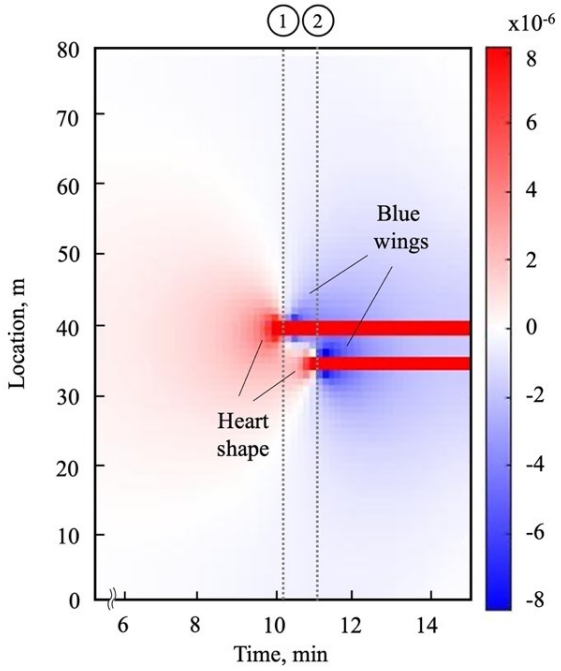

(c) Strain rate map

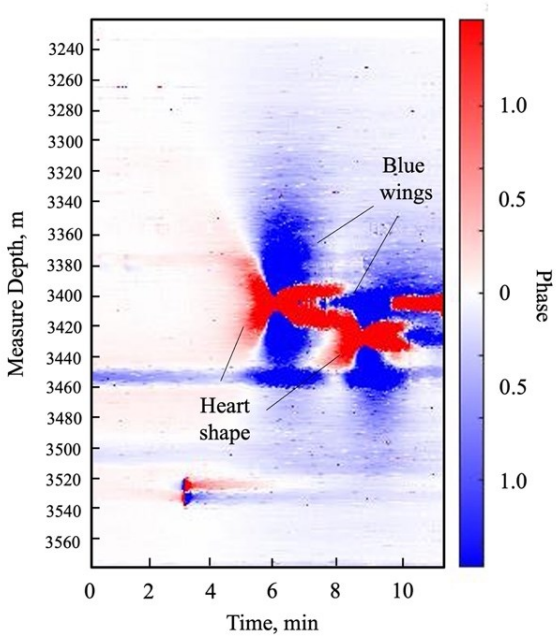

(d) Field DAS data map

Figure 5.7. Multi-frac case results: (a) fracture trajectory as the main fracture approaches the monitor well; (b) fracture trajectory as the lateral fracture hits the monitor well; (c) waterfall image of the simulated strain rate; (d) real DAS data for comparison.

In the strain rate map, two red bands are observed corresponding to the two fracture branches, with both exhibiting features of a heart shape. At time ①, the main hydraulic fracture hits the monitor well, and the branching fracture (green path) is still far away from the monitor well. A complete heart shape of the main fracture has been formed at time ① in **Figure 5.7** (c), and the heart shape for the lateral fracture is just about to form. At time ②, the second fracture hits

the monitor well and makes a complete heart shape in the strain and strain rate maps. When both fractures pass through the monitor well after time ②, they leave two red stripes in the waterfall images. The narrow blue wings in the strain rate map are much smaller than those in the field DAS data map since some input parameters are unknown and may differ from the real reservoir settings. Therefore, a qualitative comparison is achieved. Similar features of two close fracture hits with two heart shapes can also be found in the DAS data, as shown in **Figure 5.7** (d). This case illustrates that if multiple heart shapes are captured in one stage, multiple fracture branches could be responsible for creating these fracture hits.

5.4.3 Antenna case

Another common signature identifiable from field DAS data is an antenna. An antenna is a red band without an obvious heart shape, such as that detected right before the fracture hits discussed in the previous two cases (Ortega Perez, 2022). The antenna is usually located physically close to the hydraulic fracture and intersects with a heart shape, as shown in **Figure 5.8** (d). The green line in **Figure 5.5** is treated as a pre-existing fracture to simulate a possible mechanism for this case. When the yellow hydraulic fracture reaches the intersection of the green and yellow lines, the green hydraulic fracture is reactivated and starts to expand. **Figure 5.8** presents fracture trajectories at two different times, the waterfall plots of strain rate along the monitor well simulated in this case, and a portion of the field DAS data showing the antenna characteristics.

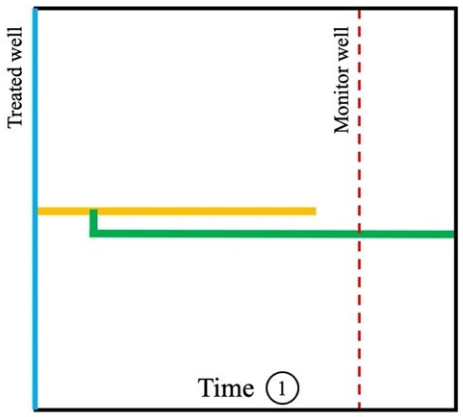

(a) The adjacent fracture is reactivated

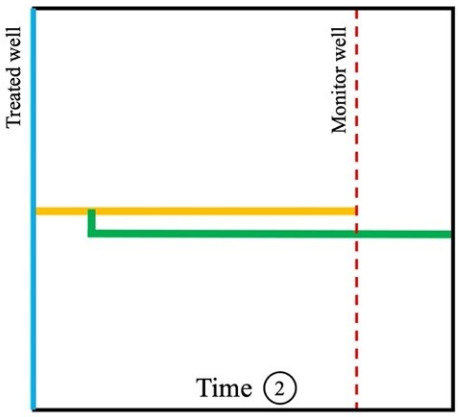

(b) Hydraulic fracture hits the MW

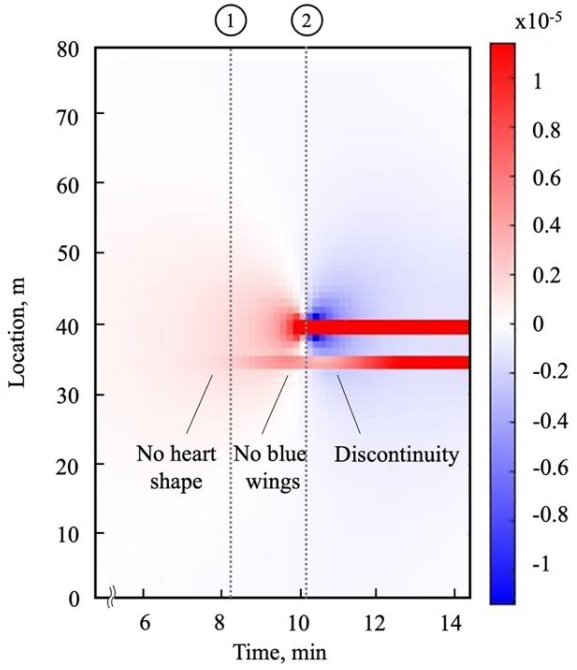

(c) Strain rate map

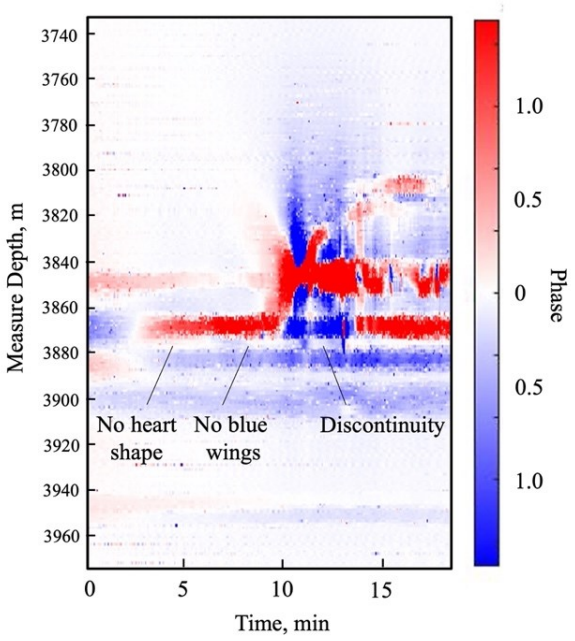

(d) Field DAS data map

Figure 5.8. Antenna case results: (a) fracture trajectory as the main fracture approaches the monitor well; (b) fracture trajectory as the lateral fracture is reactivated; (c) waterfall image of the simulated strain rate; (d) real DAS data for comparison.

After pre-existing fracture starts to expand, it shows that in both numerical maps and field data, there is no heart shape on the tip of the antenna strip and no blue wings on the sides. It illustrates that the fracture at this location already exists. When a hydraulic fracture near it approaches this pre-existing fracture, it is reactivated and starts to grow. Since it is a pre-existing

fracture, it does not propagate toward the monitor well; hence, the signature of a typical fracture hit (i.e., heart shape and blue wings) is missing. The main hydraulic fracture continues to grow after the intersection and follows the yellow path – it initiates from the perforation and gradually extends to the monitor well, creating the heart shape and blue wings in the strain rate map, as shown in **Figure 5.8** (c). **Figure 5.8** (c) and (d) show the antenna bands break after time ② (labelled as "discontinuity") in **Figure 5.8** (c). One interpretation for this feature is that the branch fracture is affected by the stress shadow from the hydraulic fracture, resulting in reduced propagation of this fracture. The numerical simulation results demonstrate that an antenna strip in the DAS waterfall image can correspond to a pre-existing fracture being reactivated by an intersecting hydraulic fracture and reaching the monitor well prior to the fracture hit of the main hydraulic fracture.

5.5 Sensitivity analysis

5.5.1 Effects of Natural Fracture Initial Permeability

A higher initial permeability of branch fracture is simulated as not all antenna stripes have discontinuities in the field data; an example of the field DAS data is shown in Figure 5.9 (b). The initial permeability, k_{nfi}, is increased to 1000 mD. The results are compared to the base case.

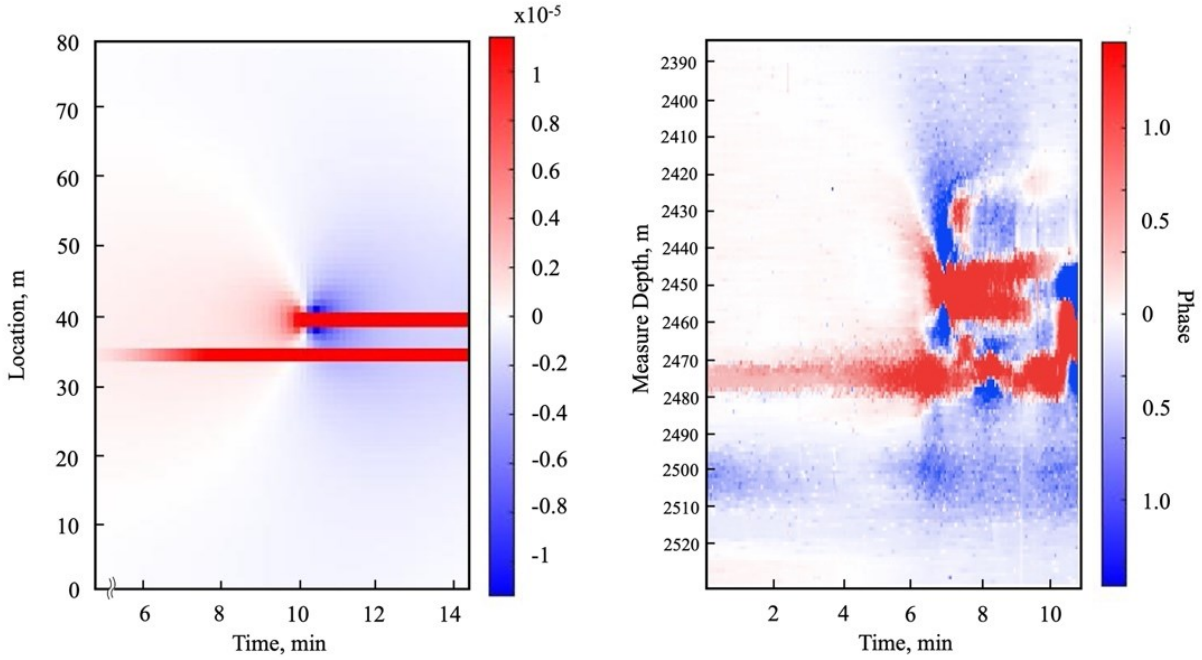

(a) Strain rate map when k_{nfi} = 1000 mD (b) Field DAS data map

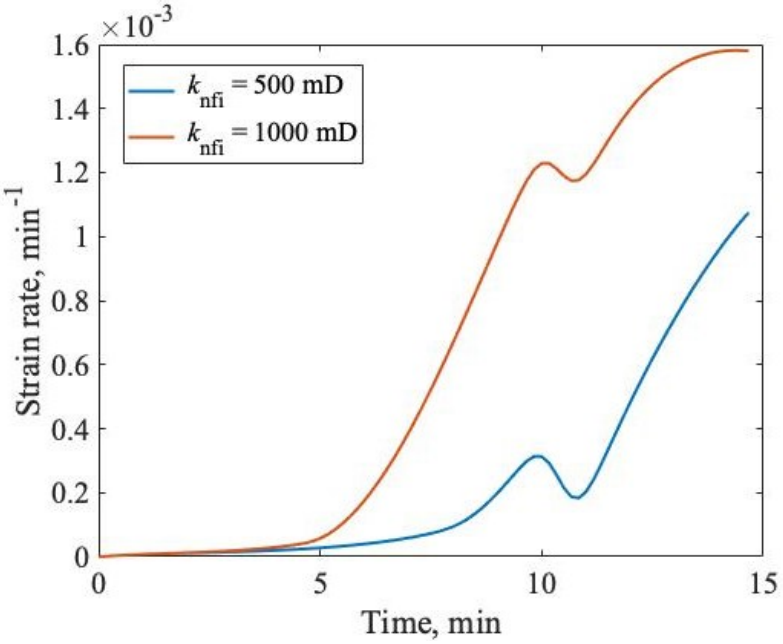

(c) Strain rate vs. time at location = 35 m

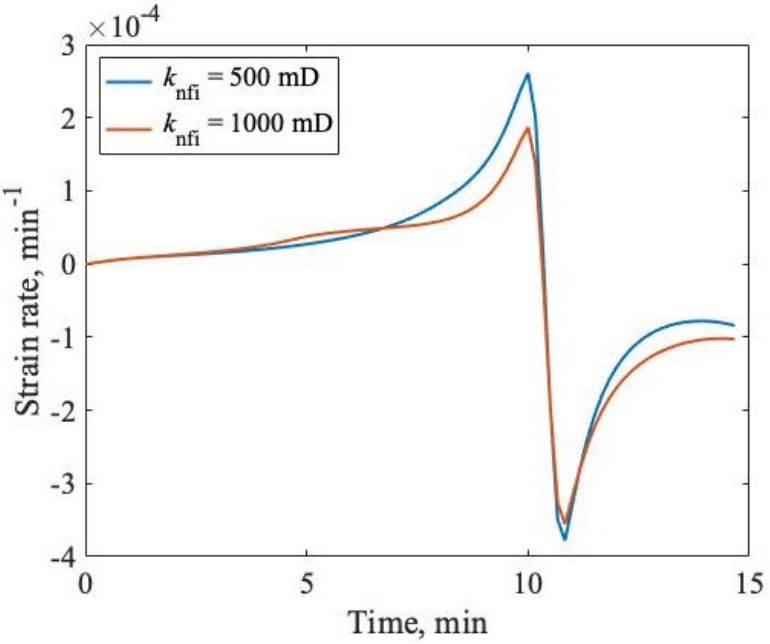

(d) Strain rate vs. time at location = 38 m

Figure 5.9. Waterfall images of (a) simulated strain rate and (b) real DAS data for a higher k_{nfi} case. Comparisons of strain rate vs. time at (c) location = 35 m and (d) location = 38 m between two different k_{nfi}.

Comparing **Figure 5.9** (a) with **Figure 5.8** (c) shows that the antenna stripe is longer and more continuous with higher k_{nfi}. **Figure 5.9** (c) also confirms that at the location where the branch fracture intersects the monitor well, higher k_{nfi} leads to higher strain rate increment and less reduction in strain rate after the fracture hit (in the 10th min), explaining why the antenna is less affected by stress shadowing effects. **Figure 5.9** (d) shows the strain rate evolution at a location between the main hydraulic fracture and the branch fracture. The trends for these two cases are similar, but the peak value is lower with higher k_{nfi}. The numerical results in this section demonstrate that if a continuous antenna signal is observed in the field DAS data, the permeability of this pre-existing fracture might be high.

5.5.2 Effects of Monitoring Well Location

Three monitor wells at different locations are compared to investigate the effects of the monitor well location (or distance between the monitor and treatment wells). The distances between the treatment well and the three monitor wells D_M are 35 m, 55 m, and 75 m. The corresponding strain rate maps are presented in **Figure 5.10** (a), (c), and (e), and the comparison of strain rate as a function of time at locations = 40 m, 38 m, and 35m are shown in **Figure 5.10** (b), (d), and (f), respectively. These locations correspond to the point where the main hydraulic fracture would hit, the point in the middle of two fractures, and the antenna in the strain rate waterfall plots, respectively.

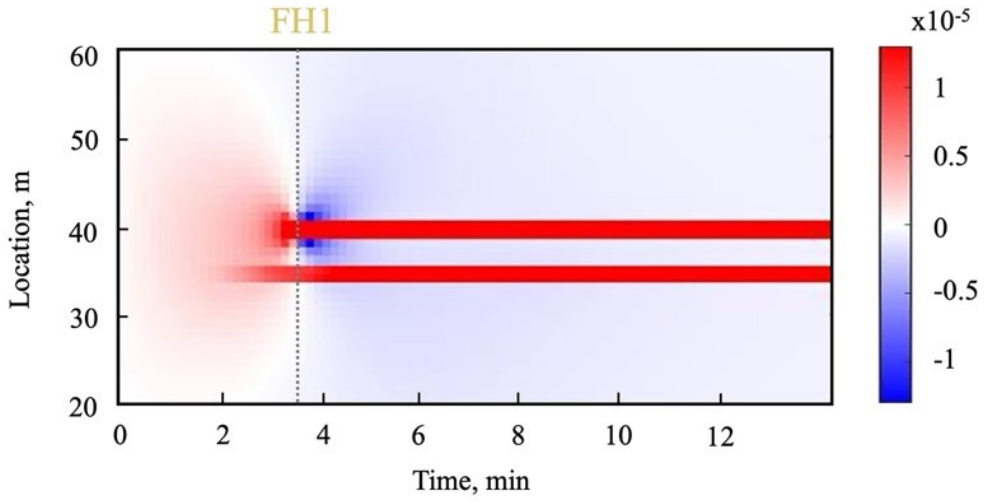

(a) Strain rate map when D_M = 35 m

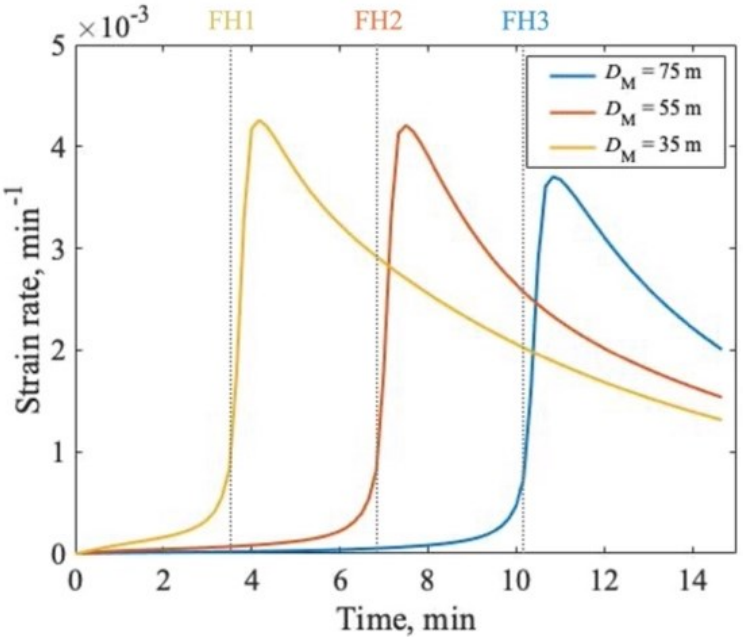

(b) Strain rate vs. time at location = 40 m

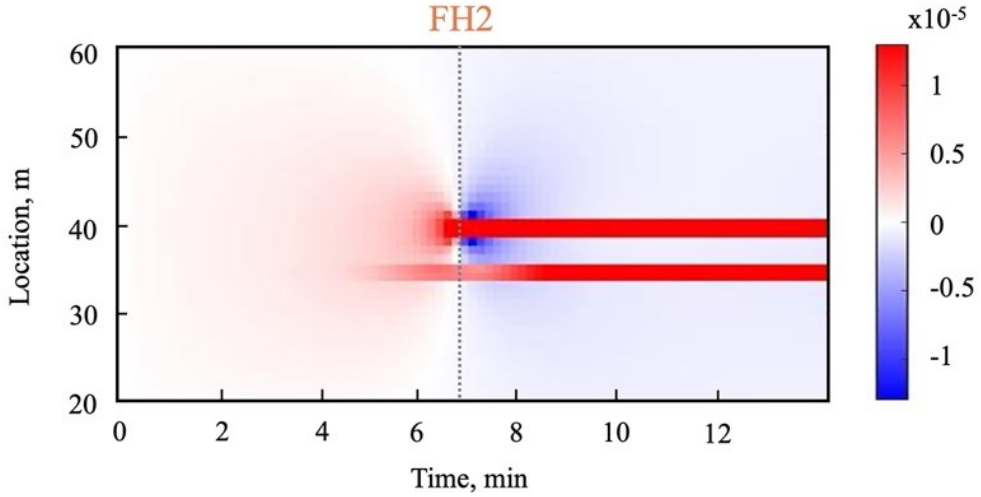

(c) Strain rate map when D_M = 55 m

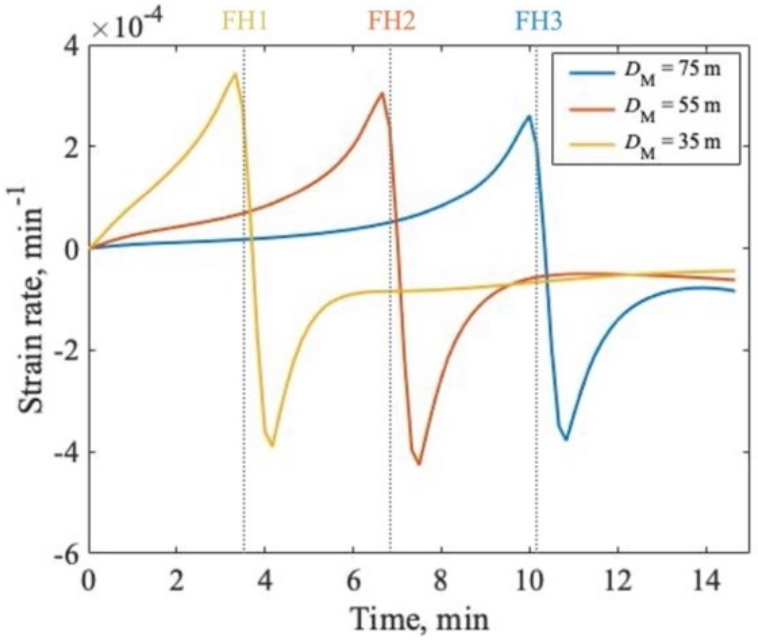

(d) Strain rate vs. time at location = 38 m

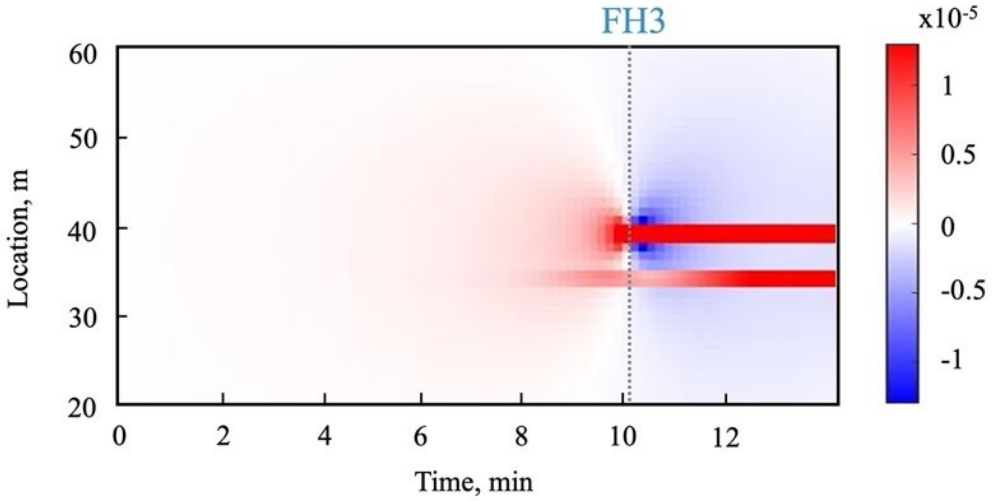

(e) Strain rate map when D_M = 75 m

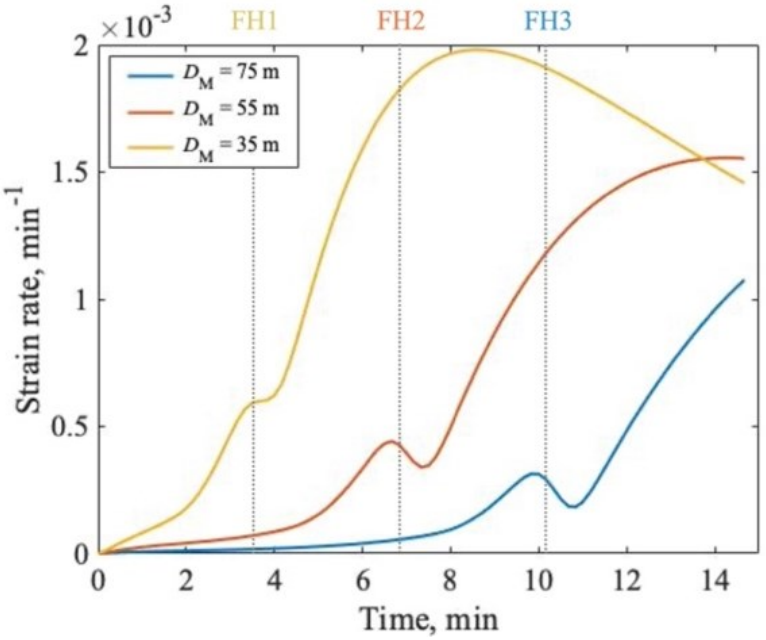

(f) Strain rate vs. time at location = 35 m

Figure 5.10. Waterfall images of simulated strain rate at (a) D_M = 35 m, (c) D_M = 55 m, and (e) D_M = 75 m. Comparison of strain rate vs. time on three monitor wells at locations of (b) 40 m, (d) 38 m, and (f) 35 m.

Figure 5.10 (b) illustrates that when the main fracture hits the monitor well (at times FH1, FH2, and FH3), the strain rate increases rapidly and then decreases, always maintaining a positive value. It means that the main hydraulic fracture expands continuously, but the expansion speed of the fracture slows down after the fracture hits. The peak value of the strain rate also decreases with the increase of D_M, which is consistent with the observations of Liu, Wu, et al. (2020). It indicates that the further the fracture grows, the slower it expands. It is hard to identify the strain rate changes in the waterfall images due to the small range of the colour bar.

Figure 5.10 (d) shows the strain rate evolution between two fractures at location = 38 m. The strain rate remains positive until the fracture hits in each case (FH1, FH2, and FH3), confirming the absence of compression zones or blue wings around the antenna stripes. **Figure 5.10** (f) shows the same plot at location = 35 m. The strain rate gradually increases before each

fracture hit, but the increase is much more gradual than in **Figure 5.10** (b). At the time of each fracture hit, the strain rates are affected by the stress shadowing effects from the main fracture, resulting in a slight initial decrease, followed by continued growth (as previously explained regarding the discontinuity). This decrease becomes more pronounced with greater distance from the treatment well. The growth rate of strain rate is very high when D_M = 35 m, indicating that strong expansion of reactivated branching fracture is observed when it is close to the treatment well, causing the antenna signal to be less susceptible to the shadowing effects. The strain rate deduction is observed in all waterfall plots, **Figure 5.10** (a), (c), and (e); the further away the monitoring well is, the discontinuities in the antenna stripes are more clearly observable.

5.5.3 Effects of Matrix Permeability on the Heart Shape Size

To investigate the effect on the heart shape size, we analyzed the sensitivity of strain changes along the fiber optic for different rock permeabilities in this section. Two cases of rock permeability of 2×10^{-18} m^2 and 2×10^{-17} m^2 are built respectively and compared with the base case. **Figure 5.11** shows strain and strain rate response to different rock permeability. Comparing **Figure 5.11** (a), (c) and (e), or (b), (d) and (f), the heart shape size increases with the increasing matrix permeability. This illustrates that the surrounding matrix has relatively high permeability when the large heart shape is observed in the field DAS data.

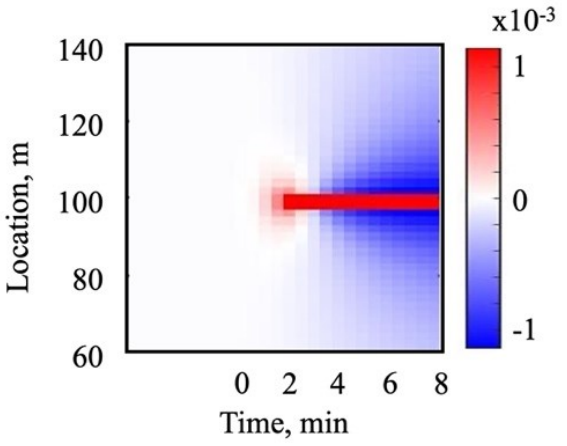

(a) Strain map for the base case

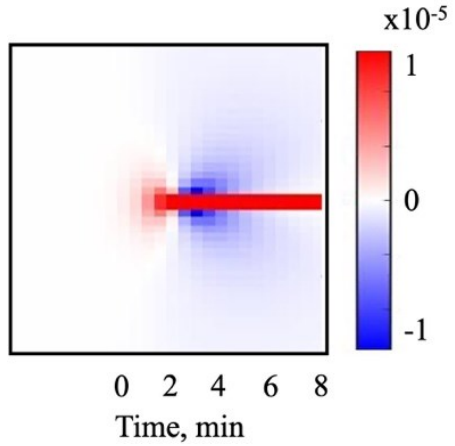

(b) Strain rate map for the base case

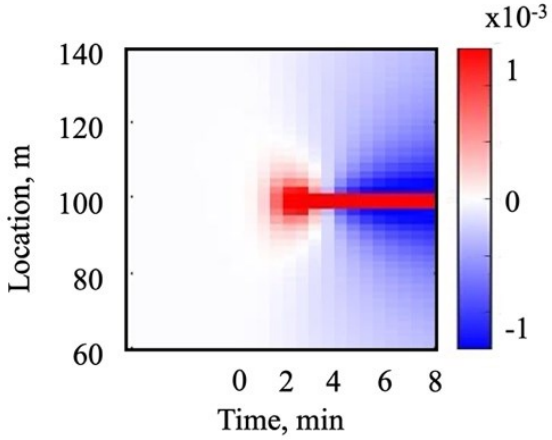

(c) Strain map for $k_M = 2\times10^{-18}$ m^2

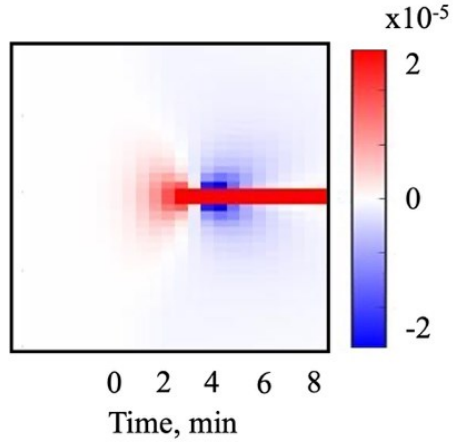

(d) Strain rate map for $k_M = 2\times10^{-18}$ m^2

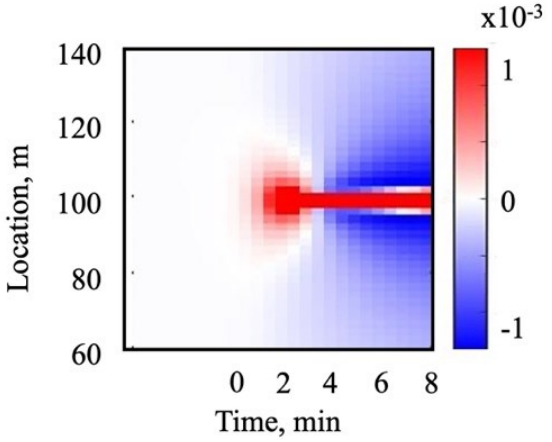

(e) Strain map for $k_M = 2\times10^{-17}$ m^2

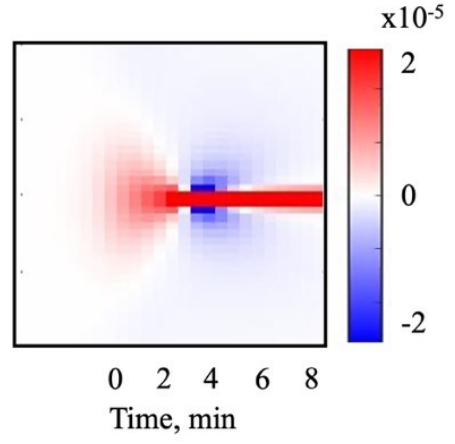

(f) Strain rate map for $k_M = 2\times10^{-17}$ m^2

Figure 5.11. Strain and strain rate maps for different matrix permeabilities. The first row shows (a) strain and (b) strain rate maps of the base case. The second row represents (c) strain and (d) strain rate plots of the case with matrix permeability of 2×10^{-18} m^2. The (e) strain and (f) strain rate plots of matrix permeability of 2×10^{-17} m^2 are shown in the third row.

CHAPTER 6 : HYDRAULIC FRACTURING MONITORING WITH DAS AND ANALYSIS OF FRACTURE HIT IMPACT ON FRACTURING STIMULATION AND PRODUCTION

6.1 Overview

The optimization of well completions is a complex process due to the interdependence of various parameters. One potential solution is the utilization of Distributed Acoustic Sensing (DAS) technology, which enables continuous monitoring of fracture geometry and production at each stage of the wellbore. However, the implementation of DAS technology remains relatively scarce within the industry.

Numerous studies have explored the positive and negative effects of fracture hits on production and the influence of well interference on fracture geometry. However, these investigations primarily concentrate on the parent and child well process. It is worth noting that hydraulic fracture propagation and the occurrence of fracture hits from infill wells can be significantly influenced by the pre-existing pressure depletion surrounding the parent well. In the field data presented in this paper, a sequential treatment approach was employed for four wells; the hydraulic fracturing process was primarily affected by stress shadowing resulting from the fractures of offset wells and previous stages.

This chapter presents several case studies utilizing an in-house numerical simulation model and raw DAS data analysis to explore the effects of cross-well fracture hits and completion designs on fracture propagation and production conductivity. Additionally, a comparative analysis considering microseismic is presented to assess the impact of stress shadowing on the fracture length close to the heel of the wellbore. The field data presented in this chapter are appropriately

interpreted through the comparison with the simulation results, providing valuable insights into the examined phenomena. This work has several novelties. Firstly, the simulation results reveal new insights into optimizing completion designs. Second, the models are analyzed to test various scenarios of cross-well fracture hits and the corresponding DAS signals. The results of this study can help make informed decisions regarding completion parameters, ultimately leading to improved well productivity and efficiency.

6.2 Project Setup

6.2.1 Well Layout

Four horizontal wells are operated with open-hole ball drop completion in the Middle Member of the Montney Formation. Well A is the monitoring well with fiber optic cables installed. Wells B, C, and D are offset wells treated sequentially. The wells are situated in a similar depth formation and are separated by distances of 150 m between wells A-B, and A-D, and 300 m between wells A-C. Furthermore, wells B and D are vertically deployed along the same section.

6.2.2 Data Acquisition Schedule

Step	Duration	Well	Total Num of Stages	Process	Data Type
1	Day 01-03	Well B	39	Treatment	FFS
2	Day 03-06	Well C	37	Treatment	FFS
3	Day 07-10	Well D	38	Treatment	FFS
4	Day 11-16	Well A	18	Treatment	NW
5	Day 39-41	Well A	-	Production	NW

Figure 6.1. Data acquisition schedule. FFS is far-field strain data, and NW is near-wellbore monitoring data.

The data acquisition schedule of the project is illustrated in **Figure 6.1**. Well B initiated the treatment first, encompassing 39 stages over three days. Subsequently, Well C commenced its treatment immediately after, comprising 37 stages completed within three days. Following that, Well D began its treatment with 38 stages. Lastly, Well A began its treatment with 18 stages lasting five days. The production of Well A commenced 23 days after the treatment was completed.

The DAS data collected for Wells B, C, and D are low-frequency far-field strain (FFS) measurements, while for Well A, high-frequency near-wellbore (NW) monitoring data was obtained. DAS technology offers diverse applications in multiple regions, including far-field and near-wellbore regions (Ugueto et al., 2019; Webster et al., 2013; Wu et al., 2020). In the case of FFS data (also known as DAS strain fronts (Ugueto et al., 2019)), DAS is recorded in an offset well, enabling the determination of fracture interactions and hydraulic fracture geometry. Since 2017, Jin and Roy (2017) have demonstrated the application of Low-Frequency DAS (LF-DAS) in monitoring strain and temperature perturbations originating from the far-field region. NW data refers to DAS measurements captured within the treatment well itself. NW data provides valuable insights into fluid flow among different clusters, facilitating the quantification of fluid allocation and the assessment of cluster efficiency (Molenaar et al., 2012; Webster et al., 2013). The color bar used for the FFS data represents a phase, where red represents extension and blue indicates compression. On the other hand, the color bar for the NW data represents signal power, with red indicating higher power and blue indicating lower power. Further discussions regarding these two types of data and their interpretations can be found in the subsequent sections, specifically in **Figure 6.2** and **Figure 6.4**, respectively.

6.3 Methodology

6.3.1 Far-Field DAS Data Characteristics

Figure 6.2 shows the low-frequency FFS response and its engineering curves for a single stage. The graph, also known as a DAS strain front or waterfall plot, uses red to indicate extension and blue to denote compression. As the hydraulic fracture approaches the fiber-optic sensor from the offset well, the magnitude of the expansion signal detected by the cable gradually increases. In contrast, the width of the signal narrows, resulting in a distinctive red heart shape prior to the fracture hit. Upon the hydraulic fracture reaching Well A, there is a consequent expansion along the fracture path while the surrounding rock is compressed, represented by blue wings on either side of the fracture. As the injection ceases, the hydraulic fracture starts to close, and the strain pattern reverses from red to blue, creating a blue tail following the red stripe. This region, where the injection ends, is called the relaxation zone (Ortega Perez, 2022). Signal tails from previous stages are identifiable by their lack of the red heart shapes characteristic of the current stage.

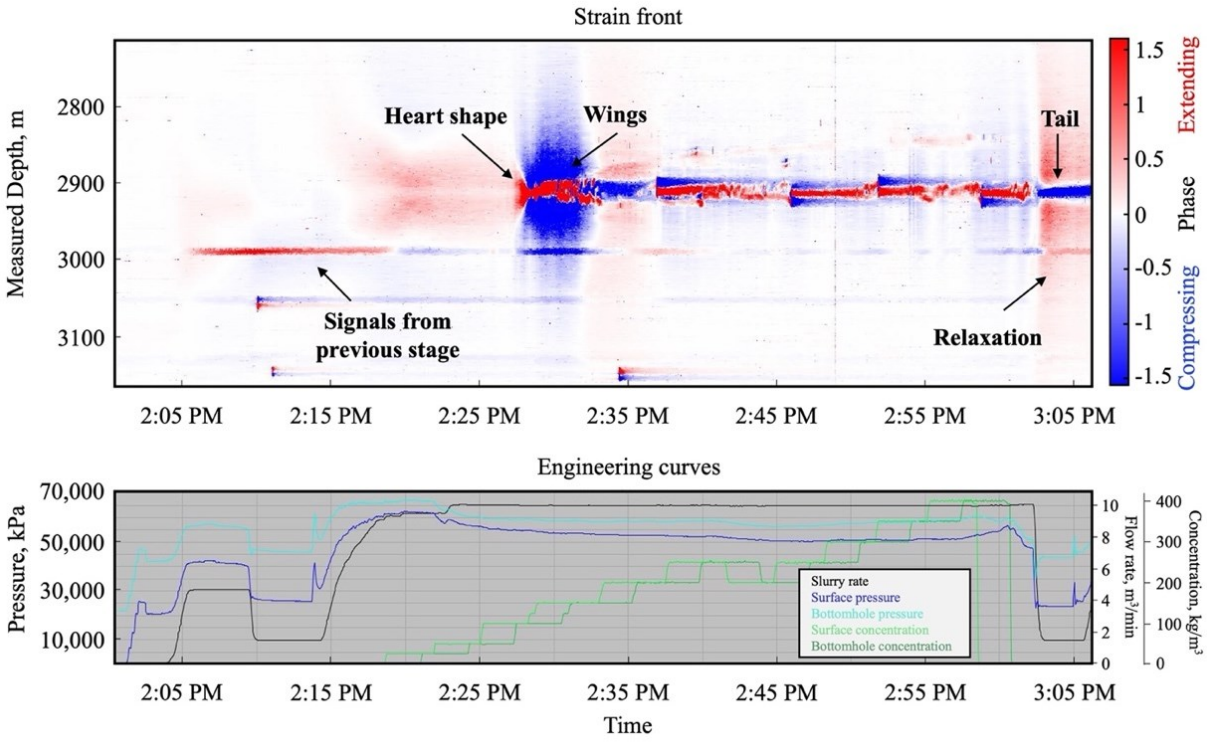

Figure 6.2. (Top) FFS observed at an offset well and (bottom) engineering curves of a single stage.

6.3.2 Measurement Depth of Fracture Hit

It is imperative to determine the measured depth (MD) at which the fracture intersects the fibre optics on Well A. Whenever a heart shape is observable, its location can be used to estimate the fracture hit MD. **Figure 6.3** illustrates the process for identifying a fracture hit in the N+1 stage, where the top and bottom depths of the heart shape are selected, and their midpoint is considered the fracture hit MD (Ortega Perez, 2022). The plot also shows that a small heart shape at the signal tail from one of the previous stages is often observable, indicating possible leaks of internal plugs. However, such signals are not considered as new fracture hits in this work.

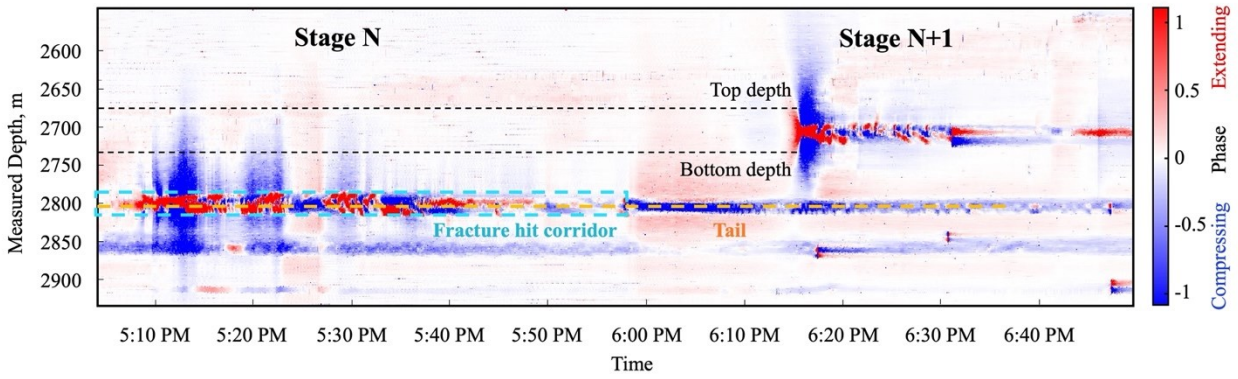

Figure 6.3. Three approaches are used in this work to identify the fracture hit MD: the midpoint of the top and bottom depths of the heart shape, the center line of the fracture hit corridor (blue dotted rectangle), and the midpoint of the blue tail (yellow dash line).

Heart shapes are not always observed, such as in stage N in **Figure 6.3**. In this case, a fracture hit corridor is defined, and its centerline is selected as the fracture hit MD. Fracture-hit corridors (FHC) represent areas of open fractures or the portion of the monitoring well containing the intercepting hydraulic fractures (Ugueto et al., 2019; Wu et al., 2020). FHC consists mainly of the extending red region in the blue dotted rectangular in **Figure 6.3**. Finally, the MD of the blue tail can be considered as an additional constraint for identifying fracture hits (Y. Liu et al., 2021), as it represents fracture closure after injection stops. By incorporating the MD of the blue tail, the accuracy of fracture hit identification can be further improved. The MD of the blue tail for stage N is represented by a yellow dash line in **Figure 6.3**, and the MD of the blue tail coincides with the centerline of the FHC.

6.3.3 Near-Wellbor DAS Data

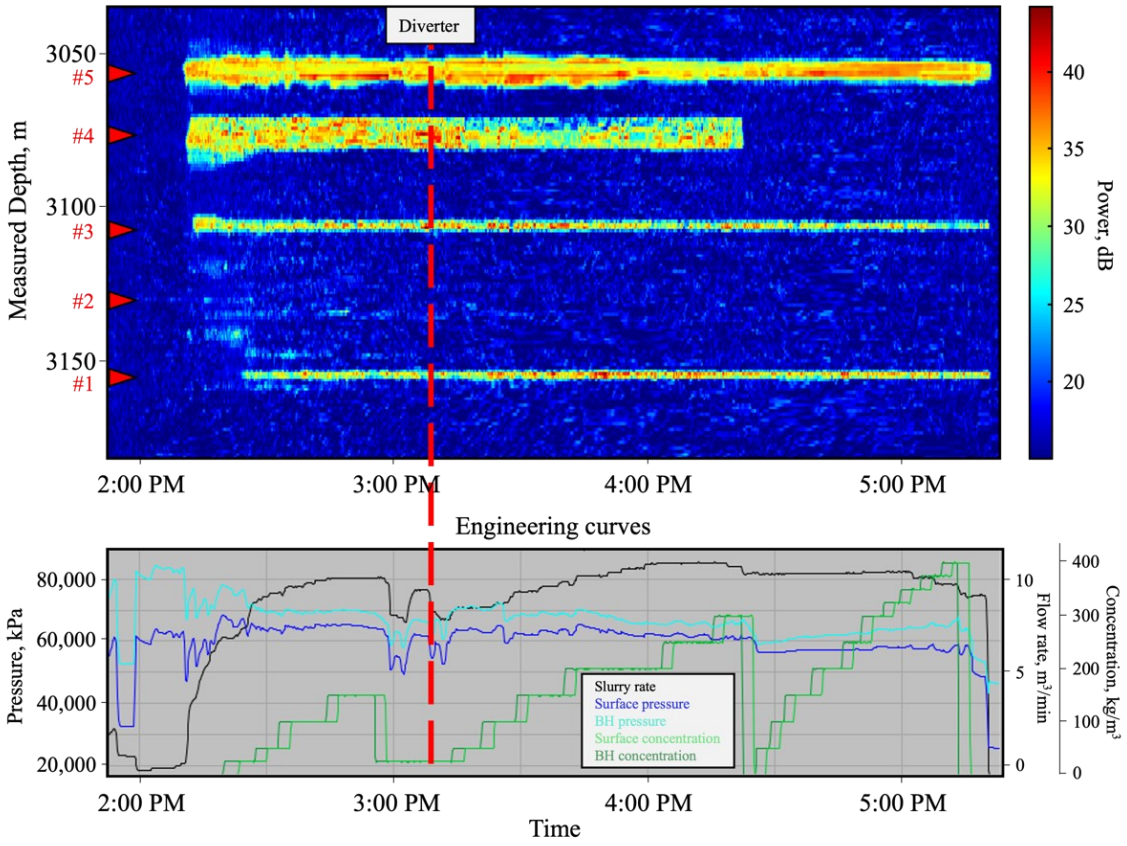

Figure 6.4. Processed High-frequency DAS measurements (200-2000 Hz) from a single stage of the monitoring well. The red triangle is the perforation, and the red dash line is the time for diversion.

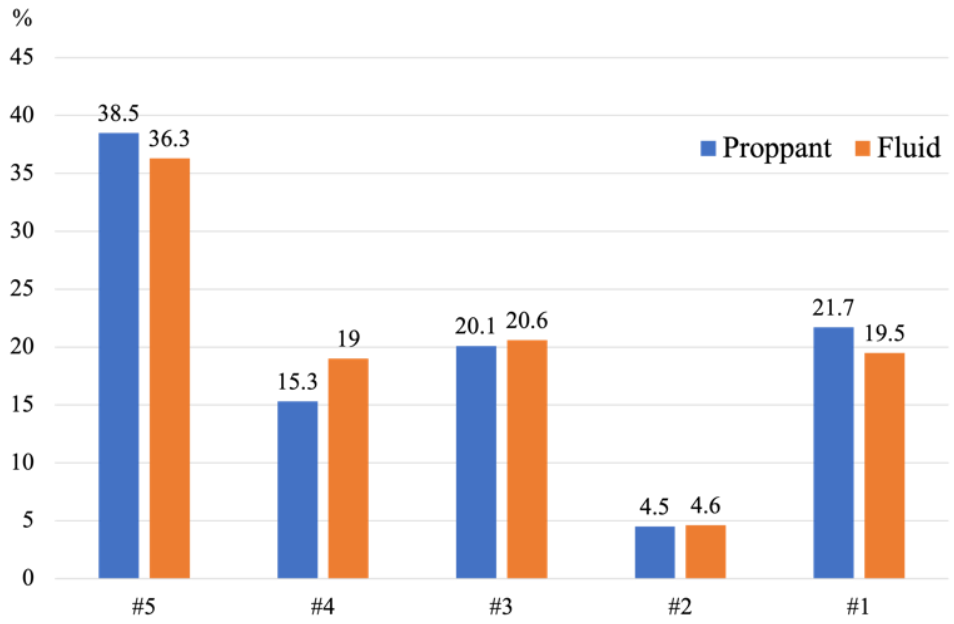

Figure 6.5. Proppant and fluid allocation in each perforation cluster (#1 – #5).

Figure 6.4 shows the processed near-wellbore DAS measured from a single stage of Well A. This stage was completed with five perforated intervals represented by red triangles. The acoustic energy level (Molenaar & Cox, 2013) is displayed across a high frequency range of 200-2000 Hz, with red denoting high and blue representing low power. A diversion technique is employed at the red dash line in order to ensure a uniform distribution of treatment fluid across the targeted intervals (Bybee, 2010). However, in this example, the effect is not readily apparent.

The perforation clusters were completed using slickwater with a low concentration of proppant. The allocation of proppant and fluid placed in each perforation cluster (PC) is shown in **Figure 6.5**. In this stage, the #5 perforation cluster has the highest proppant and fluid distribution, making it the dominant fracture. As shown in **Figure 6.4**, the energy signal generated by PC #5 is the longest and stronges. In contrast, PC #1 and 3 have comparable proppant placement, reflected in their energy levels exhibiting similar lengths and widths, although there is a brief delay of breakdown for PC #1. For PC #4, the proportion of treatment fluid is slightly lower than PC #1

and 3 due to the shorter fracturing time. Therefore, analyzing both figures provides crucial insight into fluid placement among perforation clusters during stimulation.

6.3.4 Production Data

Production allocation, or quantitative determination of contribution from individual perforation clusters to the total well production, can be estimated using DAS, relying on the proportionality between flow rates and corresponding acoustic noise (Van der Horst et al., 2014).

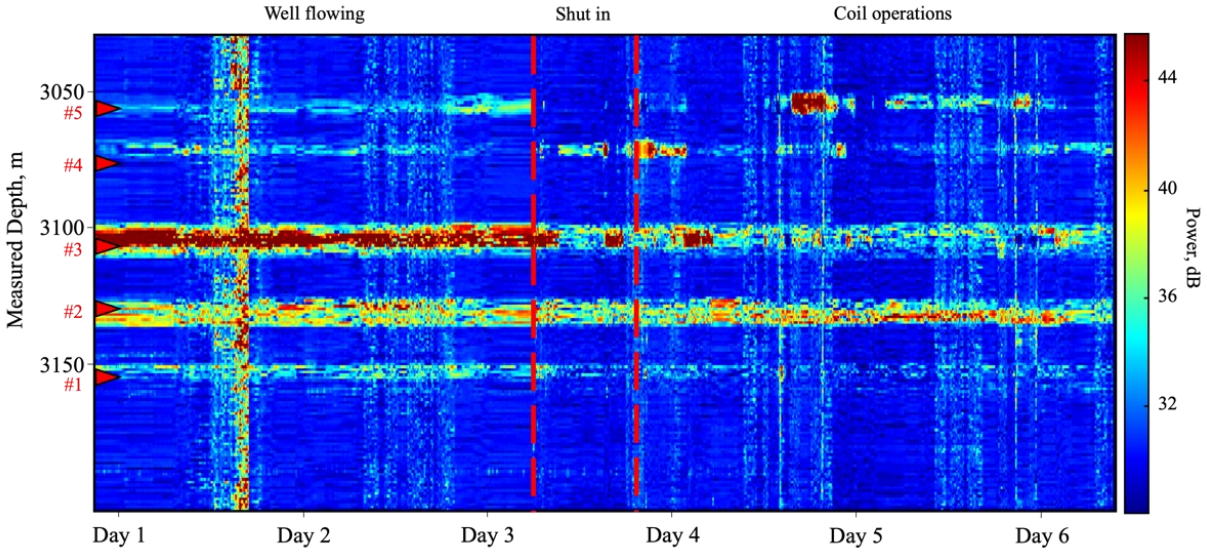

Figure 6.6. Production data recorded via DAS workflow in Well A over five days (3-10 Hz).

Figure 6.6 presents an example of the production data recorded in Well A during a 5-day period, corresponding to the same hydraulic fracturing stage as depicted in **Figure 6.4**. The production starts after the shut-in period when the bridge plug is installed. In this example, clusters #3 and #4 have stronger signal power, indicating that they make a comparatively greater contribution to production. Due to the inherent constraints in the available dataset, quantitative analysis is impeded, and only qualitative assessment is conducted.

6.4 Results and Discussion

In this section, two sensitivity analysis cases are performed. The objective is to investigate the effect of different fracture hit locations on hydraulic fracture propagation efficiency and well productivity. The DAS field data used in this section were provided by an anonymous company.

6.4.1 Effects of Cluster Spacing and Well Spacing on Fracture Length

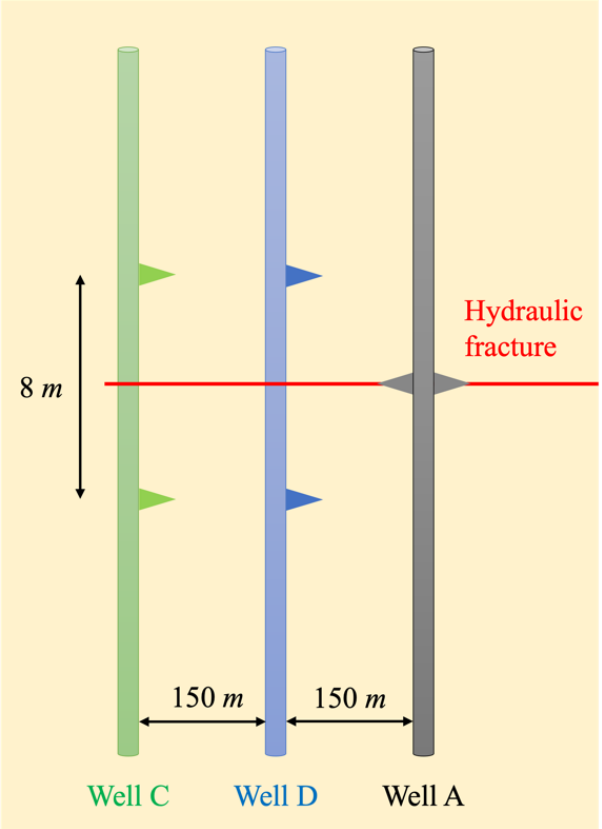

Figure 6.7. A schematic of simulation model setup.

Parameters	Value
Matrix porosity, ϕ_M	0.06
Matrix permeability, k_M	2×10^{-17} m^2 (Vaisblat et al., 2022)
Young's modulus, E	38.6 GPa
Poisson's ratio, v	0.22

Biot's coefficient, b	0.75
Initial reservoir pressure, P_{Mi}	30 MPa
Maximum horizontal stress, S_{Hmax}	45 MPa
Minimum horizontal stress, S_{Hmin}	40 MPa
Injection rate, Q_i	0.1 m^2/s
Viscosity, μ	0.005 Pa s

Table 6.1. Parameters used in the sensitivity analysis case.

The schematic of the model setup is presented in **Figure 6.7**, along with the associated completion parameters and geomechanical properties listed in **Table 6.1**. Wells A and D are selected for the cluster spacing sensitivity analysis. The perforation clusters of Well D are oriented towards Well A; therefore, the injection rate via PCs of Well D is set to half of the total flow rate $Q_i/2$, as only half of the production area is simulated. The hydraulic fracture from Well A can propagate in both directions. Two cases are simulated: (1) A single fracture in Well D as a control group (similar to the scenario with large cluster spacing); (2) cluster spacing = 4 m in Well D.

For the well spacing sensitivity analysis, the effect of fracture hit from a nearby well at varying distances is simulated. For the case of well spacing = 150 m, the impacts of Well D on fracture half-length at Well A are considered. For the case of well spacing = 300, the impacts of Well C on fracture half-length at Well A are shown.

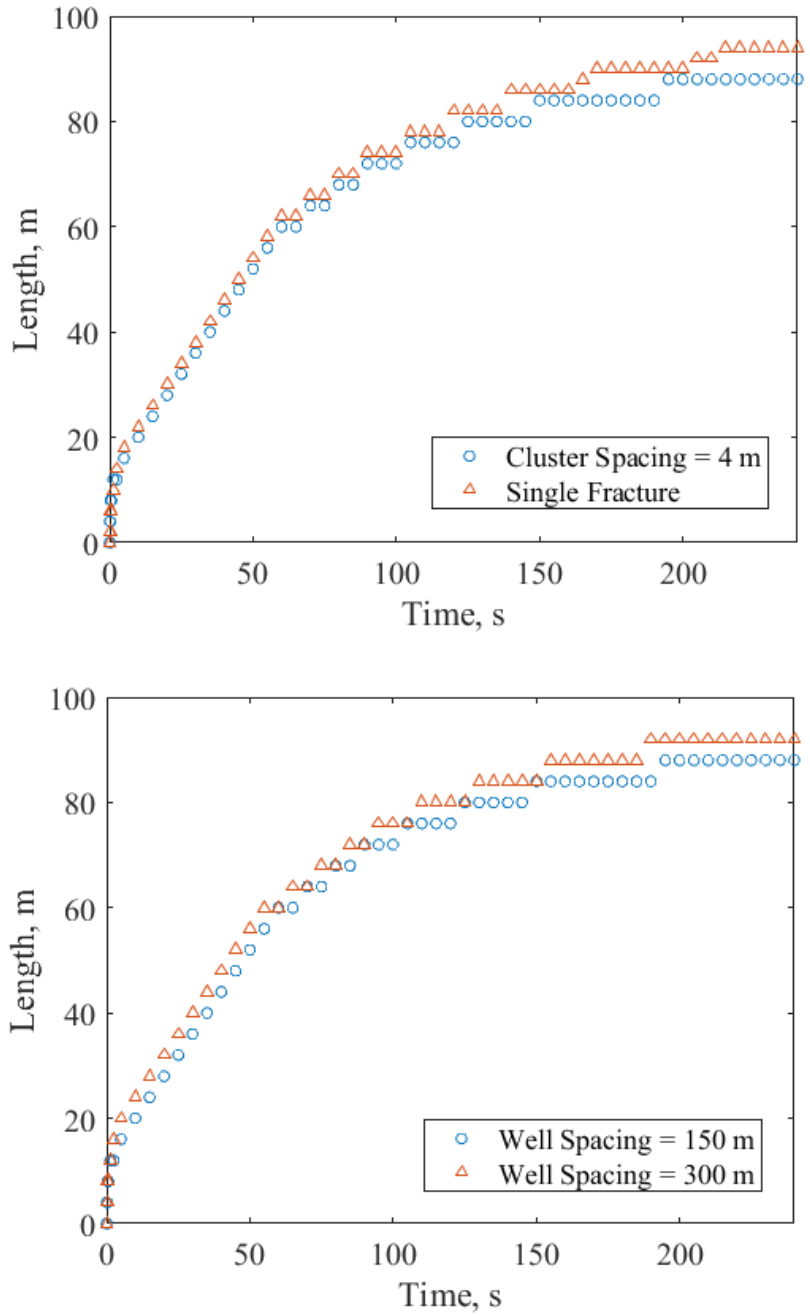

Figure 6.8. Comparison of fracture half-length vs. injection time at Well A for different: (top) cluster spacing and (bottom) well spacing.

Figure 6.8 compares fracture half-length as a function of injection time for the cluster and well spacing cases. The hydraulic fracturing treatment from well D lasted 10 minutes, followed by the injection from well A. The top plot in **Figure 6.8** illustrates that the left half-length of the

hydraulic fracture from well A is affected by the shadowing effects from the offset 'well's hydraulic fracturing treatment and is shorter compared to the single-fracture case unaffected by adjacent wells. When comparing different well spacing, the hydraulic fracturing treatment from well C lasted for 20 minutes, but the lack of stress shadowing shows that larger well spacing has less impact on the fracture growth from well A.

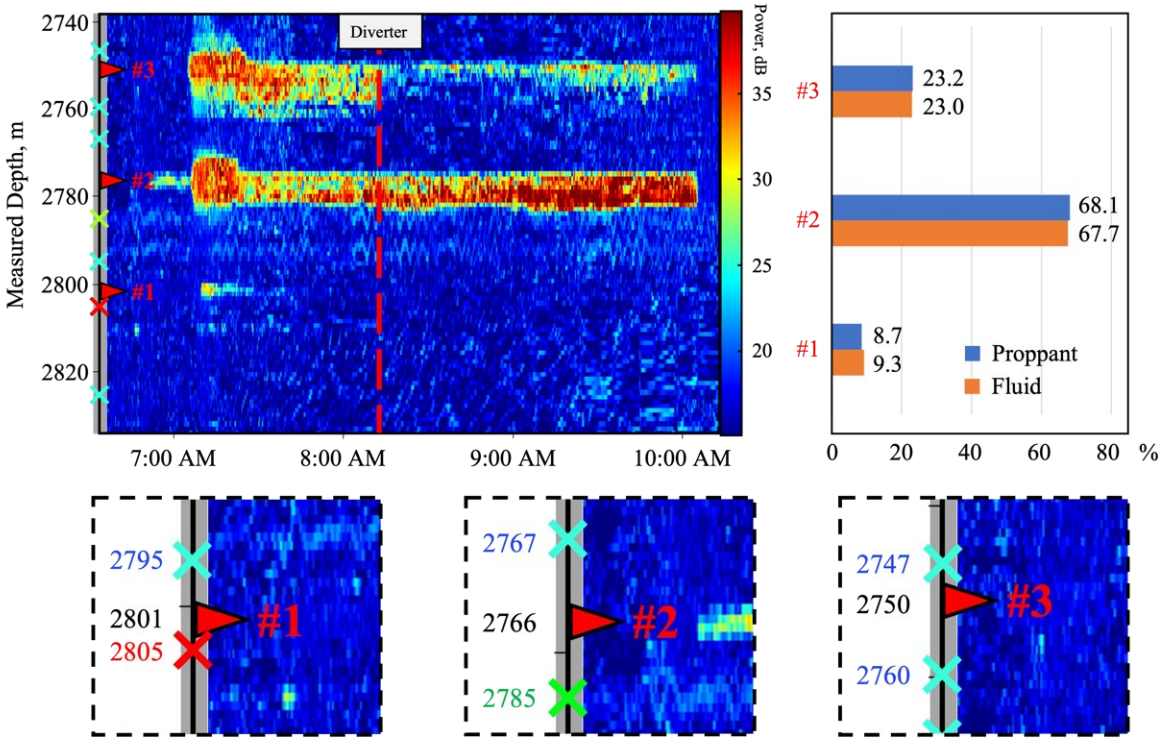

Figure 6.9. Left top: HF-NW-DAS data observed during the treatment of well A; Right top: proppant and fluid allocation, x = percentage, y = perforation number; Bottom row: Enlarged views of the relative position of perforations and fracture hits, red, green, and blue crosses indicate the MD of the fracture hit from well B, C, and D, respectively.

To further verify our results from the numerical simulations, it is advisable to re-organize the data set and provide a more comprehensive representation of the NW DAS field data. Applying the methodology presented in **Section 6.3.2**, the fracture hit locations from each well can be identified and marked on the y-axis of the NW DAS data. This allows for a clear visualization of the relative spatial relationship between the fracture hits and the perforation clusters, as

demonstrated in **Figure 6.9**. The red, green, and blue crosses indicate the fracture hits from well B, C, and D, respectively. In this stage, three perforation clusters are performed, and there is at least one fracture hit on either side of each cluster.

By comparing the results of DAS data intensity, treatment fluid allocation, and the MD of the fracture hits in **Figure 6.9**, it is observed that the red strip corresponding to PC #2 exhibits the greatest length. Additionally, the fluid allocation for this PC is the highest. It indicates that the duration of the hydraulic fracturing from PC #2 is the longest, and the hydraulic fracture from this PC has the greatest extent. Because the fracture hits surrounding PC #2 are located furthest from the perforation cluster compared to those from PC #1 and #3. Additionally, one of the fracture hits is from Well C, which is even further away from the monitoring well, making the stress shadowing effect even less and more treatment fluid flows into PC #2. This observation corroborates our simulation results, indicating that fracture hits closer to the perforation cluster and smaller well spacing results in larger stress shadowing effects that inhibit hydraulic fracture propagation from the post-process wells.

6.4.2 Effects on Production

The same model setup was used to investigate the effects on fluid productivity. **Figure 6.10** compares the effects of different cluster spacing and well spacing on cumulative production. In the case of a single fracture, the cumulative production initially increases and then stabilizes after about 350 seconds. On the other hand, in the case of cluster spacing, the fracture grows much faster and continues to grow for ten minutes, resulting in higher cumulative production.

When the offset well is located further away from well A, the cumulative production gradually increases and eventually achieves stability after 500 seconds, resembling the single

fracture case but having a longer growth period. Also, the production, in this case, is lower than the 150-meter well spacing case. Therefore, fracture hits from a closer offset well, and smaller cluster spacing positively impacts well productivity.

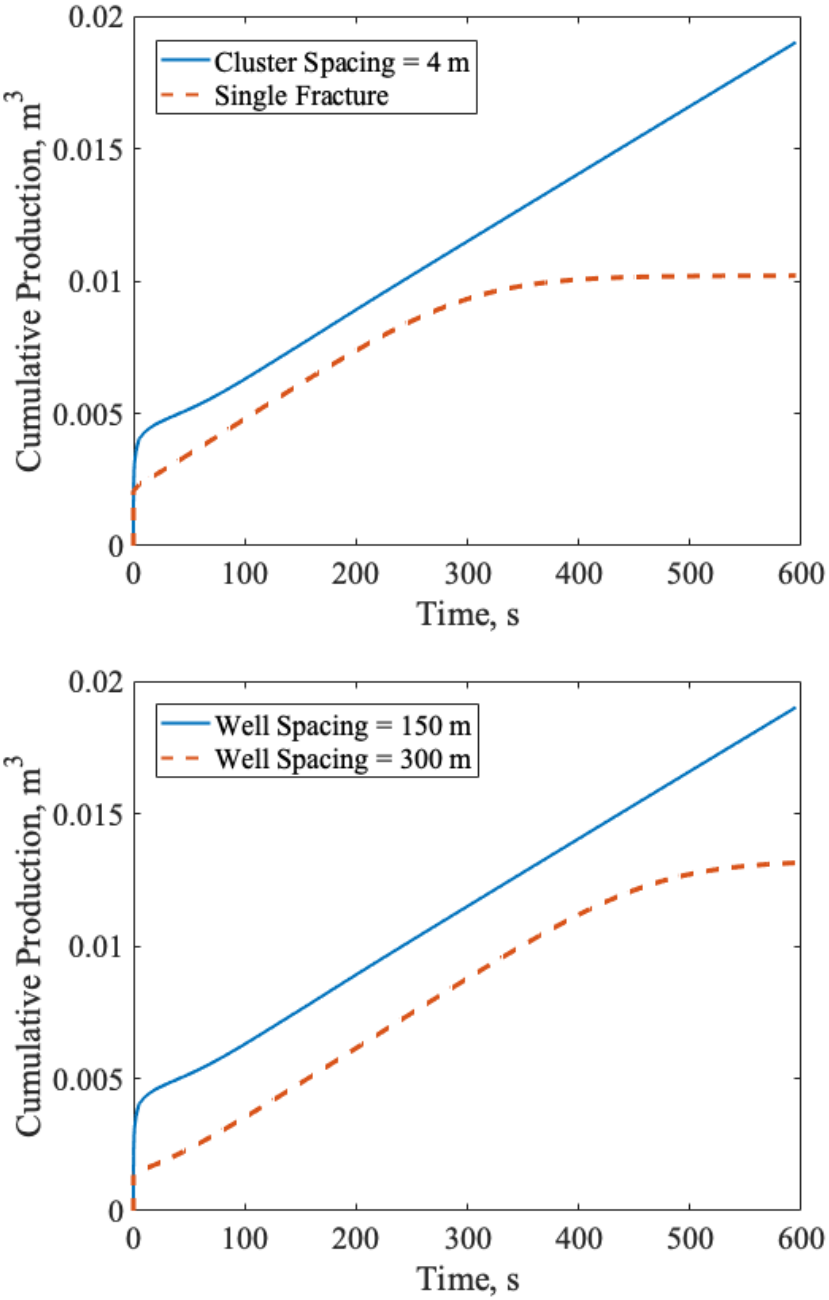

Figure 6.10. Comparison of cumulative production vs. injection time for different (top) cluster spacing and (bottom) well spacing.

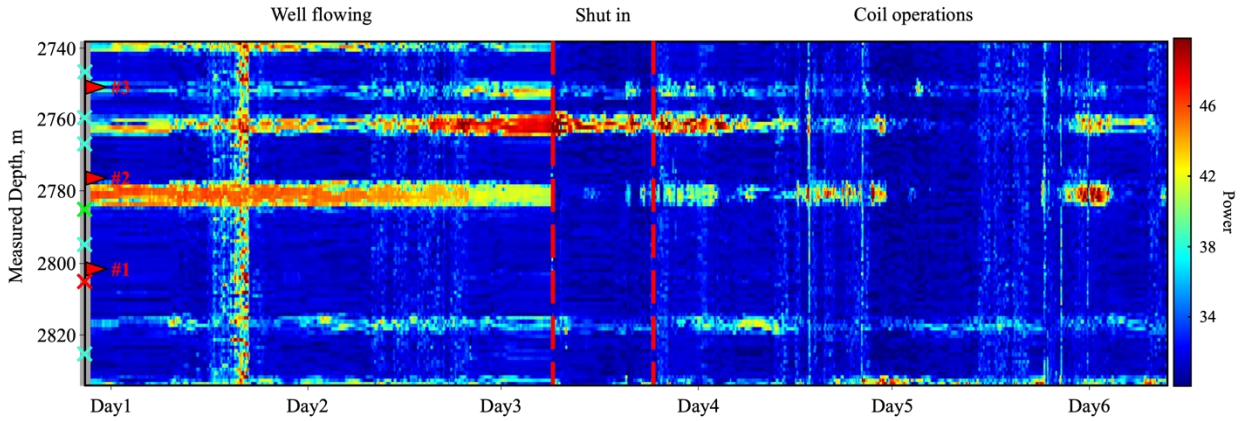

Figure 6.11. HF-NW-DAS (3-10 Hz) recorded at the same stage as the last section in Well A.

The production data recorded at the same stage as **Figure 6.9** in Well A is presented in **Figure 6.11**, along with the location markers of fracture hits. The data covers a period of 6 days, with the second half showing the start of production. It can be observed that the production signal in PC #3 is longer and more sustained, while the signal in PC #2 is discontinuous. This observation matches our simulation results, as fracture hits near PC #3 are closer and create a highly stimulated area that enhances productivity. Therefore, it illustrates that the fracture hit within the range of this stage positively impacts production. During the typical infill drilling process, when fracture hits occur, the high-pressure fluid and proppants in the hydraulic fracture come into contact with the parent wellbore. This process risks introducing sand into the parent wellbore (Pankaj, 2018) and combining the existing pressure depletion area around the wellbore, resulting in a potential production decline (Ajani & Kelkar, 2012). Hence, this scenario would be considered a "negative" fracture hit from a production perspective. However, in this case, the producer (i.e. Well A) began its treatment last and conducted production after all the hydraulic fracturing treatments were completed. This sequence prevented the risk of sand being pumped into the wellbore. Thus, fracture hits increase the drainage area and consequently have a "positive" impact on the production of Well A (Cipolla et al., 2018).

No production signal can be observed in PC #1. This may be attributed to the fact that the hydraulic fracture generated here was short and not sufficiently stimulated, according to **Figure 6.9**. It is possible that despite the presence of fracture hits around PC #1, the hydraulic fracture was not long enough to provide sufficient conductivity for fluid flow.

6.4.3 The Impact of Stress Shadowing on Hydraulic Fracture Growth in Later Stages

In this case, the *in-situ* geomechanical parameters remain the same as those presented in **Section 6.4.1**, except for using a single injector with seven perforation clusters. The spacing between each PC is 8 meters, with PC #1 on the rightmost end, near the toe of the wellbore, and PC #7 at the heel. The injection process starts at PC #1, and after 10 minutes, the injection at PC #1 ceases, and injection at PC #2 begins, continuing in this manner. This is intended to simulate the process of multi-stage hydraulic fracturing where each stage is separated by a frac plug or other isolation device, and fracture stimulation is performed stage by stage.

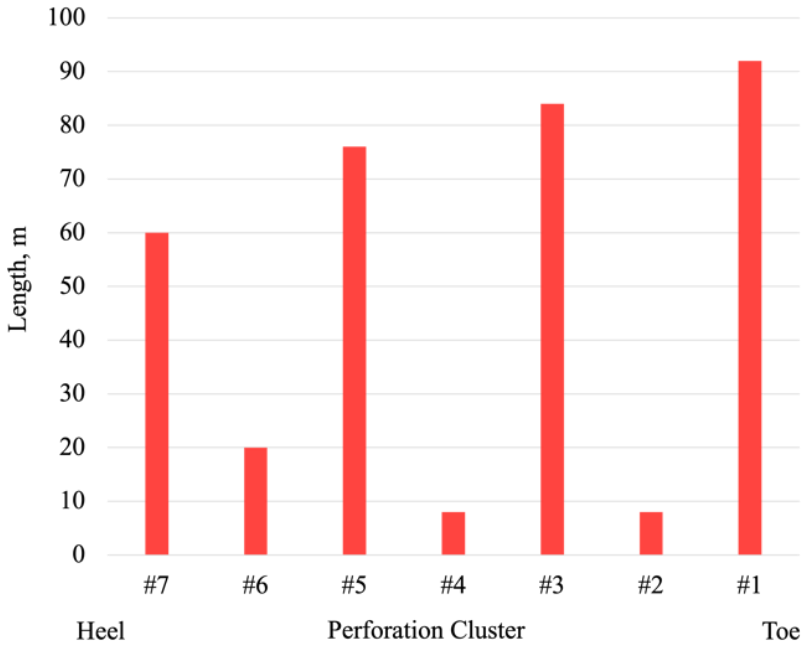

(a) Fracture half-length variation across PCs

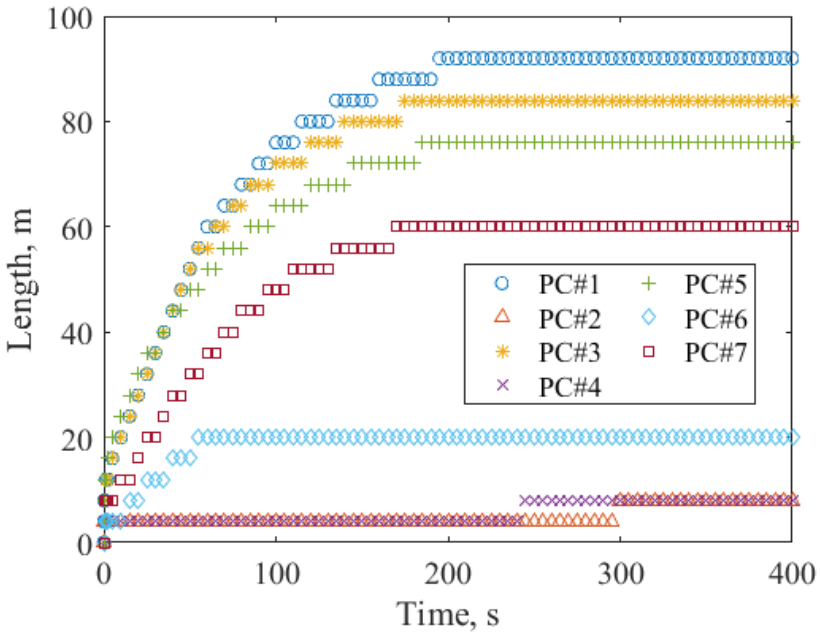

(b) Fracture half-length variation vs. time

Figure 6.12. Variation of fracture half-length (a) at perforation clusters after 10 minutes of injection for each PC and (b) over time.

Figure 6.12 shows the variation of fracture half-length cross perforation clusters after 10 minutes of injection and fracture half-length changes over time for each PC. In **Figure 6.12 (a)**, the treatment sequence proceeds from right to left. The fracture length at PC #1 is the longest, followed by a shorter fracture at PC #2, then a longer fracture at PC #3, and so on. Overall, the fracture length decreases from the toe to the heel of the wellbore. A similar trend can be observed in **Figure 6.12 (b)**. Furthermore, it illustrates that fracture growth is slower in the later stages and close to the heel of the well.

Consider the first three PCs (#1 – #3), the alternating long and short fractures observed in this section may be attributed to the large stress shadowing effect generated by the propagation of the first fracture, which inhibits the growth of the second fracture. Consequently, the second fracture does not create a substantial stress shadowing effect and poses minimal interference to the

third one. The third fracture is primarily influenced by the first fracture, which is further away, resulting in a minor impact on its length.

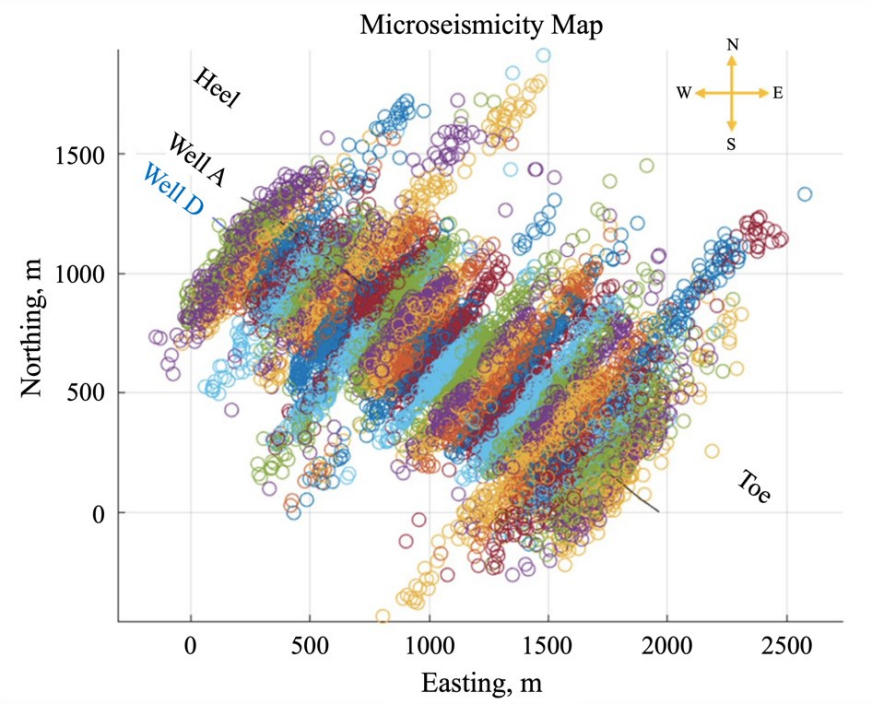

Figure 6.13. Plan view of microseismic cloud distribution across all stages. Each stage is represented with a distinct color. Modified from Ortega Perez (2022).

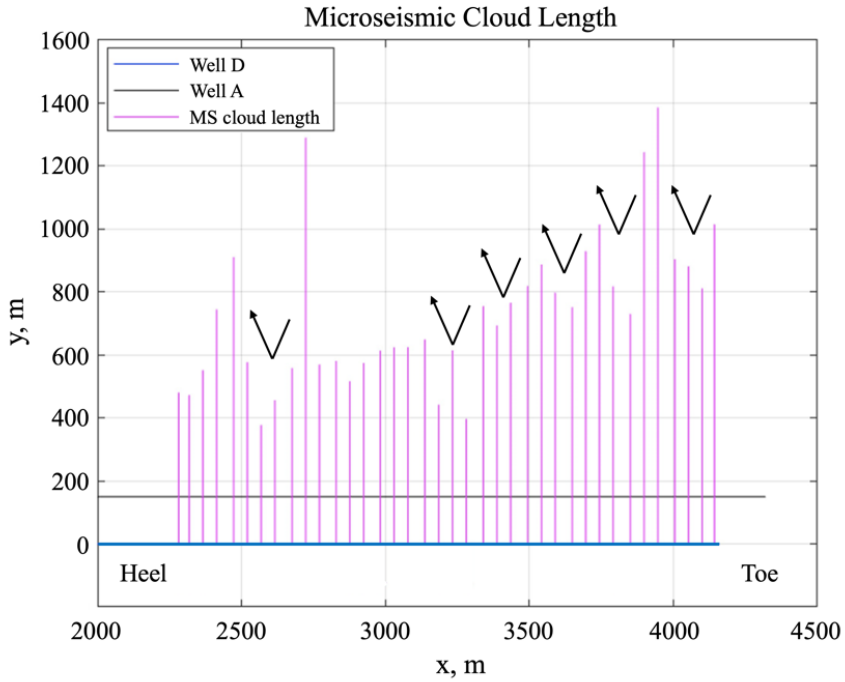

Figure 6.14. The schematic of the microseismic cloud length for each stage of well D. Black arrows indicate alternating fracture length. Modified from Ortega Perez (2022).

DAS technique is limited in accurately detecting the entire length of a hydraulic fracture, as the fiber optic sensor can only capture the moment when the fracture intersects with it and cannot monitor the fracture propagation beyond that point. In order to visualize the fracture length and study the effect on the fracture in the later stages, microseismic activity monitoring is employed. This technique provides valuable insights into the propagation and geometry of hydraulic fractures by mapping their spatial and temporal patterns (Cole et al., 2017; Le Calvez et al., 2016).

In order to approximate the fracture trajectory based on the observed microseismic events, the microseismic events were spatially mapped along the treated and monitoring wells without applying any data filters (**Figure 6.13**) in another study (Ortega Perez, 2022). Then, a linear regression analysis was conducted on the cloud plane (**Figure 6.14**), considering the spatial coordinates x and y as the fracture primarily propagates horizontally (Ortega Perez, 2022).

Figure 6.13 shows the microseismic cloud distribution across all stages of well D, representing the volumetric extent of the fracture shearing, opening, and closing. **Figure 6.14** represents a schematic of the microseismic cloud length for each stage of well D, which was obtained by projecting the MS events to a line perpendicular to the treatment well (Ortega Perez, 2022). The black arrows in the figure indicate the phenomenon of alternating fracture lengths. **Figure 6.14** demonstrates that, in general, the fracture length decreases from the toe to the heel of the wellbore. The alternating pattern of long and short fractures can also be observed, consistent with our simulation results.

CHAPTER 7 : CONCLUSIONS AND FUTURE WORK

7.1 Summary and Conclusions

The main objective of this research is to develop and implement a coupled flow and geomechanical simulation framework using the MRST software. The primary objective of this coupled model is to simulate the impact of fracture interference on stress evolution and production performance. Moreover, the model aims to interpret DAS responses and explore the impacts of cross-well fracture hits and completion designs on fracture propagation and production conductivity.

The original implementation of MRST is unable to handle the additional fracture interfaces in the DFM grid structure, preventing the coupling of flow and geomechanics in hydraulic fracturing simulation. To address this limitation, modifications were made to the MRST source code. These modifications involved creating indexes and nodes for all fracture cells that align with the adjacent matrix cells and ensuring consistency between the flow and geomechanical variables. In the flow problem, the discrete fractures are treated as lower-dimensional elements in the geometric grid but are explicitly represented as equidimensional elements in the computational domain. The unknown variables are located at the centroid of each matrix or fracture cell. In the geomechanical problem, the fractures are implicitly represented in both the geometric and computational domains, and the unknowns such as displacement and stress are located at the vertices of each matrix element. The McNamee-Gibson problem and Gu's problem are used for model validation, and the accuracy of the numerical solution is compared against the analytical solution.

The coupling model has been enhanced by incorporating a fracture propagation model, allowing for the simulation of fracture geometry and evolution during injection to interpret field DAS data and explore the impacts of cross-well fracture hits and completion designs on fracture propagation and production conductivity. The Barton-Bandis model is employed to update the fracture aperture, while the cubic law is utilized to update the fracture permeability. A pre-defined potential fracture path is established, which is represented by a sequence of inactive fracture elements with properties identical to the surrounding rock. It is assumed that fracture initiation occurs when the minimum effective stress at the fracture tip cells is less than the rock's tensile strength. The fracture propagation model is verified by comparison with KGD analytical solutions for the leak-off-viscosity, storage-viscosity and leak-off-toughness dominated regimes.

A comparison is made between the pressure distributions of the uncoupled and coupled models. It is observed that the uncoupled model exhibits a significantly larger pressure-depleted area around the hydraulic fracture compared to the coupled model. The coupled model shows slightly lower oil production, which is consistent with the closure of fractures and the reduction in pressure depletion.

A detailed sensitivity analysis is conducted to evaluate the impact of various factors, including hydraulic fracture geometry, well spacing, cluster spacing, and differential stress, on pressure depletion and stress evolution, the following conclusions can be drawn:

(1) S'_{Hmax} orientation is strongly affected by pressure depletion in the vicinity of hydraulic fractures: change in S'_{Hmax} orientation is most significant in the vicinity of hydraulic fractures.

(2) The effective principal stress distribution is affected not only by the nearby hydraulic fracture(s) within its immediate vicinity but also by its proximity to other fractures in the entire domain.

(3) If longer outer fractures surround shorter fractures, the drainage areas could be reduced dramatically due to stress shadowing effects.

(4) The well spacing and cluster spacing should be optimized. Fractures placed either too close or too far apart may negatively affect the drainage area. Analysis of inter-well interference can provide an insight into well spacing design.

(5) The results illustrate the significance of incorporating geomechanical effects in the flow simulation process – at least a 10% difference in cumulative production is observed in the case studies.

(6) Differential stress has a significant effect on stress evolution and pressure depletion. There is less change in stress orientation if the differential stress is high.

The mechanisms of fracturing fluid loss are investigated in this work, revealing that water saturation is relatively low at the intersection of hydraulic fractures and is relatively high in natural fractures. Furthermore, the flowback rate is higher at the early stage of production when hydraulic fracture intersects with a complex natural fracture network.

Some case studies are performed to investigate different fracture hit scenarios by comparing strain and strain rate waterfall plots to the field DAS signals. A sensitivity analysis of the simulated strain response is also performed. The conclusions are listed as follows:

(1) A fracture hit occurs when the heart shape ends in the DAS data or simulated strain rate waterfall plots. The strain rate waterfall plot is linear with the field DAS map.

(2) When multiple adjacent heart shapes are observed in one stage, it indicates that the hydraulic fracture is divided into multiple branches.

(3) The antenna is a red band without a heart shape, shown in the strain response maps right before the fracture hits. It can be simulated by reactivating a pre-existing fracture intersecting with the monitor well by another hydraulic fracture.

(4) If a continuous antenna signal is observed in the field DAS data, the permeability of this pre-existing fracture might be high.

(5) The spacing between the treatment well and the monitor well influences strain rate. The greater the spacing is, the more pronounced the stress shadowing effects would be on the antenna stripe.

(6) Heart shape size increases with the increasing rock permeability. The surrounding matrix is likely more permeable when the large heart shape is observed in the field DAS data.

This work aims to utilize the model to explore the effects of cross-well fracture hits, as well as various completion designs, including cluster spacing, well spacing and fracture sequencing, on fracture propagation and production conductivity at a nearby well. A combination of numerical simulation and raw DAS data analysis is employed to achieve this. The conclusions are shown as follows:

(1) Fracture hits located closer to the perforation cluster and smaller well spacing result in larger stress shadowing effects that inhibit hydraulic fracture propagation from the post-process wells.

(2) Fracture hits from a closer offset well and smaller cluster spacing can positively impact well productivity.

(3) The fracture length decreases, and fracture grows slower from the toe to the heel of the wellbore, with the length of the fracture changing alternately.

7.2 Contributions

The primary contributions are summarized as follows:

The flow problem is discretized using the Finite Volume Method (FVM), and the geomechanical discretization is based on the Virtual Element Method (VEM). To the best of the author's knowledge, although many methods for modeling hydraulic fracturing have been proposed, no such models have been implemented in the MRST framework, where flow and geomechanical computations are solved based on fixed-stress splitting in a DFM model.

The fixed-stress splitting coupled flow and geomechanical simulation model developed in MRST can simulate multi-phase flow in a domain consisting of both discrete fracture networks and the background matrix. This simulation approach can more accurately capture the dynamic behaviour of stress evolution and fracture interference, and fluid and rock properties within fractures and matrix.

This study addresses the limitations of previous research studies of fluid loss mechanisms by explicitly modeling detailed fracture geometries, arbitrarily distributed natural fractures, and fluid distribution within the fracture elements.

This study solves several research gaps that more analysis should be carried out to understand better trends and characteristics of field DAS data, particularly concerning how stress shadowing and fracture interference are observed for more complex configurations (e.g., branching fractures) and pre-existing fractures by investigating and interpreting characteristics of fracture hits from adjacent wells. Since both the matrix and fractures are discretized in the proposed

simulation model, the effect of different rock properties on the strain variation can be investigated compared to the DDM model.

This study presents several case studies to explore the effects of cross-well fracture hits and completion designs on fracture propagation and production conductivity. The simulation results reveal new insights into optimizing completion designs. The models are analyzed to test various scenarios of cross-well fracture hits and the corresponding DAS signals.

7.3 Recommendations for Future Work

Based on the limitations of this work, I provide recommendations for future work from three perspectives: (1) considering fracture direction; (2) expanding the model to a three-dimensional framework; (3) conducting quantitative analysis of the DAS data:

(1) The current model primarily focuses on planar fracture propagation along a predetermined path. However, it is important to consider the influence of stress shadowing effects from adjacent fractures on the fracture direction. Additionally, the model should incorporate the three possible scenarios that may arise at the interaction between hydraulic fractures and natural fractures. By considering these interactions, the model can provide a more accurate representation of the complex behavior observed in real-world situations.

(2) By extending the model to a 3D framework, the inclusion of surface loading and vertical stress can provide a more accurate representation of the geomechanical behavior. This expansion would allow for the investigation of additional case studies, such as scenarios involving vertical monitoring wells and fracture hits occurring at different levels, facilitating a more comprehensive characterization of the LF-DAS signature patterns.

(3) It is recommended to compare the model results with a wider range of field data, allowing for a more rigorous and quantitative assessment of the model's accuracy and predictive capabilities. A more complex natural fracture network system is also be recommended to incorporate into the simulation. By accurately representing the intricate network of natural fractures observed from DAS data or other monitoring techniques, the simulation can provide a more realistic representation of the hydraulic fracturing and production process. The simulation results can then be used to validate and calibrate the DAS measurements.

BIBLIOGRAPHY

Abe, H., Keer, L., & Mura, T. (1976). Growth rate of a penny-shaped crack in hydraulic fracturing of rocks, 2. *Journal of Geophysical Research*, *81*(35), 6292-6298.

Adachi, J., Siebrits, E., m, Peirce, A., & Desroches, J. (2007). Computer simulation of hydraulic fractures. *International Journal of Rock Mechanics and Mining Sciences*, *44*(5), 739-757.

Adachi, J. I., & Detournay, E. (2008). Plane strain propagation of a hydraulic fracture in a permeable rock. *Engineering Fracture Mechanics*, *75*(16), 4666-4694.

Ajani, A., & Kelkar, M. (2012). Interference study in shale plays. SPE Hydraulic Fracturing Technology Conference,

Andersen, O., Nilsen, H. M., & Raynaud, X. (2017). Coupled geomechanics and flow simulation on corner-point and polyhedral grids. SPE Reservoir Simulation Conference,

Baca, R., Arnett, R., & Langford, D. (1984). Modelling fluid flow in fractured-porous rock masses by finite-element techniques. *International Journal for Numerical Methods in Fluids*, *4*(4), 337-348.

Bandis, S., Lumsden, A., & Barton, N. (1983). Fundamentals of rock joint deformation. International Journal of Rock Mechanics and Mining Sciences & Geomechanics Abstracts,

Barton, N., Bandis, S., & Bakhtar, K. (1985). Strength, deformation and conductivity coupling of rock joints. International journal of rock mechanics and mining sciences & geomechanics abstracts,

Becker, M. W., Coleman, T. I., & Ciervo, C. (2020). Distributed acoustic sensing as a distributed hydraulic sensor in fractured bedrock. *Water resources research*, *56*(9), e2020WR028140.

Beirão da Veiga, L., Brezzi, F., Marini, L. D., & Russo, A. (2014). The hitchhiker's guide to the virtual element method. *Mathematical models and methods in applied sciences*, *24*(08), 1541-1573.

Bertoncello, A., Wallace, J., Blyton, C., Honarpour, M., & Kabir, C. S. (2014). Imbibition and water blockage in unconventional reservoirs: well-management implications during flowback and early production. *SPE Reservoir Evaluation & Engineering*, *17*(04), 497-506.

Bhardwaj, P., Hwang, J., Manchanda, R., & Sharma, M. M. (2016). Injection induced fracture propagation and stress reorientation in waterflooded reservoirs. SPE Annual Technical Conference and Exhibition,

Bower, A. F. (2009). *Applied mechanics of solids*. CRC press.

Bunger, A. P., Detournay, E., & Garagash, D. I. (2005). Toughness-dominated hydraulic fracture with leak-off. *International Journal of Fracture*, *134*, 175-190.

Bybee, K. (2010). Acid placement and diversion. *Journal of Petroleum Technology*, *62*(06), 53-54.

Carrier, B., & Granet, S. (2012). Numerical modeling of hydraulic fracture problem in permeable medium using cohesive zone model. *Engineering Fracture Mechanics*, *79*, 312-328.

Chang, C.-T. (1994). *Nonlinear dynamic discontinuous deformation analysis with finite element meshed block system*. University of California, Berkeley.

Chen, B., Barboza, B. R., Sun, Y., Bai, J., Thomas, H. R., Dutko, M., Cottrell, M., & Li, C. (2021). A review of hydraulic fracturing simulation. *Archives of Computational Methods in Engineering*, 1-58.

Cheng, Y. (2012). Impact of water dynamics in fractures on the performance of hydraulically fractured wells in gas-shale reservoirs. *Journal of Canadian Petroleum Technology*, *51*(02), 143-151.

Cipolla, C., Motiee, M., & Kechemir, A. (2018). Integrating microseismic, geomechanics, hydraulic fracture modeling, and reservoir simulation to characterize parent well depletion and infill well performance in the Bakken. SPE/AAPG/SEG Unconventional Resources Technology Conference,

Cipolla, C., & Wright, C. (2000). Diagnostic techniques to understand hydraulic fracturing: what? why? and how? SPE/CERI Gas Technology Symposium,

Clifton, R., & Abou-Sayed, A. (1979). On the computation of the three-dimensional geometry of hydraulic fractures. Symposium on low permeability gas reservoirs,

Clifton, R. J., & Abou-Sayed, A. S. (1981). A variational approach to the prediction of the three-dimensional geometry of hydraulic fractures. SPE/DOE low permeability gas reservoirs symposium,

Clough, R. W. (1960). The finite element in plane stress analysis. *Proc. 2^< nd> ASCE Confer. On Electric Computation, 1960*.

Cole, S., Karrenbach, M., Boone, K., Ridge, A., Kahn, D., Rich, J., Silver, K., & Langton, D. (2017). Effective diffusivity estimates from distributed fiber-optic strain and microseismic measurements. 2017 SEG International Exposition and Annual Meeting,

Coussy, O. (2004). *Poromechanics*. John Wiley & Sons.

Crouch, S. (1976). Solution of plane elasticity problems by the displacement discontinuity method. I. Infinite body solution. *International Journal for Numerical Methods in Engineering*, *10*(2), 301-343.

Cundall, P. A. (1971). A computer model for simulating progressive, large-scale movement in blocky rock system. Proceedings of the international symposium on rock mechanics,

Cundall, P. A. (1980). *UDEC-A Generalised Distinct Element Program for Modelling Jointed Rock*.

Cundall, P. A. (1988). Formulation of a three-dimensional distinct element model—Part I. A scheme to detect and represent contacts in a system composed of many polyhedral blocks. International journal of rock mechanics and mining sciences & geomechanics abstracts,

Davies, G. R., Moslow, T. F., & Sherwin, M. D. (1997). The lower Triassic Montney formation, west-central Alberta. *Bulletin of Canadian Petroleum Geology*, *45*(4), 474-505.

Detournay, E., Cheng, A.-D., & McLennan, J. (1990). A poroelastic PKN hydraulic fracture model based on an explicit moving mesh algorithm.

Fernández-Ruiz, M. R., Soto, M. A., Williams, E. F., Martin-Lopez, S., Zhan, Z., Gonzalez-Herraez, M., & Martins, H. F. (2020). Distributed acoustic sensing for seismic activity monitoring. *APL Photonics*, *5*(3), 030901.

Ferretti, E. (2020). DECM: A Discrete Element for Multiscale Modeling of Composite Materials Using the Cell Method. *Materials*, *13*(4), 880.

Fu, P., Johnson, S. M., & Carrigan, C. R. (2013). An explicitly coupled hydro-geomechanical model for simulating hydraulic fracturing in arbitrary discrete fracture networks. *International Journal for Numerical and Analytical Methods in Geomechanics*, *37*(14), 2278-2300.

Gain, A. L., Talischi, C., & Paulino, G. H. (2014). On the virtual element method for three-dimensional linear elasticity problems on arbitrary polyhedral meshes. *Computer Methods in Applied Mechanics and Engineering*, *282*, 132-160.

Garagash, D. I. (2006). Plane-strain propagation of a fluid-driven fracture during injection and shut-in: Asymptotics of large toughness. *Engineering Fracture Mechanics*, *73*(4), 456-481.

Garipov, T., Karimi-Fard, M., & Tchelepi, H. (2016). Discrete fracture model for coupled flow and geomechanics. *Computational Geosciences*, *20*, 149-160.

Geertsma, J. (1989). Two-dimensional fracture propagation models. recent advances in hydraulic fracturing. *Recent Advances in Hydraulic Fracturing*, *12*, 81-94.

Geertsma, J., & De Klerk, F. (1969). A rapid method of predicting width and extent of hydraulically induced fractures. *Journal of Petroleum Technology*, *21*(12), 1571-1581.

Geiger, S., Dentz, M., & Neuweiler, I. (2013). A novel multirate dual-porosity model for improved simulation of fractured and multiporosity reservoirs. *SPE Journal*, *18*(04), 670-684.

Ghahfarokhi, P. K., Wilson, T. H., Carr, T. R., Kumar, A., Hammack, R., & Di, H. (2019). Integrating distributed acoustic sensing, borehole 3C geophone array, and surface seismic array data to identify long-period long-duration seismic events during stimulation of a Marcellus Shale gas reservoir. *Interpretation*, *7*(1), SA1-SA10.

Giallorenzi, T. G., Bucaro, J. A., Dandridge, A., Sigel, G. H., Cole, J. H., Rashleigh, S. C., & Priest, R. G. (1982). Optical fiber sensor technology. *IEEE transactions on microwave theory and techniques*, *30*(4), 472-511.

Granet, S., Fabrie, P., Lemonnier, P., & Quintard, M. (2001). A two-phase flow simulation of a fractured reservoir using a new fissure element method. *Journal of Petroleum Science and Engineering*, *32*(1), 35-52.

Green, A., & Sneddon, I. (1950). The distribution of stress in the neighbourhood of a flat elliptical crack in an elastic solid. Mathematical Proceedings of the Cambridge Philosophical Society,

Gu, S., Liu, Y., & Chen, Z. (2014). Numerical study of dynamic fracture aperture during production of pressure-sensitive reservoirs. *International Journal of Rock Mechanics and Mining Sciences*, *70*, 229-239.

Guo, X., Wu, K., Killough, J., & Tang, J. (2019). Understanding the mechanism of interwell fracturing interference with reservoir/geomechanics/fracturing modeling in eagle ford shale. *SPE Reservoir Evaluation & Engineering*, *22*(03), 842-860.

Gupta, I., Rai, C., Devegowda, D., & Sondergeld, C. H. (2021). Fracture hits in unconventional reservoirs: A critical review. *SPE Journal*, *26*(01), 412-434.

Hartog, A. H. (2017). *An introduction to distributed optical fibre sensors*. CRC press.

Hawez, H. K., Sanaee, R., & Faisal, N. H. (2021). A critical review on coupled geomechanics and fluid flow in naturally fractured reservoirs. *Journal of natural gas science and engineering*, *95*, 104150.

Howard, G. C., & Fast, C. (1957). Optimum fluid characteristics for fracture extension. Drilling and production practice,

Hughes, T. J. (2012). *The finite element method: linear static and dynamic finite element analysis*. Courier Corporation.

[Record #138 is using a reference type undefined in this output style.]

Jiang, J., & Yang, J. (2018). Coupled fluid flow and geomechanics modeling of stress-sensitive production behavior in fractured shale gas reservoirs. *International Journal of Rock Mechanics and Mining Sciences*, *101*, 1-12.

Jin, G., & Roy, B. (2017). Hydraulic-fracture geometry characterization using low-frequency DAS signal. *The Leading Edge*, *36*(12), 975-980.

Jing, L. (2003). A review of techniques, advances and outstanding issues in numerical modelling for rock mechanics and rock engineering. *International Journal of Rock Mechanics and Mining Sciences*, *40*(3), 283-353.

Jing, L., & Hudson, J. (2002). Numerical methods in rock mechanics. *International Journal of Rock Mechanics and Mining Sciences*, *39*(4), 409-427.

Juanes, R., Samper, J., & Molinero, J. (2002). A general and efficient formulation of fractures and boundary conditions in the finite element method. *International Journal for Numerical Methods in Engineering*, *54*(12), 1751-1774.

Karaman, O. S., Kutlik, R. L., & Kluth, E. L. (1996). A field trial to test fiber optic sensors for downhole temperature and pressure measurements, West Coalinga Field, California. SPE Western Regional Meeting,

Karimi-Fard, M., Durlofsky, L. J., & Aziz, K. (2004). An efficient discrete-fracture model applicable for general-purpose reservoir simulators. *SPE Journal*, *9*(02), 227-236.

Karimi-Fard, M., & Firoozabadi, A. (2003). *Numerical Simulation of Water Injection in Fractured Media Using the Discrete Fractured Model and the Galerkin Method. SPEREE 6 (2): 117–126*.

Khan, M. S. (2010). *Investigation of discontinuous deformation analysis for application in jointed rock masses*

Khristianovic, S., & Zheltov, Y. P. (1955). Formation of vertical fractures by means of highly viscous liquid. World Petroleum Congress Proceedings,

Kim, J., Tchelepi, H. A., & Juanes, R. (2011). Stability, accuracy, and efficiency of sequential methods for coupled flow and geomechanics. *SPE Journal*, *16*(02), 249-262.

Kim, J. G., & Deo, M. D. (2000). Finite element, discrete-fracture model for multiphase flow in porous media. *AIChE Journal*, *46*(6), 1120-1130.

Klemetsdal, Ø., Berge, R., Lie, K.-A., Nilsen, H., & Møyner, O. (2017). Unstructured gridding and consistent discretizations for reservoirs with faults and complex wells. SPE Reservoir Simulation Conference,

Kurtoglu, B., & Salman, A. (2015). How to utilize hydraulic fracture interference to improve unconventional development. Abu Dhabi International Petroleum Exhibition and Conference,

Le Calvez, J., Malpani, R., Xu, J., Stokes, J., & Williams, M. (2016). Hydraulic fracturing insights from microseismic monitoring. *Oilfield Review*, *28*(2), 16-33.

Lei, Q., Latham, J.-P., & Tsang, C.-F. (2017). The use of discrete fracture networks for modelling coupled geomechanical and hydrological behaviour of fractured rocks. *Computers and Geotechnics*, *85*, 151-176.

Li, S., & Zhang, D. (2018). A fully coupled model for hydraulic-fracture growth during multiwell-fracturing treatments: enhancing fracture complexity. *SPE Production & Operations*, *33*(02), 235-250.

Li, X., Zhang, J., Grubert, M., Laing, C., Chavarria, A., Cole, S., & Oukaci, Y. (2020). Distributed acoustic and temperature sensing applications for hydraulic fracture diagnostics. SPE Hydraulic Fracturing Technology Conference and Exhibition,

Lie, K.-A. (2019). *An introduction to reservoir simulation using MATLAB/GNU Octave: User guide for the MATLAB Reservoir Simulation Toolbox (MRST)*. Cambridge University Press.

Lin, R., Ren, L., & Zhao, J. (2018). Cluster spacing optimization for horizontal-well fracturing in shale gas reservoirs: modeling and field application. SPE Europec featured at 80th EAGE Conference and Exhibition,

Lindsay, G., Miller, G., Xu, T., Shan, D., & Baihly, J. (2018). Production performance of infill horizontal wells vs. pre-existing wells in the major US unconventional basins. SPE hydraulic fracturing technology conference and exhibition,

Lisjak, A., & Grasselli, G. (2014). A review of discrete modeling techniques for fracturing processes in discontinuous rock masses. *Journal of Rock Mechanics and Geotechnical Engineering*, *6*(4), 301-314.

Liu, L., Huang, Z., Yao, J., Lei, Q., Di, Y., Wu, Y.-S., Zhang, K., & Cui, S. (2021). Simulating two-phase flow and geomechanical deformation in fractured karst reservoirs based on a coupled hydro-mechanical model. *International Journal of Rock Mechanics and Mining Sciences*, *137*, 104543.

Liu, Y., Liu, L., Leung, J. Y., & Moridis, G. J. (2020). Sequentially coupled flow and geomechanical simulation with a discrete fracture model for analyzing fracturing fluid recovery and distribution in fractured ultra-low permeability gas reservoirs. *Journal of Petroleum Science and Engineering*, *189*, 107042.

Liu, Y., Wu, K., Jin, G., & Moridis, G. (2020). Rock deformation and strain-rate characterization during hydraulic fracturing treatments: insights for interpretation of low-frequency distributed acoustic-sensing signals. *SPE Journal*, *25*(05), 2251-2264.

Liu, Y., Wu, K., Jin, G., Moridis, G., Kerr, E., Scofield, R., & Johnson, A. (2021). Fracture-hit detection using LF-DAS signals measured during multifracture propagation in unconventional reservoirs. *SPE Reservoir Evaluation & Engineering*, *24*(03), 523-535.

Mahmoud, A., Gowida, A., Aljawad, M. S., Al-Ramadan, M., & Ibrahim, A. F. (2021). Advancement of hydraulic fracture diagnostics in unconventional formations. *Geofluids*, *2021*.

Manchanda, R., Bhardwaj, P., Hwang, J., & Sharma, M. M. (2018). Parent-child fracture interference: explanation and mitigation of child well underperformance. SPE Hydraulic Fracturing Technology Conference and Exhibition,

McNamee, J., & Gibson, R. (1960a). Displacement functions and linear transforms applied to diffusion through porous elastic media. *The Quarterly Journal of Mechanics and Applied Mathematics*, *13*(1), 98-111.

McNAMEE, J., & Gibson, R. (1960b). Plane strain and axially symmetric problems of the consolidation of a semi-infinite clay stratum. *The Quarterly Journal of Mechanics and Applied Mathematics*, *13*(2), 210-227.

Mengolini, M., Benedetto, M. F., & Aragón, A. M. (2019). An engineering perspective to the virtual element method and its interplay with the standard finite element method. *Computer Methods in Applied Mechanics and Engineering*, *350*, 995-1023.

Molenaar, M. M., & Cox, B. E. (2013). Field cases of hydraulic fracture stimulation diagnostics using fiber optic distributed acoustic sensing (DAS) measurements and Analyses. SPE unconventional gas conference and exhibition,

Molenaar, M. M., Hill, D. J., Webster, P., Fidan, E., & Birch, B. (2012). First downhole application of distributed acoustic sensing for hydraulic-fracturing monitoring and diagnostics. *SPE Drilling & Completion*, *27*(01), 32-38.

Monteagudo, J., & Firoozabadi, A. (2004). Control-volume method for numerical simulation of two-phase immiscible flow in two-and three-dimensional discrete-fractured media. *Water resources research*, *40*(7).

Moradi, M., Shamloo, A., & Dezfuli, A. D. (2017). A sequential implicit discrete fracture model for three-dimensional coupled flow-geomechanics problems in naturally fractured porous media. *Journal of Petroleum Science and Engineering*, *150*, 312-322.

Muanenda, Y. (2018). Recent advances in distributed acoustic sensing based on phase-sensitive optical time domain reflectometry. *Journal of Sensors*, *2018*.

Nilsen, H. M., Nordbotten, J., & Raynaud, X. (2018). Comparison between cell-centered and nodal-based discretization schemes for linear elasticity. *Computational Geosciences*, *22*, 233-260.

Noorishad, J., & Mehran, M. (1982). An upstream finite element method for solution of transient transport equation in fractured porous media. *Water resources research*, *18*(3), 588-596.

Nordgren, R. (1972). Propagation of a vertical hydraulic fracture. *Society of Petroleum Engineers Journal*, *12*(04), 306-314.

Ortega Perez, A. K. (2022). Hydraulic fracture monitoring: Integrated analysis of DAS, pumping information, microseismicity and PKN modelling.

Pankaj, P. (2018). Decoding positives or negatives of fracture-hits: a geomechanical investigation of fracture-hits and its implications for well productivity and integrity. Unconventional Resources Technology Conference, Houston, Texas, 23-25 July 2018,

Perkins, T., & Kern, L. R. (1961). Widths of hydraulic fractures. *Journal of Petroleum Technology*, *13*(09), 937-949.

Richards, J., Bartlett, R., Onen, D., Crowther, G., Molenaar, M., Reynolds, A., Wyker, B., Den Boer, H., & Berlang, W. (2015). Cloud-Based Solution for Permanent Fiber-Optic DAS Flow Monitoring. SPE Digital Energy Conference and Exhibition,

Roussel, N. P., Florez, H. A., & Rodriguez, A. A. (2013). Hydraulic fracture propagation from infill horizontal wells. SPE annual technical conference and exhibition,

Samier, P., & De Gennaro, S. (2007). Practical iterative coupling of GeoMechanics with reservoir simulation. SPE Reservoir Simulation Symposium,

Sandve, T. H., Berre, I., & Nordbotten, J. M. (2012). An efficient multi-point flux approximation method for discrete fracture–matrix simulations. *Journal of Computational Physics*, *231*(9), 3784-3800.

Seth, P., Kumar, A., Manchanda, R., Shrivastava, K., & Sharma, M. M. (2018). Hydraulic Fracture Closure in a Poroelastic Medium and its Implications on Productivity. 52nd US Rock Mechanics/Geomechanics Symposium,

Settari, A., Sullivan, R., Walters, D., & Wawrzynek, P. (2002). 3D analysis and prediction of microseismicity in fracturing by coupled geomechanical modeling. SPE gas technology symposium,

Shahri, M., Tucker, A., Rice, C., Lathrop, Z., Ratcliff, D., McClure, M., & Fowler, G. (2021). High fidelity fibre-optic observations and resultant fracture modeling in support of planarity. SPE Hydraulic Fracturing Technology Conference and Exhibition,

Shi, G. (1988). Discontinuous deformation analysis: a new numerical model for the statics and dynamics of block systems (Doctoral dissertation, University of California, Berkeley).

Shojaei, A., Galvanetto, U., Rabczuk, T., Jenabi, A., & Zaccariotto, M. (2019). A generalized finite difference method based on the Peridynamic differential operator for the solution of

problems in bounded and unbounded domains. *Computer Methods in Applied Mechanics and Engineering*, *343*, 100-126.

Shrivastava, K., & Sharma, M. M. (2018). Mechanisms for the formation of complex fracture networks in naturally fractured rocks. SPE Hydraulic Fracturing Technology Conference and Exhibition,

Shyu, K. (1993). *Nodal-based discontinuous deformation analysis*. University of California, Berkeley.

Sierra, J., Kaura, J., Gualtieri, D., Glasbergen, G., Sarker, D., & Johnson, D. (2008). DTS monitoring of hydraulic fracturing: Experiences and lessons learned. SPE Annual Technical Conference and Exhibition,

Simonson, E., Abou-Sayed, A., & Clifton, R. (1978). Containment of massive hydraulic fractures. *Society of Petroleum Engineers Journal*, *18*(01), 27-32.

Sneddon, I. N. (1946). The distribution of stress in the neighbourhood of a crack in an elastic solid. *Proceedings of the Royal Society of London. Series A. Mathematical and Physical Sciences*, *187*(1009), 229-260.

Sneddon, I. N., & Lowengrub, M. (1969). Crack problems in the classical theory of elasticity. *1969, 221 P*.

Tan, Y., Wang, S., Rijken, P., Hughes, K., Lim Chen Ning, I., Zhang, Z., & Fang, Z. (2020). Geomechanical Template for DAS Fiber Strain Patterns During Hydraulic Fracturing. SPE Annual Technical Conference and Exhibition,

Ugueto C, G. A., Huckabee, P. T., Molenaar, M. M., Wyker, B., & Somanchi, K. (2016). Perforation cluster efficiency of cemented plug and perf limited entry completions; Insights from fiber optics diagnostics. Spe hydraulic fracturing technology conference,

Ugueto C, G. A., Wojtaszek, M., Huckabee, P. T., Reynolds, A., Brewer, J., & Acosta, L. (2018). Accelerated stimulation optimization via permanent and continuous production monitoring using fiber optics. SPE/AAPG/SEG Unconventional Resources Technology Conference,

Ugueto, G. A., Todea, F., Daredia, T., Wojtaszek, M., Huckabee, P. T., Reynolds, A., Laing, C., & Chavarria, J. A. (2019). Can you feel the strain? DAS strain fronts for fracture geometry in the BC Montney, Groundbirch. SPE Annual Technical Conference and Exhibition,

Vaisblat, N., Harris, N. B., Ayranci, K., Chalaturnyk, R., Power, M., Twemlow, C., & Minion, N. (2022). Petrophysical properties of a siltstone reservoir-An example from the Montney Formation, western Canada. *Marine and Petroleum Geology*, *136*, 105431.

Valkó, P., & Economides, M. J. (1995). *Hydraulic fracture mechanics* (Vol. 28). Wiley Chichester.

Van der Horst, J., Den Boer, H., In't Panhuis, P., Wyker, B., Kusters, R., Mustafina, D., Groen, L., Bulushi, N., Mjeni, R., & Awan, K. F. (2014). Fibre optic sensing for improved Wellbore production surveillance. International Petroleum Technology Conference,

Vishkai, M., Wang, J., Wong, R. C., Clarkson, C. R., & Gates, I. D. (2017). Modeling geomechanical properties in the montney formation, Alberta, Canada. *International Journal of Rock Mechanics and Mining Sciences*, *96*, 94-105.

Wang, M., & Leung, J. Y. (2015). Numerical investigation of fluid-loss mechanisms during hydraulic fracturing flow-back operations in tight reservoirs. *Journal of Petroleum Science and Engineering*, *133*, 85-102.

Wang, S., & Chen, S. (2019). Insights to fracture stimulation design in unconventional reservoirs based on machine learning modeling. *Journal of Petroleum Science and Engineering*, *174*, 682-695.

Warpinski, N. R. (1996). Hydraulic fracture diagnostics. *Journal of Petroleum Technology*, *48*(10), 907-910.

Warpinski, N. R., Moschovidis, Z., Parker, C., & Abou-Sayed, I. (1994). Comparison study of hydraulic fracturing models—test case: GRI staged field experiment no. 3. *SPE Production & Facilities*, *9*(01), 7-16.

Warren, J., & Root, P. J. (1963). The behavior of naturally fractured reservoirs. *Society of Petroleum Engineers Journal*, *3*(03), 245-255.

Webster, P., Cox, B., & Molenaar, M. (2013). Developments in diagnostic tools for hydraulic fracture geometry analysis. SPE/AAPG/SEG Unconventional Resources Technology Conference,

Wu, K. (2014). *Numerical modeling of complex hydraulic fracture development in unconventional reservoirs*

Wu, K., & Olson, J. E. (2015a). A simplified three-dimensional displacement discontinuity method for multiple fracture simulations. *International Journal of Fracture*, *193*(2), 191-204.

Wu, K., & Olson, J. E. (2015b). Simultaneous multifracture treatments: fully coupled fluid flow and fracture mechanics for horizontal wells. *SPE Journal*, *20*(02), 337-346.

Wu, K., Wu, B., & Yu, W. (2018). Mechanism analysis of well interference in unconventional reservoirs: Insights from fracture-geometry simulation between two horizontal wells. *SPE Production & Operations*, *33*(01), 12-20.

Wu, Y., Richter, P., Hull, R., & Farhadiroushan, M. (2020). Hydraulic frac-hit corridor (FHC) monitoring and analysis with high-resolution distributed acoustic sensing (DAS) and far-field strain (FFS) measurements. *First break*, *38*(6), 65-70.

Zhang, Z., Fang, Z., Stefani, J., DiSiena, J., Bevc, D., Lim Chen Ning, I., Hughes, K., & Tan, Y. (2020). Modeling of fiber-optic strain responses to hydraulic fracturing. *Geophysics*, *85*(6), A45-A50.

Zhong, C., & Leung, J. Y. (2020). Numerical investigation of water retention in secondary fractures and apparent permeability modeling in shale gas production. *Journal of Petroleum Science and Engineering*, *192*, 107294.

Zienkiewicz, O. C., & Morice, P. (1971). *The finite element method in engineering science* (Vol. 1977). McGraw-hill London.

Appendix A

The appendix provides the function code for flow calculation, which is modified from the 'equationsOilWaterMech' within the 'ad-mechanics' module in the MRST package. To enhance the fracture model, the Barton-bandis model has been incorporated into the souce code to account for fracture deformation, aperture changes and permeability variations. Additionally, the DFM model has been integrated to create connectivity mapping for intersecting fracture grids. Porosity updates has also been implemented in this code to ensure accurate representations of the fluid flow behaviour.

```
function [eqs, names, types, state] = equationsOilWaterMech(p0, sW0, state0,
p, sW, wellVars, state, model, dt, mechTerm, drivingForces, varargin)
%
%
% SYNOPSIS:
%   function [eqs, names, types, state] = equationsOilWaterMech(p0, sW0,
state0, p, sW, wellVars, state, model, dt, mechTerm, drivingForces, varargin)
%
% DESCRIPTION:
%
% PARAMETERS:
%   p0            - pressure   (for previous time step)
%   sW0           - saturation (for previous time step)
%   state0        - state      (for previous time step)
%   p             - pressure
%   sW            - saturation
%   wellVars      - well variables
%   state         - current state
%   model         - model class instance that is used
%   dt            - time step size
%   mechTerm      - mechanical input which will enter the computation of the
%                   effective porosity
%   drivingForces - structure that gathers the well parameters and boundary
conditions.
%   varargin      -
%
% RETURNS:
%   eqs   - The residual values as ADI variables (that is with the Jacobian)
%           if the inputs were also ADI.
%   names - The name of each equations
%   types - The type of each equations
```

```
%   state - Some field related to well control of the state variables may be
updated.
%
%
%
%
% PARAMETERS:
%   p             - Pressure
%   sW            - Saturation
%   wellVars      - Well variables
%   state         - State at given time step
%   p0            - Pressure (for previous time step)
%   sW0           - Saturation (for previous time step)
%   state0        - State at given time step (for previous time step)
%   model         - Model class instance that is used.
%   dt            - Time step
%   mechTerm      - Mechanical input which will enter the computation of the
%                   effective porosity
%   drivingForces - Structure that gathers the well parameters and boundary
conditions.
%
% RETURNS:
%   eqs   - The residual values as ADI variables (that is with the Jacobian)
%           if the inputs were also ADI.
%   names - The name of each equations
%   types - The type of each equations
%   state - Some field related to well control of the state variables may be
updated.
%


% Equation for oil water system that also takes input from mechanics.


    % Note that state is given only for output
    opt = struct('iteration', -1, ...
                 'resOnly', false); % just to avoid warning
    opt = merge_options(opt, varargin{:});

    W = drivingForces.W;

    mstate = drivingForces.mstate;

    load('modeloperator');
    s = Jiahui_1;
    G = model.G; % G should be updated in the ppg model
    f = model.fluid;
    rock = model.rock; % if the matrix has dynamic properties, it'll change

    % ------------------------------------------------------------------------

    % Update fracture aperture and permeability applying Barton-Bandis
    % model

    ppg_switch = ['ppg']; % Switching from static frac to dynamic fracture
```

```
% Update aperture
% Find normal stress acting on the fracture surface
stress = mstate.stress;
stressx  = stress(:, 1); % Find all stress_xx
stressy  = stress(:, 2); % Find all stress_yy
stressxy = stress(:, 3); % Find all stress_xy

% Find cells adjacent to the fracture surface
global hybridInd GT G0

switch ppg_switch
    case 'no ppg'
        actCells = hybridInd;
        oldNeighbors = GT.faces.neighbors(GT.faces.tags > 0, :);
        newNeighbors = oldNeighbors; % newNeighbors will be updated later
        oldNeighbors(oldNeighbors >= actCells(1)) = [];
        oldNeighbors = sort(oldNeighbors);

    case 'ppg'
        actCells = G.actCells;
        face_nodes = reshape(G0.faces.nodes, 2, [])';
        oldNeighbors = G0.faces.neighbors(G.actFaces, :);
        fracNodes = face_nodes(G.actFaces,:);

    otherwise
        error('Do not recognized')

end

% Calculate total stress first
clear stress
stress = drivingForces.mechModel.operators.stress*...
    (drivingForces.xd); % effective stress
% reversoir pressure from last time step (without frac)
pr0 = p0(1:length(drivingForces.mstate.stress));

griddim = drivingForces.mechModel.G.griddim;
if griddim == 3
    pI = bsxfun(@times, pr0, [1, 1, 1, 0, 0, 0]);
    nlin = 6;
else
    pI = bsxfun(@times, pr0, [1, 1, 0]);
    nlin = 3;
end
stress = reshape(stress, nlin, []);
stress = stress';
totalStress = stress - pI; % total stress

% Find pressure in the vicinity of the fracture
pfrac = p0(actCells);
% Calculate total stress
stressxf1  = totalStress(oldNeighbors(:,1),1);
stressxf2  = totalStress(oldNeighbors(:,2),1);
% Calculate normal stress
global alpha
```

```
    stressn1 = stressxf1 + alpha .* pfrac;
    stressn2 = stressxf2 + alpha .* pfrac;

    % Update aperture using Barton-Bandis model
    global Kni Dnmax aperture apertureNew E nu

    % Barton-Bandis final
    apertureNew1 = aperture -...
        Dnmax*stressn1 ./ (Kni*Dnmax + stressn1);

    apertureNew2 = aperture -...
        Dnmax*stressn2 ./ (Kni*Dnmax + stressn2);

    apertureNew = mean([apertureNew1,apertureNew2], 2);

    if length(aperture)~= length(apertureNew) && length(aperture)~=1
        aperture_act = reshape(aperture, 2, numel(aperture)/2)';
        aperture_act = mean(aperture_act, 2);
    end

    % Store cells.neighbors to G just in case
    switch ppg_switch
        case 'no ppg'
            hybridn = length(actCells);
            G.cells.neighbors = newNeighbors(1:hybridn, :);
            newNeighborsRight = ...
newNeighbors((hybridn+1):length(newNeighbors), 2);
            G.cells.neighbors = [G.cells.neighbors, newNeighborsRight];

        case 'ppg'
            hybridn = length(hybridInd);

        otherwise
            error('Do not recognized')
    end

    % Update pore volume of fracture?

    % Update fracture permeability
    global permfrac% $aperture$ is the initial aperture
    if length(aperture)~= length(apertureNew) && length(aperture)~=1
        fracperm = permfrac .* (apertureNew./aperture_act).^2;
    else
        fracperm = permfrac .* (apertureNew./aperture).^2;
    end

    rock.perm(actCells,:) = fracperm; % make sure that the orders of
                                      % 'actCells' and 'oldNeighbors'
                                      % are the same

    % ---------------------------------------------------------------------

    % Evaluate relative permeability
    sO  = 1 - sW;
```

```
    sO0 = 1 - sW0;

    [krW, krO] = model.evaluateRelPerm({sW, sO});

    % Multipliers for properties
    [pvMult, transMult, mobMult, pvMult0] = ...
    getMultipliers(model.fluid, p, p0);

    % Modifiy relperm by mobility multiplier (if any)
    krW = mobMult.*krW; krO = mobMult.*krO;

    % Compute transmissibility
    T = s.T.*transMult;

    % --------------------------------------------------------------------

    % Update transmissibilities and create the correct connectivity mapping
    % for meshes in DFM model

    GT.faces.neighbors = GT.faceNeighbors;
    GT.rock.perm = rock.perm; % Update fracture permeability
    % Compute TPFA transmissibilities
    T = computeTrans_DFM(GT,GT.rock,'hybrid',true);

    % Transmissibilites for fracture-fracture connections
    [GT,T2] = computeHybridTrans(GT,T);

    % computeTrans returns 2 half-transmissibilities for each internal face &
    % one transmissibility for each external face. Below we compute one
    % transmissibility per face.
    cf = GT.cells.faces(:,1);
    nf = GT.faces.num;
    T  = 1 ./ accumarray(cf, 1./T, [nf, 1]);

    % find the centroids of each cell in GT.cells.centroids
    neighborclm1_ctrd = GT.cells.centroids(GT.cells.neighbors(:,1),:);
    neighborclm2_ctrd = GT.cells.centroids(GT.cells.neighbors(:,2),:);

    % create a new matrix listing the centroids of 'frac-frac' faces (x,y)
    frac2frac_ctrd(:,1) = (neighborclm1_ctrd(:,1) + ...
    neighborclm2_ctrd(:,1)) ./ 2;
    frac2frac_ctrd(:,2) = (neighborclm1_ctrd(:,2) + ...
    neighborclm2_ctrd(:,2)) ./ 2;
    frac2frac_ctrd_old = frac2frac_ctrd;

    for i = 1:length(T2)
        if ismember(frac2frac_ctrd(i,:), GT.faces.centroids,  'rows') == 1
            % find the location of T2 in T and replace the wrong values
            T(ismember(GT.faces.centroids, frac2frac_ctrd(i,:), 'rows')) ...
= T2(i);
        else
            % find the location of intersections and correct the values in T
            if frac2frac_ctrd(i,1)-floor(frac2frac_ctrd(i,1)) > ...
GT.L(1)/GT.cartDims(1)/2 && ...
```

```
                    frac2frac_ctrd(i,2)-floor(frac2frac_ctrd(i,2)) > ...
GT.L(2)/GT.cartDims(2)/2
                frac2frac_ctrd(i,1) = ...
frac2frac_ctrd(i,1)+GT.L(1)/GT.cartDims(1)/4;
                frac2frac_ctrd(i,2) = ...
frac2frac_ctrd(i,2)+GT.L(2)/GT.cartDims(2)/4;

            elseif frac2frac_ctrd(i,1)-floor(frac2frac_ctrd(i,1)) < ...
GT.L(1)/GT.cartDims(1)/2 && ...
                    frac2frac_ctrd(i,2)-floor(frac2frac_ctrd(i,2)) < ...
GT.L(2)/GT.cartDims(2)/2
                frac2frac_ctrd(i,1) = frac2frac_ctrd(i,1)- ...
GT.L(1)/GT.cartDims(1)/4;
                frac2frac_ctrd(i,2) = frac2frac_ctrd(i,2)- ...
GT.L(2)/GT.cartDims(2)/4;

            elseif frac2frac_ctrd(i,2)-floor(frac2frac_ctrd(i,2)) < ...
GT.L(2)/GT.cartDims(2)/2 && ...
                    frac2frac_ctrd(i,1)-floor(frac2frac_ctrd(i,1)) > ...
GT.L(1)/GT.cartDims(1)/2
                frac2frac_ctrd(i,2) = frac2frac_ctrd(i,2)- ...
GT.L(2)/GT.cartDims(2)/4;
                frac2frac_ctrd(i,1) = ...
frac2frac_ctrd(i,1)+GT.L(1)/GT.cartDims(1)/4;

            elseif frac2frac_ctrd(i,2)-floor(frac2frac_ctrd(i,2)) > ...
GT.L(2)/GT.cartDims(2)/2 && ...
                    frac2frac_ctrd(i,1)-floor(frac2frac_ctrd(i,1)) < ...
GT.L(1)/GT.cartDims(1)/2
                frac2frac_ctrd(i,2) = ...
frac2frac_ctrd(i,2)+GT.L(2)/GT.cartDims(2)/4;
                frac2frac_ctrd(i,1) = frac2frac_ctrd(i,1)- ...
GT.L(1)/GT.cartDims(1)/4;
            end

            T(ismember(GT.faces.centroids, frac2frac_ctrd(i,:), 'rows')) ...
= T2(i);
        end
    end

    T = T(s.internalConn); % Get internal trans

    % ------------------------------------------------------------------------

    % Gravity contribution
    gdz = model.getGravityGradient();

    % Evaluate water properties
    [vW, bW, mobW, rhoW, pW, upcw] = ...
    getFluxAndPropsWater_BO(model, p, sW, krW, T, gdz);
    bW0 = model.fluid.bW(p0);

    % Evaluate oil properties
    [vO, bO, mobO, rhoO, p, upco] = ...
    getFluxAndPropsOil_BO(model, p, sO, krO, T, gdz);
```

```
    bO0 = getbO_BO(model, p0);

    if model.outputFluxes
        state = model.storeFluxes(state, vW, vO, []);
    end
    if model.extraStateOutput
        state = model.storebfactors(state, bW, bO, []);
        state = model.storeMobilities(state, mobW, mobO, []);
        state = model.storeUpstreamIndices(state, upcw, upco, []);
    end

    % ------------------------------------------------------------------

    % Update porosity
    % Upstream weight b factors & multiply by interface fluxes to obtain the
    % fluxes at standard conditions.
    bOvO = s.faceUpstr(upco, bO).*vO;
    bWvW = s.faceUpstr(upcw, bW).*vW;

    % Computation of "effective" porosity which take into account the changes
    % due to mechanics.
    switch ppg_switch
        case 'no ppg'
            poro = rock.poro;
            porofrac = poro(length(drivingForces.mstate.stress)+1);

        case 'ppg'
            poro = rock.poro;
            porofrac_act = poro(G.actCells);
            porofrac_inact = poro(hybridInd);

        otherwise
            error('Do not recognized')

    end

    % Make the size of the variables below consistent with 'mechTerm'
    rock.poro = poro(1:length(drivingForces.mstate.stress), :);
    G.cells.volumes = ...
    G.cells.volumes(1:length(drivingForces.mstate.stress), :);
    rock.alpha = rock.alpha(1:length(drivingForces.mstate.stress), :);

    effPorVol = rock.poro.*(G.cells.volumes.*pvMult) + rock.alpha .* ...
              mechTerm.new;
    effPorVol0 = rock.poro.*(G.cells.volumes.*pvMult0) + rock.alpha .* ...
        mechTerm.old;

    switch ppg_switch
        case 'no ppg'
            porofrac = ...
porofrac*(GT.cells.volumes(length(drivingForces.mstate.stress)+1)*pvMult0);
            porofrac = porofrac * ones(length(actCells), 1);
            effPorVol.val = [effPorVol.val; porofrac];
            effPorVol0 = [effPorVol0; porofrac];
```

```
    case 'ppg'
        % Update fracture porosity
        porofrac_act = apertureNew./(GT.L(1)/GT.cartDims(1));
        effPorVol.val = [effPorVol.val; porofrac_inact];
        effPorVol0 = [effPorVol0; porofrac_inact];
        effPorVol.val(G.actCells) = porofrac_act;
        effPorVol0(G.actCells) = porofrac_act;

    otherwise
        error('Do not recognized')
end

% Make the format of ADI variables consistent
num = length(effPorVol.jac);
for i = 1 : 2
    jac = full(effPorVol.jac{i});

    jac1 = zeros(hybridn);
    jac = blkdiag(jac, jac1);

    jac = sparse(jac);
    effPorVol.jac{i} = jac;
end

for i = 3 : num
    jac = full(effPorVol.jac{i});

    jac1 = zeros(hybridn,size(jac,2));
    jac = [jac;jac1];

    jac = sparse(jac);
    effPorVol.jac{i} = jac;
end

% ------------------------------------------------------------------------

% Governing Equation for the flow problems
% Conservation of mass for water
water = (1./dt).*(effPorVol.*bW.*sW - effPorVol0.*bW0.*sW0)  + ...
s.Div(bWvW);
% Conservation of mass for oil
oil = (1./dt).*(effPorVol.*bO.*sO - effPorVol0.*bO0.*sO0)  + s.Div(bOvO);

eqs = {water, oil};
names = {'water', 'oil'};
types = {'cell', 'cell'};

% Finally, add in and setup well equations
wellSol = model.getProp(state, 'wellsol');
[~, wellVarNames, wellMap] = ...
    model.FacilityModel.getAllPrimaryVariables(wellSol);
wellSol0 = model.getProp(state0, 'wellsol');

% Store the change of the fracture into the variable 'state', and pass
```

```
    % it to the next timestep
    state.fracNodes = fracNodes; % Fracture nodes
    state.apertureNew = [apertureNew,actCells]; % Fracture aperture

    [eqs, names, types, state.wellSol] = model.insertWellEquations(eqs,
names, types, wellSol0, wellSol, wellVars, wellMap, p, {mobW, mobO}, {rhoW,
rhoO}, {}, {}, dt, opt);

end
```